uOttawa

L'Université canadienne
Canada's university

FACULTÉ DES ÉTUDES SUPÉRIEURES ET POSTOCTORALES

uOttawa

L'Université canadienne
Canada's university

FACULTY OF GRADUATE AND POSDOCTORAL STUDIES

Ryan Bolen
AUTEUR DE LA THÈSE / AUTHOR OF THESIS

M.Sc. (Physics)
GRADE / DEGREE

Department of Physics
FACULTÉ, ÉCOLE, DÉPARTEMENT / FACULTY, SCHOOL, DEPARTMENT

A Study of Optical Frequency Domain Reflectometry and its Associated Distributed Sensor Applications

TITRE DE LA THÈSE / TITLE OF THESIS

X. Bao
DIRECTEUR (DIRECTRICE) DE LA THÈSE / THESIS SUPERVISOR

CO-DIRECTEUR (CO-DIRECTRICE) DE LA THÈSE / THESIS CO-SUPERVISOR

S. Desgreniers

L. Ramunno

J. Armitage

Gary W. Slater
Le Doyen de la Faculté des études supérieures et postdoctorales / Dean of the Faculty of Graduate and Postdoctoral Studies

A Study of Optical Frequency Domain Reflectometry and its Associated Distributed Sensor Applications

Ryan Bolen

Thesis submitted to the
Faculty of Graduate and Postdoctoral Studies
In partial fulfillment of the requirements
For the M.Sc. degree in Physics

Department of Physics
Faculty of Science
University of Ottawa

Your file Votre référence
ISBN: 978-0-494-65486-6
Our file Notre référence
ISBN: 978-0-494-65486-6

Table of Contents

Abstract

Optical Frequency Domain Reflectometry (OFDR) is an interferometric technique which is capable of interrogating fibers under test (FUT) up to kilometers in length with millimeter resolution[10]. It does so by taking the Rayleigh backscattered light, or Fresnel back-reflected light and combining it with the reference arm to create a beating signal. The beating signal is then Fourier transformed to create a scattering profile of the FUT. Presented in this thesis are 5 novel OFDR configurations that improve the SNR in the spatial domain up to 26dB. As well, 4 new data analysis algorithms are presented that improve the spectral resolution by up to a factor of 40 and spectral SNR by 1.31dB. The FUT's investigated are regular SMF, linear FBG's, and chirped FBG's. With these, the wavelength shift at specific points along the FUT is measured and correlated with temperature changes (with associated applications), longitudinal stress, and torsional stress stimuli.

Acknowledgements

I would like to thank my supervisor, Dr. Xiaoyi Bao, for giving me the opportunity to be a part of her research team and always providing support in research related matters. The completion of this thesis would have been impossible without her many insightful conversations.

Dr. Wenhai Li guided me down the right path on a many of occasions by suggesting I investigate certain avenues that I may have otherwise overlooked and/or recommended that certain areas I was skimming over that I in turn should look more in depth. He also assisted me in the very early troubleshooting stages of my setup development which was also greatly appreciated. Robert Walker also bears a thank-you for fabricating me the linear FBG's used in §5.3.

I would also like to thank Dr. Cheng Hu, Research Officer and Weimin Qian, Technical Officer who are members of the NRC-IFCI (National Research Council – Institute for Fuel Cell Innovation) facility in Vancouver. Dr. Cheng Hu for allowing me the opportunity to go out there and collaborate with his group in the development of a distributed temperature sensor for in-situ mapping of temperature distribution inside of a PEM (proton exchange membrane) hydrogen fuel cell. Weimin Qian for basically helping to provide me with anything I needed during the developmental phase of the setup at their facility, as well as for several insightful conversations that allowed me to eventually develop the Fourier Interpolation algorithm.

List of Tables

List of Figures

List of Abbreviations

BF:	Boxcar Filter
CW:	Continuous Wave
DUT:	Device Under Test
EM:	Electromagnetic
EOSR:	Extended Optical Sweep Range
ESS:	Extended Segment Size
FFT:	Fast Fourier Transform
FFT^{-1}:	Inverse Fast Fourier Transform
FIA:	Fourier Interpolation Algorithm
FBG:	Fiber Bragg Grating
FMCW:	Frequency Modulated Continuous Wave Reflectometry
FOS:	Fiber Optic Sensor
FUT:	Fiber Under Test
FWHM:	Full Width at Half Maximum
GPIB:	General Purpose Interface Bus
NRC-IFCI:	National Research Council – Institute for Fuel Cell Innovation
OCT:	Optical Coherence Tomography
OFDR:	Optical Frequency Domain Reflectometry

OLCR:	Optical Low Coherence Reflectometry
OPD	Optical Path Difference
OTDR:	Optical Time Domain Reflectometry
PBS:	Polarization Beam Splitter
PDL:	Polarization Dependent Loss
PEM:	Proton Exchange Membrane
PM:	Polarization Maintaining
PMD:	Polarization Mode Dispersion
SHM:	Structural Health Monitoring
SMF:	Single Mode Fiber
SNR:	Signal-to-Noise Ratio
SOP:	State of Polarization
TDM:	Time Division Multiplexing
WDM:	Wavelength Division Multiplexing

Chapter 1

Introduction

1.1 Optical Fiber Sensors

Over the last 20 years there have been two major technology revolutions that have affected almost everyone on the planet. The first is the area of optoelectronics while the second is that of the fiber optics communications industry. The optoelectronics industry has brought us such things as DVD players, laser printers, and laser pointers. The fiber optics communications industry has overhauled our telecommunications networks making them more reliable, while also providing us with orders of magnitude more bandwidth on demand compared to its copper wire counterparts.

It is because the components that are needed for these two industries (i.e. - cheaper and smaller lasers, modulators, couplers, WDM's, circulators, etc.) are also needed for the field of optical fiber sensing that it has allowed it to also flourish in parallel. As the cost of these components has dropped, it has made it more feasible for fiber optic sensors to replace their electronic counterparts such as strain gauges, thermistors and/or thermocouples, pressure gauges, humidity sensors, and chemical sensors. In recent years fiber optic sensors have become quite popular in the area of structural health monitoring such as bridges[1], skyscrapers and oil/oil sand pipelines[2, 8]. Industries ranging from automotive, to aviation and aerospace have also taken interest for applications that ranges from temperature monitoring, to chemical sensing as well as vibration monitoring. Historically speaking almost all of the electrical sensors listed above are what are considered to be point sensors whereby a separate channel is needed for each sensor to both supply the needed voltage/current for it to operate properly as well as to measure any changes. To implement

large networks of these sensors meant that it very quickly became expensive and complicated. The optical sensor equivalent to these electrical point sensors are fiber Bragg gratings (further details shall be provided in a later chapter). On their own they have a comparable performance to their electrical counterparts. The big difference though is that if each of the FBG's have different central wavelengths then it is possible to multiplex many of them in series – thereby having many point sensors that can be measured simultaneously using only one channel. This alone significantly can cut down on system overhead costs without sacrificing accuracy. The other problem is that what if the event you are trying to detect happens to be in between two of the point sensors of the array? Ultimately this event will be missed and/or will not be properly measured. The advantage of using SMF or other specialty fibers as the DUT means that the measurement can be done anywhere along it as opposed to at discrete points so that no events are missed. This is what is known as distributed sensing.

The above measurands affect the light being transmitted through the fiber by modulating its intensity, phase, polarization, or wavelength (or some combination thereof). The spatial information of the stimuli is usually given by either the round-trip propagation times in the fiber when optical pulses are used to interrogate the FUT (time domain detection), or a reference arm and interferometer configuration when continuous light is used (frequency domain detection). The technique as shall be discussed in more detail in subsequent sections/chapters linearly sweeps continuous light through an interferometer setup to retrieve the location information and looks primarily at the variation of the phase/wavelength to determine the degree of the stimulus.

1.2 Optical Fibers

An optical fiber is a long, thin, cylindrical dielectric waveguide made of silica glass or polymer. The three most common fiber optic configurations as well as their index profiles can be seen in Fig.1.1 below:

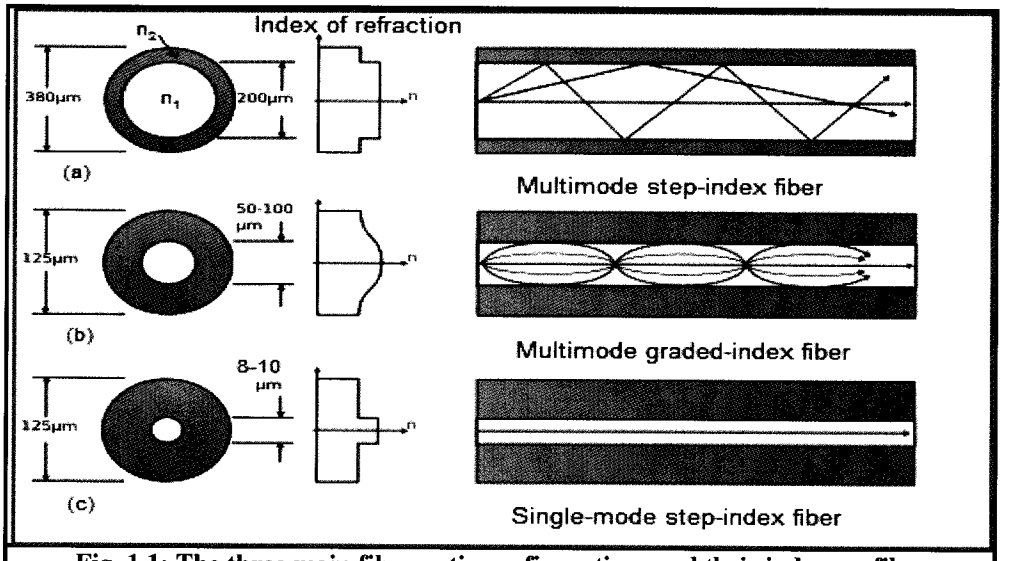

Fig. 1.1: The three main fiber optic configurations and their index profiles.

Of these types of fiber the most common type is known as step index fiber. This consists of a core of index n_1 surrounded by a cladding of lower refractive index n_2. The relative difference between these two indices of refraction can be found by the following equation: $\Delta = (n_1 - n_2)/n_1$. Values for n_1 are usually between 1.44 and 1.46, while Δ is usually between 0.001 and 0.02. The overall effective group index of refraction for standard SMF-28 fiber at 1550nm is 1.4682. Other refractive index profiles and spectral attenuation information for SMF-28 fiber can be seen in Fig.1.2 below[3]. Besides Δ, another useful parameter for optical fiber is the V number with determines the overall number of modes that are capable of propagating through the core of the fiber. This parameter can be determined using the following equation:

$$V = k_0 a \left(n_1^2 - n_2^2\right)^{\frac{1}{2}}, \qquad (1.1)$$

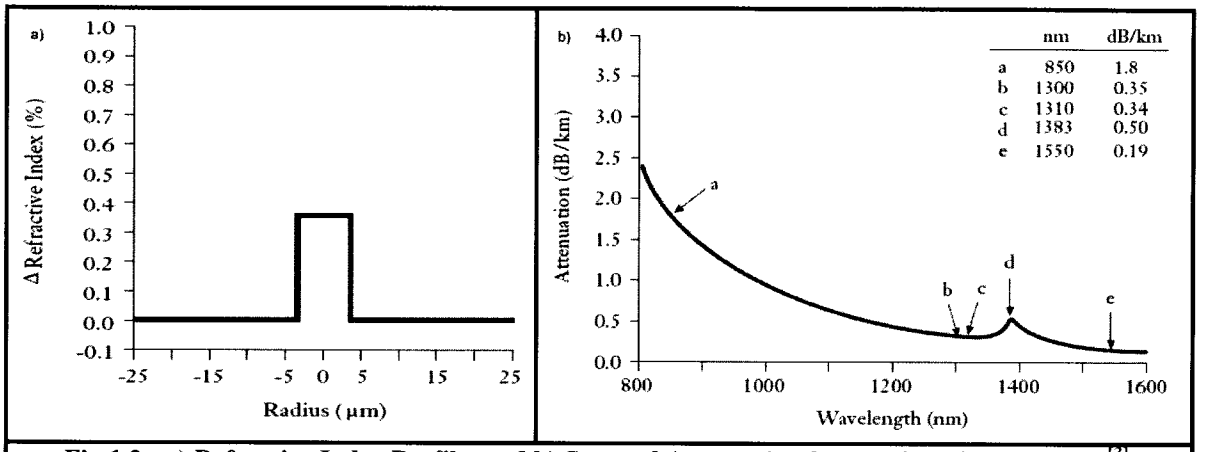

Fig.1.2 - a) Refractive Index Profile, and b) Spectral Attenuation for standard SMF-28 fiber[3].

whereby a is the radius of the core, $k_0 = 2\pi/\lambda$, and λ is the wavelength of the light. When $V < 2.405$, the fiber will support only a single mode[45]. For the central wavelength of 1550nm which is used in the research provided in subsequent chapters the core diameter of the fiber used is 8.2μm and the cladding is of diameter 125μm. These parameters confine the light to propagate in only a single-mode through the fiber.

If single-mode fibers had perfect axial symmetry and the glass was homogeneous throughout then there would be no degenerate modes. Unfortunately, during the fabrication process there results a 1% variation in the concentricity of the core and cladding, as well as a variation in the internal stresses. This means that the propagation constants along the 2 axes are no longer equal ($\beta_x \neq \beta_y$) creating a mode degeneracy that causes a mixing of the two polarization states. Ideally the power between the two modes would be exchanged in a periodic manner with a beat length of:

$$L_B = \frac{2\pi}{|\beta_x - \beta_y|} = \frac{\lambda}{B_m}, \tag{1.2}$$

where B_m is the modal birefringence and is defined as:

$$B_m = \frac{|\beta_x - \beta_y|}{k_0} = |n_x - n_y|, \tag{1.3}$$

where n_x and n_y are the index of refractions for the two orthogonal modes. Realistically though, the modal birefringence is constantly and randomly changing along its length because of the constant fluctuation of the core radius and shape as well as other imperfections. Another problem is that each orthogonal mode propagates at slightly different velocities. Accordingly, for OTDR style systems using pulses sent down km's of fiber the pulse will experience a distortion/broadening of the pulse along the two polarization axes that can affect the accuracy of the results. This effect is known as polarization mode dispersion (PMD). Luckily, for OFDR techniques that use continuous wave light for sensing, and typically sense over a DUT of $\leq$ 100m PMD does not really play a large role.

For applications that need to preserve the polarization state – polarization maintaining fibers are often used. These fibers are fabricated with a stress-induced birefringence such that only a single fiber state is supported and/or the two polarization modes become discretely decoupled[4]. The three main styles of PM fiber are shown in the figure below:

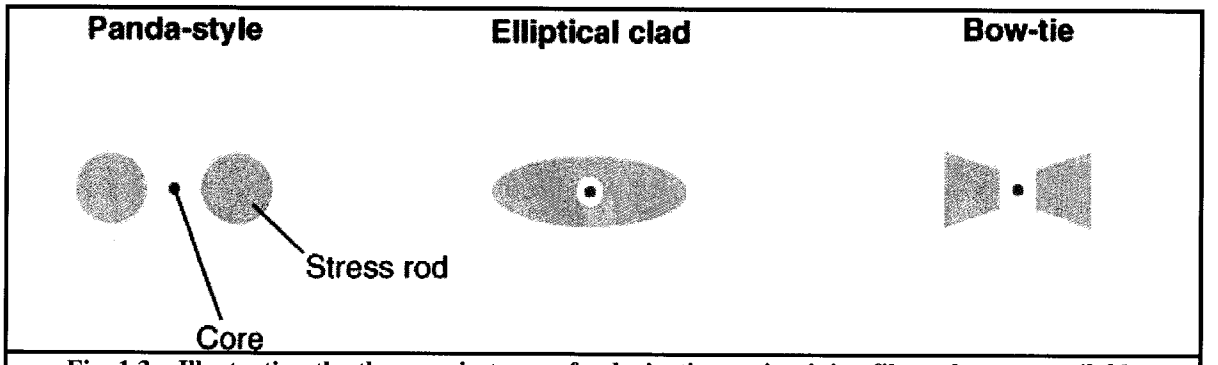

Fig. 1.3 – Illustrating the three main types of polarization maintaining fibers that are available

1.3 Optical Scattering

When referring to electromagnetic radiation that is in the ultraviolet to infrared range (10nm to 10μm) - there are four types of scattering that it can experience as it propagates

through gases, liquids and solids. These four types are: Raman, Brillouin, Rayleigh, and Rayleigh-wing scattering.

Raman scattering results from the interaction of light with the vibrational modes of the molecules or atoms in the scattering medium. This is equivalent to saying that it is the optical scattering from optical phonons. Brillouin scattering can be considered as the optical scattering from sound, pressure or density waves. Equivalently, this is described as scattering from acoustic phonons. Both Raman and Brillouin scattering are forms of inelastic scattering and result in a wavelength shift. Rayleigh scattering is what is considered the scattering of light from non-propagating density fluctuations or entropy fluctuations. Rayleigh-wing scattering is scattering from fluctuations in orientation of anisotropic molecules and is spectrally very broad. Although found in solids, this type of scattering is more commonly experienced in liquids and gases. Both Rayleigh and Rayleigh-wing can be considered quasi-elastic in that the scattered wave does not exhibit any frequency shifts. The frequency relationships of the four scattering processes are shown in Fig. 1.4. The Brillouin Stokes and anti-Stokes components are separated from the Rayleigh peak by the Brillouin frequency ν_B.

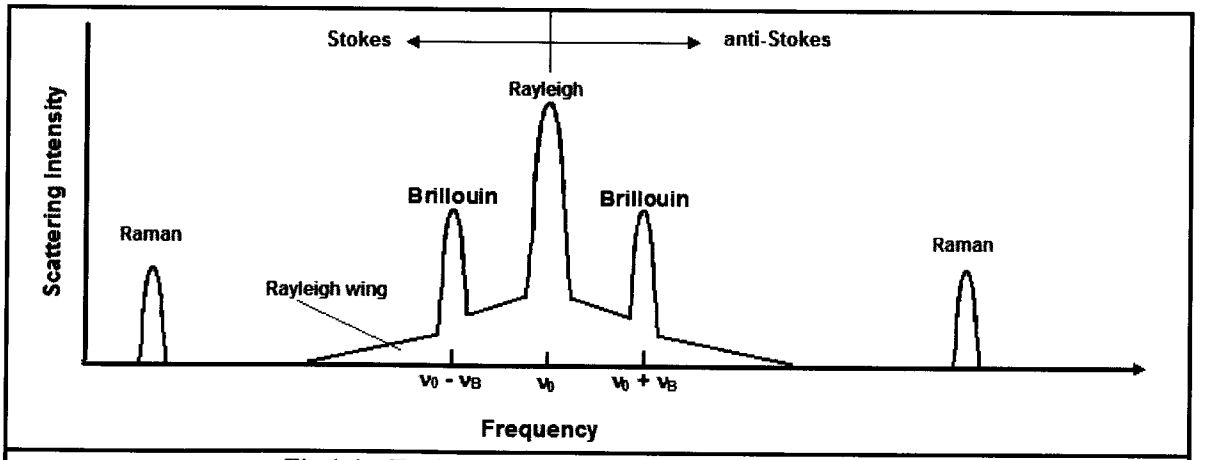

Fig.1.4 – Typical spontaneous light scattering spectrum

All three of these types of scattering are capable of occurring as both spontaneous and stimulated scattering. Spontaneous scattering means that the optical properties of the material system are unaffected by the presence of the incident light. Stimulated light scattering refers to the condition in which the fluctuations causing the scattering are induced by the presence of the incident light. Since the research in question deals with Rayleigh backscattered light, only it will be addressed from here on.

Process	*Typical Shift* (cm^{-1})	*Linewidth* (cm^{-1})	*Relaxation Time (s)*	*Gain (cm/MW)*
Raman	1000	5	10^{-12}	$5\ 10^{-3}$
Brillouin	0.1	5×10^{-3}	10^{-9}	10^{-2}
Rayleigh	0	5×10^{-4}	10^{-8}	10^{-4}
Rayleigh-wing	0	5	10^{-12}	10^{-3}

Table 1.1 – General values of the parameters which describe the four types of scattered light.[5]

1.4 Mathematical Treatment of Spontaneous Rayleigh Scattering

The fluctuations in the dielectric constant which are at the root of Rayleigh scattering can be expressed in terms of the thermodynamic variables density ρ and temperature T as[5]:

$$\Delta\varepsilon = \left(\frac{\partial\varepsilon}{\partial\rho}\right)_T \Delta\rho + \left(\frac{\partial\varepsilon}{\partial T}\right)_\rho \Delta T\,. \tag{1.4}$$

To within a 2% accuracy, one can ignore the second term[6] since the dielectric constant typically depends more on the density than on the temperature. One now takes the entropy s and pressure p to be the independent thermodynamic variables. The variation in density can then be represented as[5]:

$$\Delta\rho = \left(\frac{\partial\rho}{\partial p}\right)_s \Delta p + \left(\frac{\partial\rho}{\partial s}\right)_p \Delta s\,. \tag{1.5}$$

The first term in (1.5) describes the adiabatic density fluctuations (acoustic waves) which leads to Brillouin scattering, while the second term describes the isobaric density fluctuations

(temperature or entropy fluctuations) that leads to Rayleigh scattering. By subbing (1.5) into (1.4) and looking at the portion of the dielectric constant fluctuations which is responsible for Rayleigh scattering we have:

$$\Delta\varepsilon = \left(\frac{\partial\varepsilon}{\partial\rho}\right)_T \left(\frac{\partial\rho}{\partial s}\right)_p \Delta s\,. \tag{1.6}$$

This as can be seen is proportional to entropy. The entropy fluctuations are described by the same equation as one uses to describe temperature variations[5]:

$$\rho c_p \frac{\partial \Delta s}{\partial t} - \kappa\nabla^2 \Delta s = 0\,, \tag{1.7}$$

where c_p is the specific heat at constant pressure, and κ is the thermal conductivity. These fluctuations obey the diffusion equation and not the wave equation. A solution to the diffusion equation (1.7) is[5]:

$$\Delta s = \Delta s_0 e^{-\delta t} e^{-q\cdot r}\,, \tag{1.8}$$

where the damping rate of the entropy disturbance is given as[5]:

$$\delta = \frac{\kappa}{\rho c_p} q^2\,. \tag{1.9}$$

As can be seen from (1.8), that unlike pressure waves – the entropy fluctuations do not propagate. Accordingly, the nonlinear polarization which is proportional to Δs can give rise to purely an unshifted component of the scattered light. The FWHM of this component is given by $\delta\omega_c = \delta$ or [5]:

$$\delta\omega_c = \frac{4\kappa}{\rho c_p}|k|^2 \sin^2(\theta/2)\,. \tag{1.10}$$

It should be noted that because of the internal reflection a single-mode fiber, the only possible directions for scattering are forward (θ = 0) and backward (θ = π). Forward Rayleigh scattered light is considered part of the transmitted light, but for OFDR sensing

applications we are primarily interested in the Rayleigh backscattered light. Accordingly, subbing ($\theta = \pi$) into (1.10) we get a FWHM of:

$$\delta\omega_c = \frac{4\kappa}{\rho c_p}|\mathrm{k}|^2 = \frac{4\kappa}{\rho c_p} n^2 \frac{\omega^2}{c^2} \ . \tag{1.11}$$

Although stimulated Rayleigh scattering exists, for the OFDR setups described herein the incident light used is not of a high enough intensity to induce extra fluctuations in the dielectric constant. Accordingly I shall not address the mathematics of stimulated Rayleigh scattering.

1.5 Three Primary Types of Reflectometry using Rayleigh Backscatter

Over the last 20 years there have been three types of reflectometry developed which are capable of using Rayleigh backscattered light (wavelength dependent), as well as Fresnel reflections (wavelength independent) as the sensing mechanism capable of interrogating a FUT. These are 'Optical Low Coherence Reflectometry' (OLCR), 'Optical Frequency Domain Reflectometry' (OFDR) which also goes by the older name of 'Frequency Modulated Continuous Wave Reflectometry' FMCW, and 'Optical Time Domain Reflectometry' (OTDR). The operation ranges of these 3 types of reflectometry are shown below:

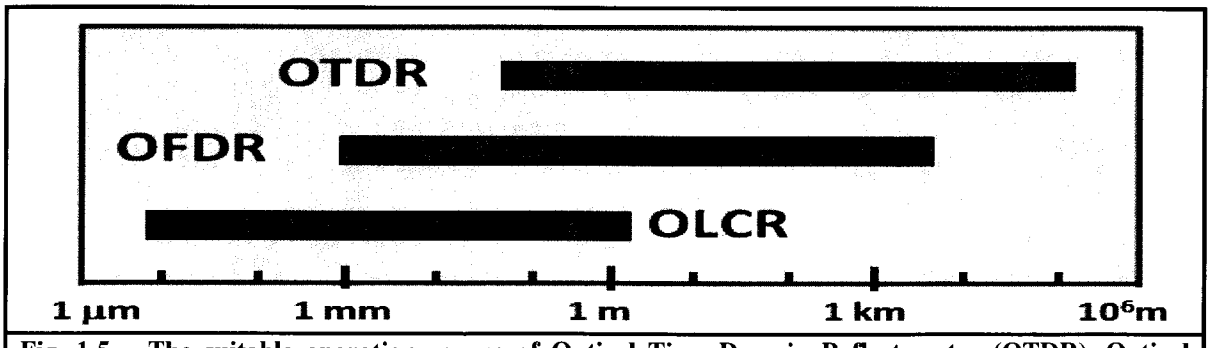

Fig. 1.5 – The suitable operation ranges of Optical Time Domain Reflectometry (OTDR), Optical Frequency Domain Reflectometry (OFDR), and Optical Low Coherence Reflectometry (OLCR)

The following two subsections shall provide a brief overview of OTDR and OLCR. The details of OFDR shall be provided in the next section.

1.5.1 *Optical Time Domain Reflectometry*

A basic OTDR setup can be seen in Fig. 1.6 on the following page. It works by sending multiple optical pulses down a FUT. The light from the pulse that gets back-reflected either via Rayleigh scattering or Fresnel reflection is then measured using a photodetector converted to a voltage signal and saved using an oscilloscope or other data acquisition card. After sending many pulses and taking the average of the backscattered signal a typical profile of say the FUT in Fig. 1.6 can be seen in Fig. 1.7:

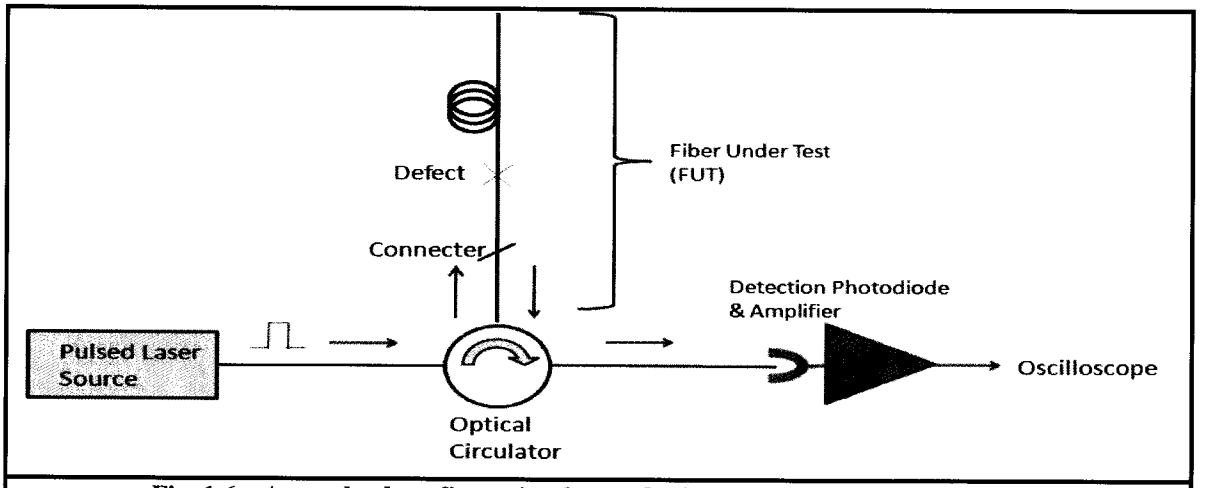

Fig. 1.6 – A standard configuration for an Optical Time Domain Reflectometer

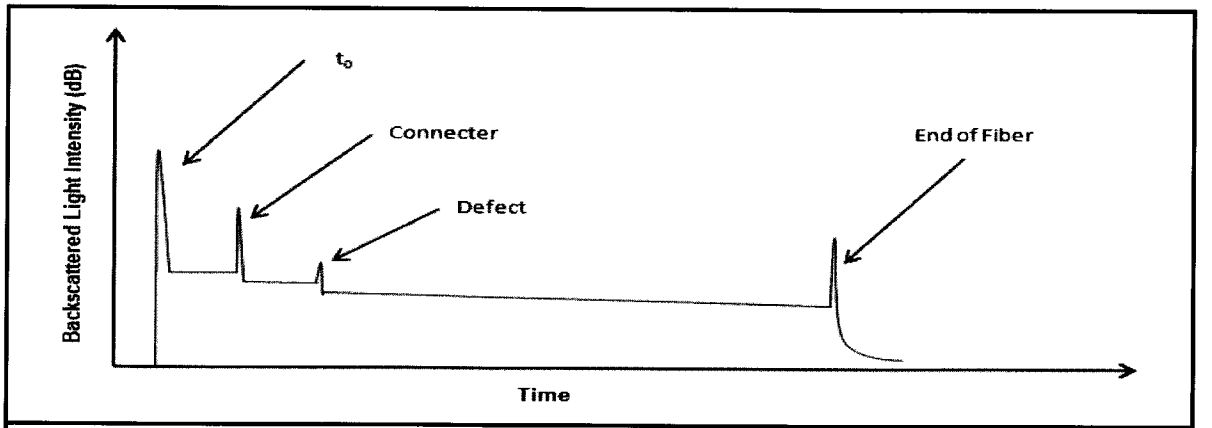

Fig. 1.7 – An example of a time domain backscattered light profile of a fiber under test

Allowing x to represent some position along the Fiber Under Test that represents a scattering/back reflecting event we can say that the time between the pulse emission and its detection is given as: $t - t_0 = 2x/v_g$, where v_g is the group velocity in the fiber. Where τ represents the pulse duration, the spatial resolution of the backscattered profile is approximately: $v_g * \tau/2$. So, for the example of a 10ns pulse the resolution is roughly 1m.

The contribution of the backscattered signal which specifically comes from the Rayleigh scattering can be expressed by the following[7]:

$$P_{bs}(x) = S\frac{\alpha_d}{2} v_g \tau \cdot P_{in}(x=0) \cdot e^{-2\alpha x}, \tag{1.12}$$

where S represents the capture coefficient which is proportional to $\propto (NA/n)^2$ where for $\lambda = 1.55\mu m$, $S \cong 1.5x10^{-3}$; the diffusion coefficient, $\propto_d \propto 1/\lambda^4 \cong 0.14 dB/km$, while the group velocity v_g for the SMF at 1.55μm is $2x10^8$m/s. $P_{in}(x=0)$ represents the input optical power at position x = 0, and α is the attenuation coefficient for the fiber under test. On the other hand, the portion of the signal that comes more from Fresnel reflections from say: the end of the fiber, connectors, components in a network under test, cracks and so on can be expressed as[7]:

$$P_r(x) = R \cdot P_{in}(x=0) \cdot e^{-2\alpha x}, \tag{1.13}$$

where R represents the reflection coefficient for each item, and S represents the capture

The dynamic range of an OTDR is dependent on a combination of the optical pulse output power, pulse width, input sensitivity, and integration time. The higher pulse output power and input sensitivity can improve the measuring range, however the pulse width and signal integration time choices are more application specific. Longer pulses improve the attenuation measurement resolution and dynamic range but at the expense of spatial

resolution. Short pulses on the other hand improve the spatial resolution but also reduce the measurement range and attenuation measurement resolution. This measurement length is also referred to as the dead zone whereby it is the minimum distance needed to distinguish reflective discrete optical events. Some dead zone values can be seen in Table 1.2 below:

Pulse Length	Event Dead Zone
1ns	0.15m
10ns	1.5m
100ns	15m
1μs	150m
10μs	1.5km
100μs	15km

Table 1.2 – Pulse Lengths vs. Dead Zone size for OTDR

Although an OTDR setup is capable of being used for FUT's that are several km's in length, and have short measure times – the biggest drawback is the poorer spatial resolution.

1.5.2 *Optical Low Coherence Reflectometry*

There are two main configurations of OLCR setups which can be seen in Fig.1.8 below:

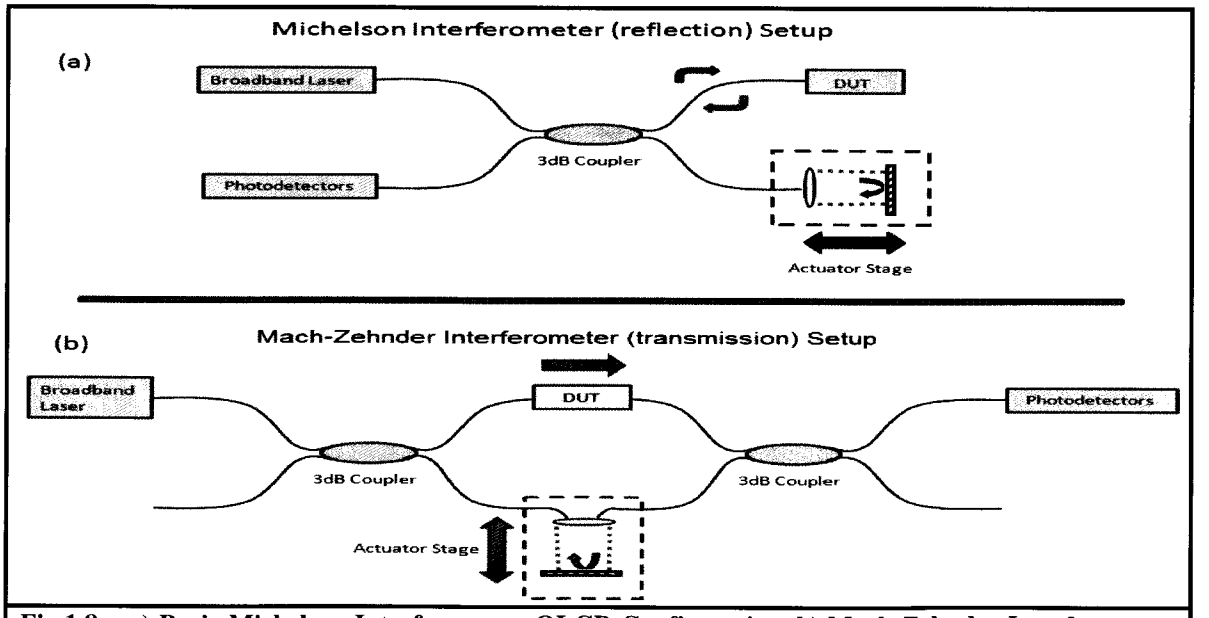

Fig.1.8 – a) Basic Michelson Interferometer OLCR Configuration, b) Mach-Zehnder Interferometer OLCR Configuration

If you take Fig.1.8(a) and replace the DUT with an objective lens and a Sample Under Test (SUT) the setup is also commonly referred to as Optical Coherence Tomography (OCT). This is typically used in medical/biological applications to create 3D images of tissue samples.

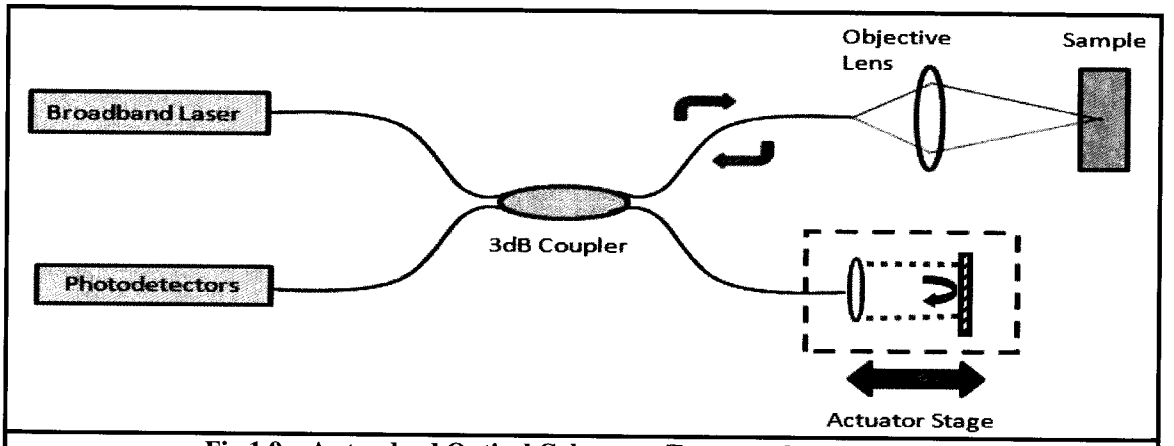

Fig.1.9 – A standard Optical Coherence Tomography setup (OCT)

The general operation of the OLCR setup is as follows. A broadband light source is sent through a 3dB (50/50) coupler. Half of the light is reflected by variable position mirror mounted on an actuator stage (the reference arm), while the other half of the light is sent to a FUT/SUT. The backscattered light signal recombines with the reference arm signal and is measured by the photodetector. The signal measured by the detector will remain DC so long as the spatial difference between the reference arm and the DUT arm is less than or equal to the coherence length of the laser source. The coherence length of the system is determined by the spectral width as given by the following equation:

$$L_c = \frac{\lambda^2}{n\Delta\lambda}, \tag{1.14}$$

where λ is the central wavelength of the source, $\Delta\lambda$ is the spectral FWHM of the source and n is the refractive index of the DUT. Once the magnitude of the spatial difference of the two

arms is less than or equal to the coherence length then an interference (AC) signal shall start to appear. In other words, if the source bandwidth is $\Delta\upsilon$, and the time delay, $\Delta\tau$ in which the interferometric fringes can be seen then[9]:

$$\Delta\tau\Delta\upsilon \leq 1. \tag{1.15}$$

The time delay, $\Delta\tau$, is the coherence time of the source[9]:

$$\Delta\tau \approx 1/\Delta\upsilon. \tag{1.16}$$

So the coherence length, L_c can also be expressed as[9]:

$$L_c = c\Delta\tau/n \approx c/n\Delta\upsilon. \tag{1.17}$$

When scanning the actuator stage such that the difference between the two arms passes through the coherence length range one gets the following type distribution:

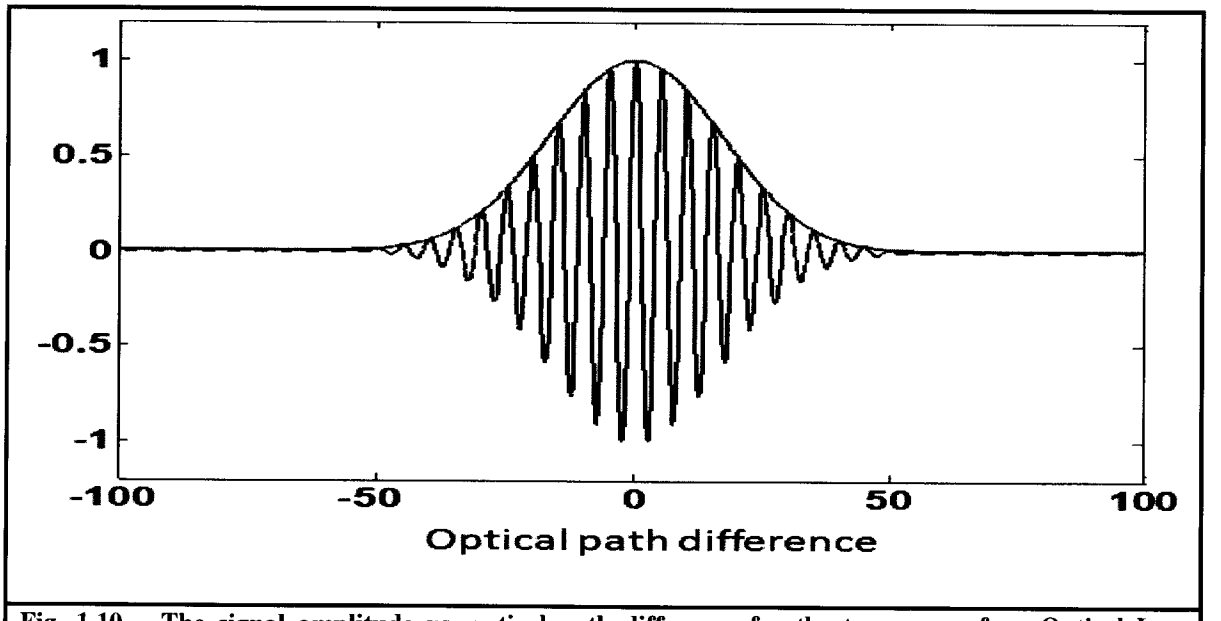

Fig. 1.10 – The signal amplitude vs. optical path difference for the two arms of an Optical Low Coherence Reflectometry setup.

This is in fact the cross-correlation of the two arms of the interferometer. From this plot one can determine the position of the reflection and/or backscatter event on the FUT arm to a very high degree – down to microns in precision.

Although the OLCR setup is very accurate in providing the spatial profiles of a particular DUT, it has two main drawbacks: a) the scanning process of the mirror on the reference arm is quite time consuming, and b) the actuator stage must be longer than the full DUT. Unfortunately the longest 'precision' states are only about a meter in length so the full DUT length must be less than this.

1.6 Optical Frequency Domain Reflectometry Analytical Overview

As was summarized in §1.5, Optical Time Domain Reflectometry is fast and can interrogate FUT's of length's 10's of kilometers but has a spatial resolution around a meter. Optical Low Coherence Reflectometry can give spatial resolution down to microns in scale but only allows for a maximum FUT length of about 1m, as well as can take many seconds just to distinguish one backscattering event (on the order of minutes and even hours to profile a full FUT). A good compromise between the two techniques is something called Optical Frequency Domain Reflectometry. The technique is capable of providing < 1mm spatial resolution, with FUT's of up to 2km[10]. As well, it only takes a few seconds to get the full profile of FUT. The research covered in this thesis goes over variants of the classical OFDR setup. This section will cover the analytical theory of classical OFDR. It should be noted that this theory has been published many times over the years, in the following references [11 – 15, 17] to name a few. I shall work through it again here for the sake of completeness.

The idea of frequency domain reflectometry was first developed about half a century ago[16] for electric radar but was introduced into optics for the first time in 1981[11]. The original name of this technique was frequency modulated continuous wave (FMCW) interferometry but also goes by the more recent names of OFDR and swept wavelength

interferometry (SWI). No matter what the name though – the general layout remains the same. A relatively coherent optical wave, in which the frequency is continuously modulated with a proper waveform (i.e. – sawtooth or triangular) and is divided into two waves via a coupler/splitter. The one signal becomes the reference path where the other travels along a FUT (fiber under test) path. These two waves then recombine to interfere. By measurement of the frequency or phase shift of the produced beat signal, the optical path difference (OPD) between the two waves is determined.

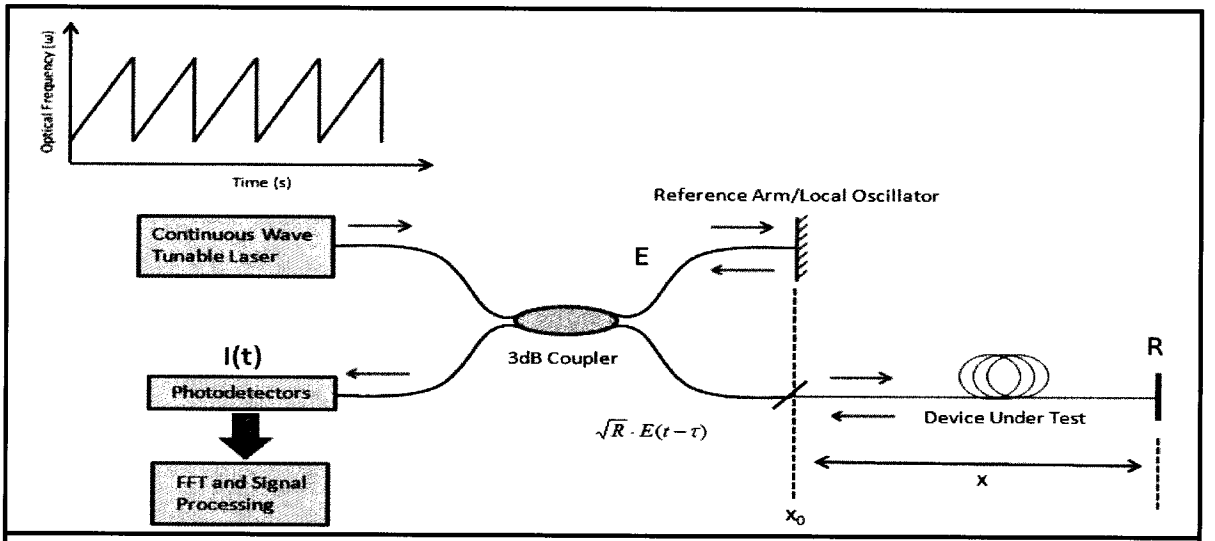

Fig. 1.11 – Classical Optical Frequency Domain Reflectometry (OFDR) Setup

1.6.1 Optical Frequency Domain Reflectometry – General Theory

A general diagram of the fiber optic OFDR can be seen in Fig.1.11. The optical frequency in the laser is continuously modulated. This light source still has the typical amplitude and phase components, but the phase component is a nonlinear function of time. If the derivative of the phase is defined as the angular frequency ω(t),

$$\omega(t) = \frac{d\phi(t)}{dt}, \tag{1.18}$$

then its integral is the phase component φ(t) of the signal which can be written as:

$$\phi(t) = \int_0^t \omega(t)dt + \phi_0 \,, \tag{1.19}$$

where ϕ_0 is defined as the initial phase of the source. Accordingly, the electric field can be written as:

$$E(t) = E_0 \exp[-i\phi(t)], \tag{1.20}$$

where E_0 is the amplitude of the electric field. When there is a small angular frequency modulation ($\Delta\omega << \omega_0$), the chromatic dispersion of the medium can be neglected, thus the wave function of an optical FMCW wave can be written as:

$$E(\tau,t) = E_0(l)\exp[-i\phi(t-\tau)], \tag{1.21}$$

where $E_0(l)$ is the wave amplitude that is inversely proportional to the propagation distance, and l is the distance from the light source to the point under consideration. In this case, τ is the propagation time of the wave from the light source to the point under consideration given by:

$$\tau = \frac{l}{v_g} = \frac{nl}{c}, \tag{1.22}$$

whereby v_g is the group velocity, n is the index of refraction of the medium and c is the speed of light in a vacuum. The intensity of the linearly polarized FMCW wave can be represented by[14]:

$$I = \left\langle E(\tau,t)^2 \right\rangle \propto \left| E(\tau,t) \right|^2, \tag{1.23}$$

where < > represents a time average over a period much longer than the optical vibration period. If many optical FMCW waves are recombined to interfere with one another, the intensity of the resulting electric field (which in turn is the beat signal that is measured) will be of the following form[14]:

$$I(\tau_1,...\tau_n,t) = \left\langle \left[\sum_{i=1}^{n} E_i(\tau_i,t) \right]^2 \right\rangle \propto \left| \sum_{i=1}^{n} E_i(\tau_i,t) \right|^2 . \tag{1.24}$$

When considering only a 1st order case (not multiple reflections of the light within the fiber) there will typically only be two linearly polarized optical plane waves interfering at time t at the coupler of an interferometer which is recombining the reference path signal with the FUT path signal. In other words, primarily only $E_1(\tau_1,t)$ and $E_2(\tau_2,t)$ will be interfering at that time t. The intensity of the resulting electric field can be expressed by:

$$\begin{aligned} I(\tau_1,\tau_2,t) &= \left|E_1(\tau_1,t)+E_2(\tau_2,t)\right|^2 \\ &= [E_1(\tau_1,t)+E_2(\tau_2,t)][E_1(\tau_1,t)+E_2(\tau_2,t)]^* \\ &= E_1(\tau_1,t)E_1^*(\tau_1,t)+E_2(\tau_2,t)E_2^*(\tau_2,t)+E_1(\tau_1,t)E_2^*(\tau_2,t)+E_1^*(\tau_1,t)E_2(\tau_2,t), \\ &= E_1^2+E_2^2+2E_1E_2\cos[\varphi(t-\tau_1)-\varphi(t-\tau_2)] \\ &= I_1+I_2+2\sqrt{I_1I_2}\cos[\varphi(t-\tau_1)-\varphi(t-\tau_2)] \end{aligned} \tag{1.25}$$

by subbing (1.21) into (1.24). When the initial phases are correlated/coherent, as is the case when the two waves are derived from the same optical source but travel along different paths (which are less than the coherence length of the source) before they meet, the beating intensity of the electric field will be:

$$I(\tau_1,\tau_2,t) = I_0\{1+V\cos[\varphi(t-\tau_1)-\varphi(t-\tau_2)]\}, \tag{1.26}$$

where I_0 is the average intensity of the resulting field ($I_0=I_1+I_2$) and V is what is termed as the visibility or contrast or the beat signal that is given by:

$$V=\frac{2\sqrt{I_1I_2}}{I_1+I_2}. \tag{1.27}$$

Now remember that τ_1 and τ_2 are the propagation times from the laser source to the points under consideration. Because $\varphi(t-\tau_1)-\varphi(t-\tau_2)=\varphi(t-\tau_1)-\varphi[(t-\tau_1)-(\tau_2-\tau_1)]$, if we shift the origin of the temporal coordinate by τ_1, the intensity of the resulting electric field becomes:

$$I(\tau_1,\tau_2,t) = I_0\{1+V\cos[\varphi(t)-\varphi(t-\tau)]\}, \tag{1.28}$$

where now τ is the delay time of the second wave (the signal wave) with respect to the first wave (the reference wave), given by: $\tau = \tau_2 + \tau_1$.

The first term of the right-hand side of (1.28) which is constant is the DC portion of the interacting fields, which doesn't provide any information. The second term represents the AC (beating) portion of the field interaction and also gives all the location and sensing information of the FUT. Accordingly, one of the parameters to optimize the system is to maximize V or the visibility. As seen in Fig.1.12 below this occurs when the intensity of the two arms, I_1 and I_2 are equal.

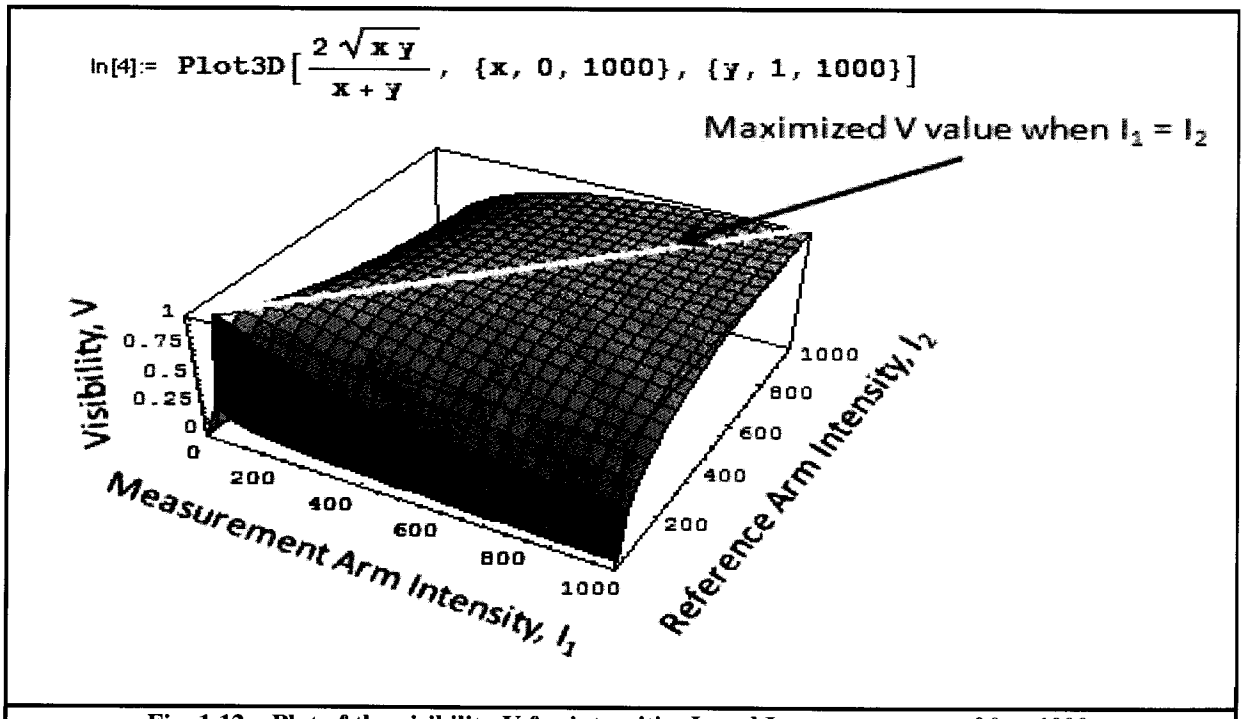

Fig. 1.12 – Plot of the visibility V for intensities I_1 and I_2 across a range of 0 to 1000.

For OFDR setups like that in Fig.1.11 the type of beating signal is dependent on the style of frequency modulation of the laser source. The three main styles of FMCW interference/sweeping are of: saw-tooth, triangle, and sinusoidal types as seen in Fig.1.13.

Throughout the duration of the research on this subject I used 3 tunable lasers: a) New Focus TLB-6600, b) Agilent 8163B/81980A, and the c) Thorlabs ECL5000D. All of which use a sawtooth style of sweeping. Accordingly I shall only look at this style of modulation below.

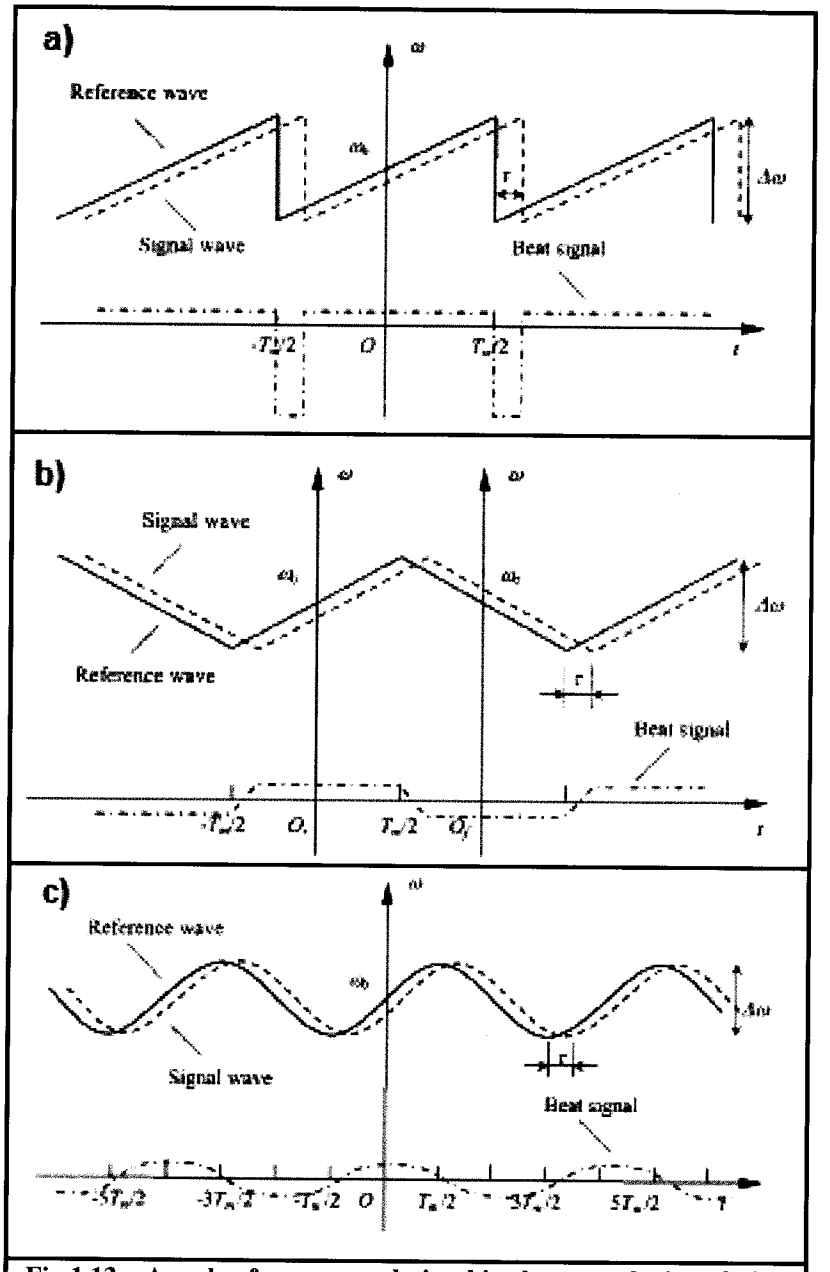

Fig.1.13 – Angular frequency relationships between the interfering waves and the produced beat signal in: a)sawtooth-wave FMCW interference, b)triangle-wave FMCW interference, and sinusoidal-wave FMCW interference respectively. These figures were borrowed from Ref. [14]

1.6.2 Sawtooth-Wave Optical Modulation

When looking at Fig.1.11, if the two optical waves which originated from the same coherent source are modulated with a sawtooth waveform, travel along different paths and are recombined at some point to interfere then the angular frequency waveforms and the beat frequency are as illustrated in Fig.1.13(a) (assuming the path lengths are remaining constant). In this case the solid line represents the angular

frequency of the reference wave, the dashed line stands for the angular frequency of the signal wave, while the dotted-dashed line corresponds to the angular frequency of the generated beat signal. Remembering that $\tau = \tau_2 + \tau_1$ one can say that the angular frequency of the reference wave $\omega_R(t)$ within the period ($-T_m/2 + \tau$, $T_m/2$) can be written as[14]:

$$\omega_R(t) = \alpha t + \omega_C, \tag{1.29}$$

where ω_C is the central angular frequency, and α is the angular frequency modulation rate $d\omega/dt$ or by letting $\Delta\omega$ represent the angular frequency span then:

$$\alpha = \frac{\Delta\omega}{T_m}, \tag{1.30}$$

where T_m is the modulation period. As was the case before with (1.19) we find the phase by taking the integral of (1.29) such that:

$$\phi_R(t) = \frac{1}{2}\alpha t^2 + \omega_C t + \phi_0, \tag{1.31}$$

where ϕ_0 is the initial phase of the source. Thus the electric field for the reference wave $E_R(t)$ will be of the form:

$$E_R(t) = E_1 \exp[-i\left(\frac{1}{2}\alpha t^2 + \omega_C t + \phi_0\right)], \tag{1.32}$$

For the signal wave $E_S(\tau,t)$ we have the following relations[14]:

$$\omega_S(\tau,t) = \alpha(t-\tau) + \omega_C, \tag{1.33}$$

$$\phi_S(\tau,t) = \frac{1}{2}\alpha(t-\tau)^2 + \omega_C(t-\tau) + \phi_0, \tag{1.34}$$

$$E_S(\tau,t) = E_2 \exp[-i\left(\frac{1}{2}\alpha(t-\tau)^2 + \omega_C(t-\tau) + \phi_0\right)], \tag{1.35}$$

When (1.32) and (1.35) recombine as in (1.25) the measured beating signal can be written as follows:

$$
\begin{aligned}
I(\tau,t) &= \left|E_1(t) + E_2(\tau,t)\right|^2 \\
&= \left[E_1(t) + E_2(\tau,t)\right]\left[E_1(t) + E_2(\tau,t)\right]^* \\
&= E_1(t)E_1{}^*(t) + E_2(\tau,t)E_2{}^*(\tau,t) + E_1(t)E_2{}^*(\tau,t) + E_1{}^*(t)E_2(\tau,t) \\
&= E_1{}^2 + E_2{}^2 + 2E_1E_2\cos\left(-\frac{1}{2}\alpha\tau^2 + \omega_C\tau + \alpha\tau t\right) \\
&= I_1 + I_2 + 2\sqrt{I_1I_2}\cos\left(-\frac{1}{2}\alpha\tau^2 + \omega_C\tau + \alpha\tau t\right) \\
&= I_0\left[1 + V\cos\left(-\frac{1}{2}\alpha\tau^2 + \omega_C\tau + \alpha\tau t\right)\right]
\end{aligned}
\quad , \qquad (1.36)
$$

For most of the experiments carried out $\tau \approx 50ns, \alpha \approx \omega_C$, so the term $\alpha\tau^2/2$ can be ignored in (1.36). Thus (1.36) can be simplified to the following form[14]:

$$
\begin{aligned}
I(\tau,t) &= I_0\left[1 + V\cos(\omega_C\tau + \alpha\tau t)\right] \\
&= I_0\left[1 + V\cos(\omega_B t + \phi_B)\right]
\end{aligned}
\quad , \qquad (1.37)
$$

where $\omega_B = \alpha\tau$ is the beating signal's angular frequency and ϕ_B is the beating signal's initial phase.

In the period of ($-T_m/2$, $-T_m/2 + \tau$), as mentioned above $\tau \approx 5x10^{-8}s$, which compared to T_m (being 1 to 5 seconds in duration) contributes very little to the overall sweep period. Accordingly we can treat the whole sweep period of ($-T_m/2$, $T_m/2$) as approximately that found in (1.37). Across the whole time domain ($-\infty,\infty$) the signal at the detector can be viewed as the convolution of (1.37) with an impulse function[14]:

$$
I(\tau,t) = I_0\left\{1 + \left[VT_m\cos(\omega_B t + \phi_B)W_{T_m}(t) \otimes \sum_{n=-\infty}^{\infty}\delta(t - nT_m)\right]\right\}, \qquad (1.38)
$$

where:

$$
W_{T_m}(t) = \begin{cases} 1/T_m, |t| \le T_m/2 \\ 0, |t| > T_m/2 \end{cases}.
$$

Since the optical path difference, x along the FUT is equal to $c\tau$, and we know the relationships of frequency (Hz) is $\upsilon = 2\pi\omega$, as well as we know that $\lambda = 2\pi c/n\omega$ so putting (1.37) into more usable experimental units we have:

$$I(x,t) = I_0\left[1 + V\cos\left(\frac{2\pi\Delta\upsilon nx}{T_m c}t + \frac{2\pi}{\lambda_C}x\right)\right], \tag{1.39}$$

It should be noted that all of the calculations listed above are for the interaction (and beating) of just two electric fields. One from the reference arm and the other from the measurement arm of the interferometer. This approximation justified when either of the following two conditions are met: **a)** both signals are transmission portions of the original field, or **b)** the measurement arm signal recombines with the reference arm signal after having reflected off of a mirror or very strong Fresnel reflector. For most sensing this is rarely the case unless it is to analyze the status of a portion of a network optical cable and there is a bad break on the line. For this thesis though, the FUT's are of either multiple FBG's in series (or in parallel), as well as using the minute Rayleigh backscatter in a standard SMF-28 fiber. In this case there are not two fields interacting and beating, but the superposition of n fields which are separated by different τ_n values. This shall be addressed in the next subsection.

1.6.3 Measuring Rayleigh Backscattered Light using OFDR

As was specified in (1.24):

$$I(\tau_1,\ldots\tau_n,t) = \left\langle\left[\sum_{i=1}^{n} E_i(\tau_i,t)\right]^2\right\rangle \propto \left|\sum_{i=1}^{n} E_i(\tau_i,t)\right|^2. \tag{1.40}$$

The analysis could be carried out for many reflections (time delays τ) as was done above but becomes very cumbersome very quickly. Accordingly the more sensible strategy is to treat the beating signals measured at the detector in more of a statistical nature. To do this we will

express some of these terms in integral form. To simplify, I shall re-define a few terms. Looking at Fig.1.11 let the reference arm be of length x_0. Let the starting position of the FUT be also defined as x_0 on the measurement arm. If we define $x_0 = 0$, then any backscattering and/or reflections at arbitrary elements dx at position x in the FUT shall have a time delay of: $\tau = 2x/v_g = 2nx/c$. As well, during this time delay the optical tuning frequency shall change by: $\Omega = \tau(d\omega/dt)$. This differential frequency between the two arms is what can be seen using a photodetector and spectrum analyzer. Converting this into units of Hz and using experimental parameters we have the following:

$$\begin{aligned} v_{BEAT} &= \frac{\Omega}{2\pi} = \frac{\tau}{2\pi}\left[\frac{d\omega}{dt}\right] = \frac{2x}{2\pi v_g}\left[2\pi\frac{dv}{dt}\right] = \frac{2nx}{c}\left[\frac{c(\Delta\lambda/dt)}{\lambda_C{}^2}\right], \\ &= 2nx\frac{(\Delta\lambda/\Delta t)}{\lambda_C{}^2} \end{aligned} \tag{1.41}$$

Where λ_C is the central wavelength of the sweep (in nm), $\Delta\lambda/\Delta t$ is the sweeping speed in nm/s, and n is the index of refraction of the fiber (approximately 1.4682 for SMF-28e fiber). Now let L represent the maximum length of the FUT. When looking at (1.41) since λ_C is constant, n is constant and $\Delta\lambda/\Delta t$ is relatively constant then we can extrapolate the relationship of:

$$\frac{v_{BEAT}}{v_{MAX}} = \frac{|x - x_0|}{L}, \tag{1.42}$$

Based on such, the whole FUT spatial profile can be found by measuring the sweep beating profile using a spectrum analyzer. As well the amplitude distribution is proportional to the local backscattering coefficient and optical power - so it describes the signal attenuation with respect to distance x.

As before we shall consider a lightwave of the amplitude E_0 that's coupled at the position $x = x_0 = 0$ in a FUT of length L. The electric field amplitude distribution along the

fiber can be treated as: $E(x)\exp(-i\beta x)$, where β is the propagation constant and $E(x)=\sqrt{a(x)}\cdot E_0$ is the real amplitude whereby *a(x)* is the attenuation function defined by[11]:

$$a(x)=\exp\left[-\int_0^x \alpha(\xi)d\xi\right], \tag{1.43}$$

which is to be determined from the measurement data. The superposition of all Rayleigh backscattered light that comes from a fiber element *dx* with a localized scattering coefficient σ(x) contributes an amplitude of $E(x)\sigma(x)dx$ to the overall backscattered wave of $E_S(x)$. Thus the total backscattered amplitude coming from the entire FUT is[11]:

$$E_S(\beta)=E_0\int_0^L \sigma(x)a(x)\exp(2i\beta x)dx\ . \tag{1.44}$$

The laser frequency is linearly** swept, so the propagation constant is assumed to be of the form: $\beta(t)=\omega(t)/\upsilon_g=\beta_0+\gamma t$ where $\gamma=(1/\upsilon_g)d\omega/dt$ is the sweep rate. The reference wave is of the form:

$$E_R(\beta)=rE_0a(x_r)\exp(2i\beta x_r)\ , \tag{1.45}$$

which when looking at Fig.1.11 is produced by a reflection of the forward wave in the reference arm from the Fresnel reflector at position $x_r = x_0$ with a known amplitude reflection coefficient *r*.The fields listed in (1.44) and (1.45) above then interfere with one another and the result as described in (1.25):

$$\begin{aligned} I(\beta)&=\left|E_S(\beta)+E_R(\beta)\right|^2 \\ &=\left[E_S(\beta)+E_R(\beta)\right]\left[E_S(\beta)+E_R(\beta)\right]^* \\ &=\left|E_R\right|^2+\left|E_S\right|^2+E_R(\beta){E_S}^*(\beta)+{E_R}^*(\beta)E_S(\beta) \end{aligned}\ , \tag{1.46}$$

**** Note: these derivations assume that it is a linear sweep (ie – γ is constant). The next subsection will deal with the case of nonlinear sweeping.**

Looking on the right-hand side of (1.46), the first two terms represent the DC portion and are not dependent on β, whereas the other two terms represent the AC (beating) portion and are β dependent. The normalized backscattered signal can be expressed as: $E(\beta) = E_S(\beta)/E_R(\beta)$. The normalized AC portion of the signal can be treated as $2 \cdot Re\{E(\beta)\}$. If we suppress the β_0 portion of the $\beta(t) = \omega(t)/v_g = \beta_0 + \gamma t$ and combine (1.44) and (1.45) we have[11]:

$$E(\gamma t) = \int_0^L E(x)\exp[-2i(x - x_r)\gamma t]dx, \tag{1.47}$$

$$E(x) = [\sigma(x)a(x)/ra(x_r)]\exp[-2i\beta_0(x - x_r)]. \tag{1.48}$$

Looking at Eq.(1.47) one is able to see that the backscattered signal from a location x contributes to the total AC signal at the detector by the component of $E(x)dx$ and the angular frequency value of $\Omega = 2\gamma|x - x_r|$. This is the beating frequency of the measurement arm and reference arm signals that come from points x and x_r respectively.

The angular beating frequency Ω is not only dependent on x, but also on the reference point x_r. As before, if we let $x_r = x_0 = 0$ then the maximum frequency $\Omega_m = 2\gamma t$. Accordingly each position on the fiber is associated with the frequency $\Omega/\Omega_m = v/v_m = x/L$ which can observed using a spectrum analyzer.

The Eq. (1.47) can be viewed as the inverse Fourier transform of the spectral function $E(\Omega) = E(2\gamma|x - x_r|) = E(x)$. The function $E(x)$ needs to be recovered. This can be done by performing the direct Fourier transform on the measured function $E(\gamma t)$ as follows[11]:

$$E(\Omega) = \frac{1}{2\pi}\int_{-\infty}^{\infty} E(\gamma t)\exp(-i\Omega t)dt. \tag{1.49}$$

Since $E(\gamma t)$ is limited to a short sweep interval $(0 < t < \Delta t)$ during which $\Delta\omega = \gamma\Delta t$, the interval must be truncated to what is equivalent of multiplying $E(\gamma t)$ by a rectangular impulse

shaped function of width Δt and unit height before putting it into the integral (1.49). Thus the recovered function $E_r(\Omega)$ is given by the convolution of both spectra:

$$E_r(\Omega) = E(\Omega) \otimes R(\Omega), \tag{1.50}$$

or in spatial coordinates of: $E_r(x) = E(x) \otimes R(x)$. (1.51)

In (1.50) and (1.51), $R(\Omega)$ and $R(x)$ are the spectral functions of the impulse function in the frequency and spatial domains respectively. Since these are sinc functions, one can approximate the spatial resolution by the relations of $\Delta\Omega = 2\pi/\Delta t$ and $\Delta x = 2\pi/\Delta\beta$. Thus it is not possible to recover multiple reflections in the fiber that are separated by distances smaller than Δx.

The convolutions listed in (1.50) and (1.51) are the same as those listed in (1.38). Experimentally, as will be discussed in the next chapter, the convolution is already taken care of since the data is only acquired during the gated sweep period of Δt. The above process is rehashed again in Chapter 3 using FFT's and FFT^{-1}'s, as well as further subsequent steps needed to extract the spectral response from specific locations used in finding the wavelength shifts and accordingly temperature and stress/strain changes at that location.

1.7 External Clocking and Acquiring Data in the Frequency Domain

The theory in the previous section holds true so long as the frequency of the laser is sweeping linear with time. Unfortunately this is never the case. Even the newest tunable lasers on the market have some deviation from linearity. When acquiring the data in the time domain, the more non-linear the sweep is, the more broadened and distorted events become when observing them on a spectrum analyzer. U. Glombitza and E. Brinkmeyer wrote about

a work around to this issue in their 1993 paper [12]. An overview of the main points shall be presented as follows.

We start with the general case as was provided in (1.20) of an initial electric field:

$$E(t) = E_0 \exp[-i\phi(t)], \tag{1.52}$$

with the instantaneous optical frequency of:

$$\omega(t) = \frac{d\phi(t)}{dt}, \tag{1.53}$$

or

$$\upsilon(t) = \frac{1}{2\pi}\frac{d\phi(t)}{dt}. \tag{1.54}$$

One needs to rederive *E(t)* in the spectral domain so as to be able to distinguish between group and phase delays. To do so *E(t)* is expanded as a Fourier integral[12]:

$$E(t) = \int_{-\infty}^{+\infty} e_0(\upsilon)\exp[-2\pi i\upsilon t]d\upsilon. \tag{1.55}$$

For light which travels from the input of the FUT to some backscatter location and then back again the phase of the spectrum $e_0(\upsilon)$ is changed by a factor of $exp[i\beta(\upsilon)2x]$ where $\beta(\upsilon)$ is the propagation constant and x is the point of reflection/backscatter. Performing the inverse Fourier transform on (1.55) to return to the time domain we have[12]:

$$\int e_0(\upsilon)\exp[i\beta(\nu)2x]\exp[-2\pi i\upsilon t]d\upsilon. \tag{1.56}$$

We can evaluate (1.56) by approximating the propagation constant as: $\beta(\upsilon) = \beta(\upsilon_0) + \beta'(\upsilon_0)(\upsilon - \upsilon_0)$. Since $\beta(\upsilon_0)$ and $\beta'(\upsilon_0)$ are related to the phase delay τ_{ph}, and the group delay τ_{gr} respectively a generalized version of the measured beating signal at the detector can be treated as[12]:

$$I = I_0\left[1 + \sum_{n=1}^{N}\{\left|r_{eff}\right|_n^{\,2} + 2\left|r_{eff}\right|_n \cos\left(\phi(t) - \phi(t-\tau_{n\,gr}) + 2\pi\upsilon_0(\tau_{n\,ph} - \tau_{n\,gr}) + \psi_n\right)\}\right], \tag{1.57}$$

where r_{eff} is the effective reflection factor. This can be further simplified by substituting $\phi(t)-\phi(t-\tau_{ngr})$ with $\tau_{ngr}(d\phi/dt)=2\pi\upsilon\tau_{ngr}$. The higher order terms can be neglected if $\tau^2{}_{ngr}(d\upsilon/dt)<<1$, in which most of the experiments carried out in this thesis have a $\tau^2{}_{ngr}(d\upsilon/dt)\cong 0.01$ so this condition holds. As well, since $\phi(t)-\phi(t-\tau_{ngr})$ is not an explicit function of time, the measured signal can be taken as a function of the instantaneous optical frequency υ, such that the AC portion of the signal is[12]:

$$I=2I_0\sum_{n=1}^{N}\left|r_{eff}\right|_n\cos\left(2\pi\upsilon\tau_{ngr}+\xi_n\right). \tag{1.58}$$

Thus no matter what kind of tuning is used, the reflectivity along the fiber can be accurately determined so long as the instantaneous frequency is measured simultaneously during the measurement process. This is used to make *I*, the signal measured at the detector a function of υ. One means of automatically doing so is to use an unbalanced auxiliary Mach-Zehnder interferometer. The output from this, no matter what the linearity of the sweeping speed of the laser is - contains equidistant optical frequency Δυ values that can serve as triggers. These triggers serve as an external clock so as to sample the main photodetector beating signal voltage as a function of Δυ.

If the sweeping speed of the laser is perfectly linear, then the beating signal on the auxiliary interferometer will remain constant. This means that the measurement triggers coming from it will be both equidistant in both the time domain (Δt), as well as in the frequency domain (Δυ). Accordingly this would be the same as just sampling in the time domain and not using the auxiliary interferometer at all for clocking. This can be seen in Fig.1.14(a). Unfortunately, since no lasers can sweep in a perfectly linear fashion the auxiliary interferometer is still needed for external clocking. Even with nonlinear sweeping,

it is still possible to acquire data values which are equidistant (1 beat cycle) in the frequency domain ($\Delta\upsilon$) as is seen in Fig.1.14(b). This essentially means that if the laser sweeping rate increases, more data points will be taken within a given time period. Inversely, if the laser rate decreases then less data points will be acquired during that same time period. This clocking/triggering technique compensates for both nonlinear tuning as well as general phase jumping within the laser cavity.

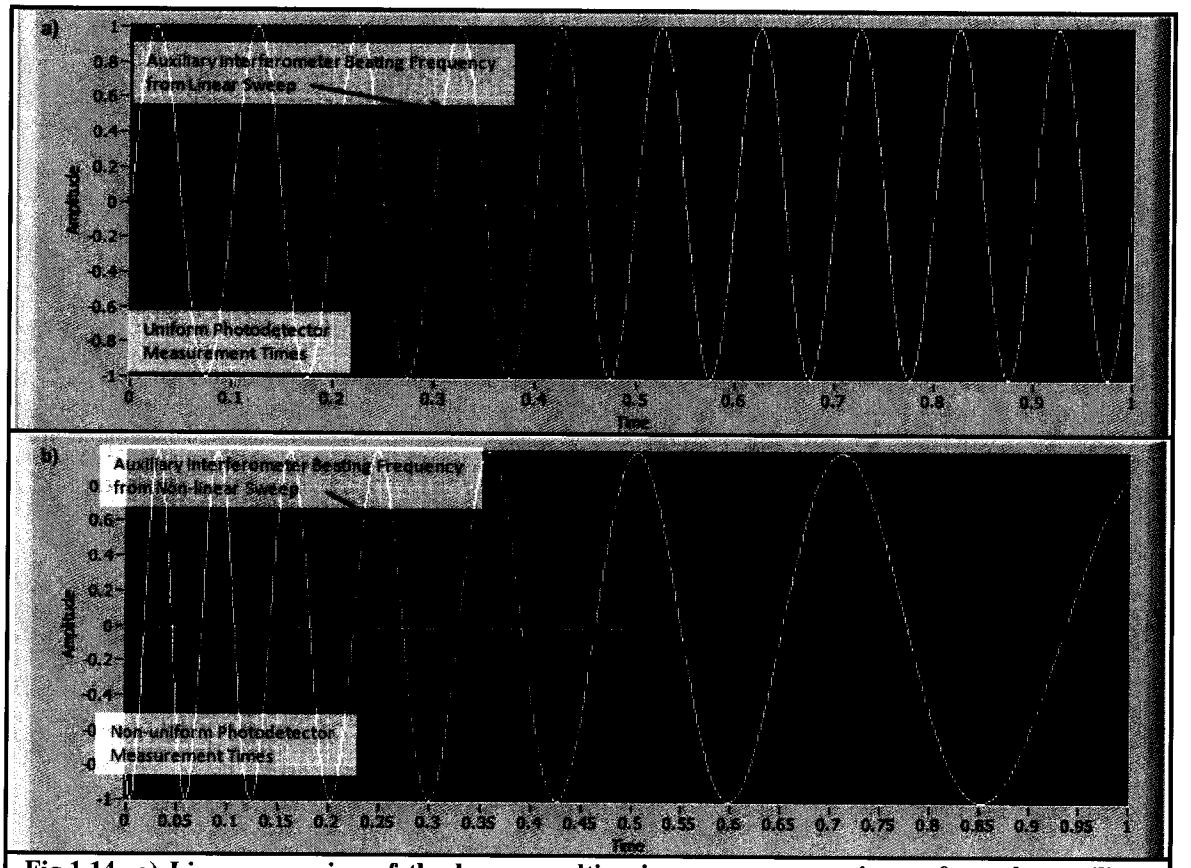

Fig.1.14- a) Linear sweeping of the laser, resulting in measurement triggers from the auxiliary interferometer that are both equidistant in both the time (Δt), and frequency domains ($\Delta\upsilon$). b) The nonlinear sweeping of the laser results in measurement triggers from the auxiliary interferometer being equidistant in the frequency domain ($\Delta\upsilon$) but not in the time domain.

To show the degree of nonlinearity of one of the lasers used in my research, I carried out a typical sweep using the Agilent 8163B/81980A. This was a 20nm tuning range from 1540 to 1560nm. The sweeping rate was 20nm/s so the full duration of the sweep was 1s.

Using a high-speed wavemeter I acquired 200 wavelength measurements during the sweep that were equally spaced in the time domain. The results of this are displayed in Fig.1.15. The red line represents the average value for the sweeps, while the green lines represent the standard deviations. Although Fig.1.15(a) looks like a linear sweep with respect to time,

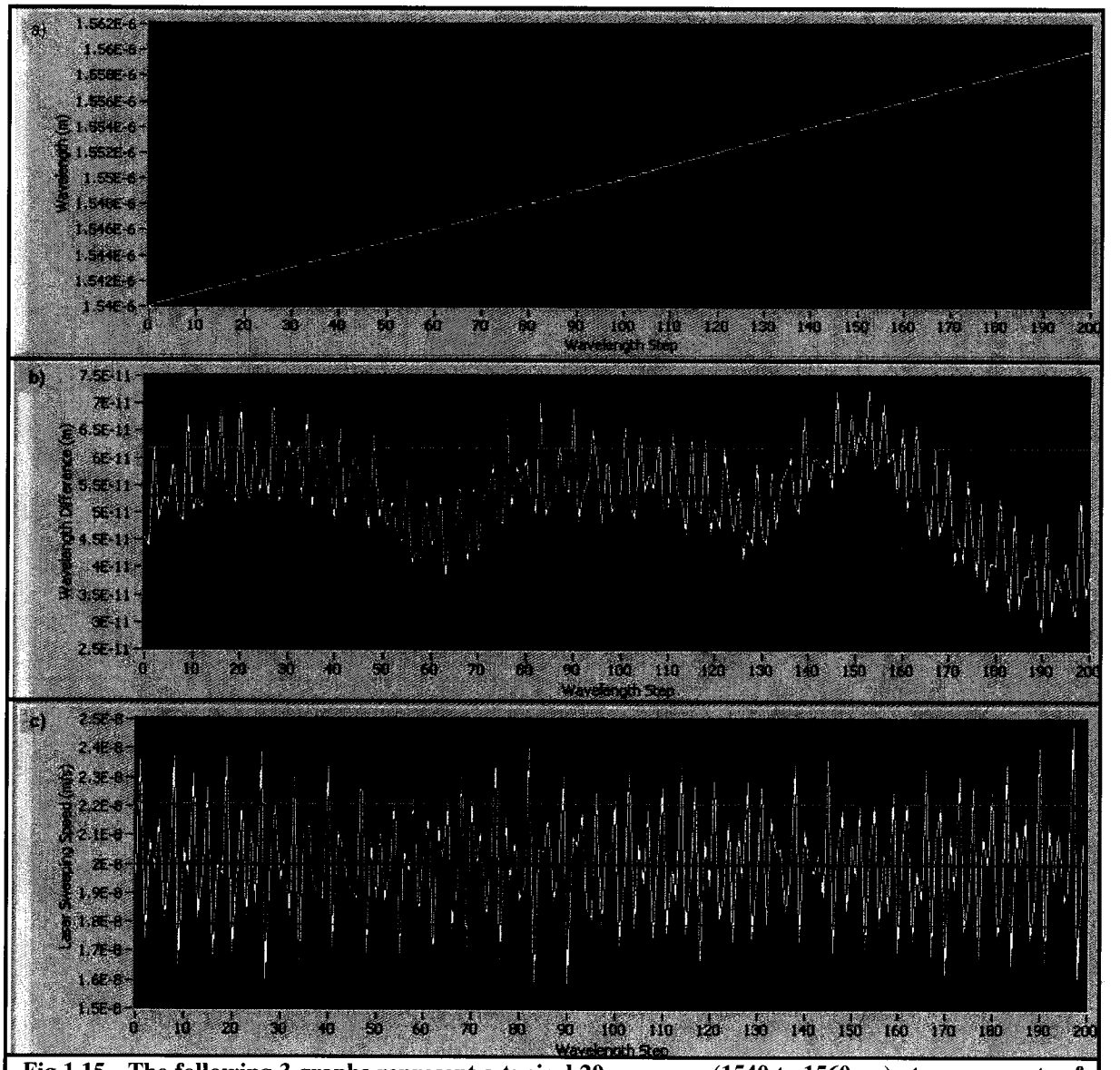

Fig.1.15 - The following 3 graphs represent a typical 20nm sweep (1540 to 1560nm) at a sweep rate of 20nm/s of the Agilent 8163B laser used during my research. 200 equally spaced points in the time domain were acquired using a high-speed wavemeter during this 20nm sweep. Fig.A represents the tuning range. Fig.B shows the wavelength values with respect to a perfectly linear sweep while Fig.C shows the deviation in the tuning rate.

Fig.1.15(b) is the same graph but made with respect to a perfectly linear sweep. The standard deviation of the wavelength position with respect to time is 8.99169pm. Fig.1.15(c) is displaying the sweeping speed deviations of this data. Although the average is 19.9929nm/s, very close to the ideal 20nm/s, the standard deviation throughout the sweep was 2.1041nm/s.

1.8 Thesis Summary

This thesis will present a comprehensive study into the performance of OFDR using various types of FUT to measure the three types of stimuli: temperature, longitudinal stress, and torsional stress. Chapter 2 will start off with a general overview of all of the components used in the optical setups; then focus in on the five various measurement schemes studied in my research. These measurement setups are defined as: [(i)]the *Basic*, [(ii)]*Polarization Diverse*, [(iii)]*Balanced*, [(iv)]*Quadrature Interferometer*, and [(v)]*Differential Quadrature Interferometer* schemes respectively. This chapter finishes off with a performance comparison of each in the time/spatial domain.

Chapter 3 continues on where §1.6 and §1.7 left off. It discusses the hereditary shortcomings of the classical OFDR analysis – particularly in the spectral domain in which it puts a resolution limit on the measurement of the wavelength shifts for specific segments of the FUT of 13.22 points/nm, or inversely 75.6 pm/point. For a 1cm segment this spectral resolution corresponds to approximately an 8.3°C temperature sensing resolution. To try to improve the spectral resolution and accuracy I will present the four novel data analysis algorithms of: [(i)]the *Fourier Interpolation Algorithm*, [(ii)]the *Extended Optical Sweep Range Algorithm*, [(iii)]the *Boxcar Filter Algorithm*, and [(iv)]the *Extended Segment Size Algorithm.*

Chapter 4 goes into detail of using SMF-28 fiber as the FUT to sense the external stimuli of temperature, longitudinal stress, and torsional stress separately using the Polarization Diverse as well as with the Differential Quadrature Setup – which was the best performing out of the five optical schemes.

Chapter 5 covers my research collaboration with NRC-IFCI to do 'In-situ Mapping of Temperature Distribution Inside a PEM Fuel Cell' using embedded SMF-28 fiber was well as linear FBG's. It also includes subsequent experiments doing temperature measurements using both linear FBG's, as well as with chirped FBG's; finishing off the chapter with a performance comparison of linear and chirped FBG's along with SMF-28 fiber.

I close off my research in Chapter 6 discussing the different methods of system optimization such as: averaging over multiple sweeps, variation of the optical linewidth of the source, and increasing the optical tuning range. I also will briefly discuss a means of differentiating temperature stimulus from stress/strain along the FUT, as well as when using the polarization diverse configuration - discuss how the PBS response affects the SNR depending on the amount of elliptically polarized light is in the system.

In Chapter 7 I shall finish off by re-summarizing all of my results as well as discussing possible future work.

Chapter 2

Experimental OFDR Setups and Their Components

2.1 General Experimental Setup Overview

The purpose of this chapter is to go through a detailed overview of all of the variations of my experimental setup and the components therein. This section will give a general overview of the ***basic setup***. The subsequent sections will focus in more on the lasers used, the auxiliary interferometer, the variable coupler, and the measurement/detection schemes respectively. The last section will do a comparison between the different detection schemes with regards to the SNR's in the time domain.

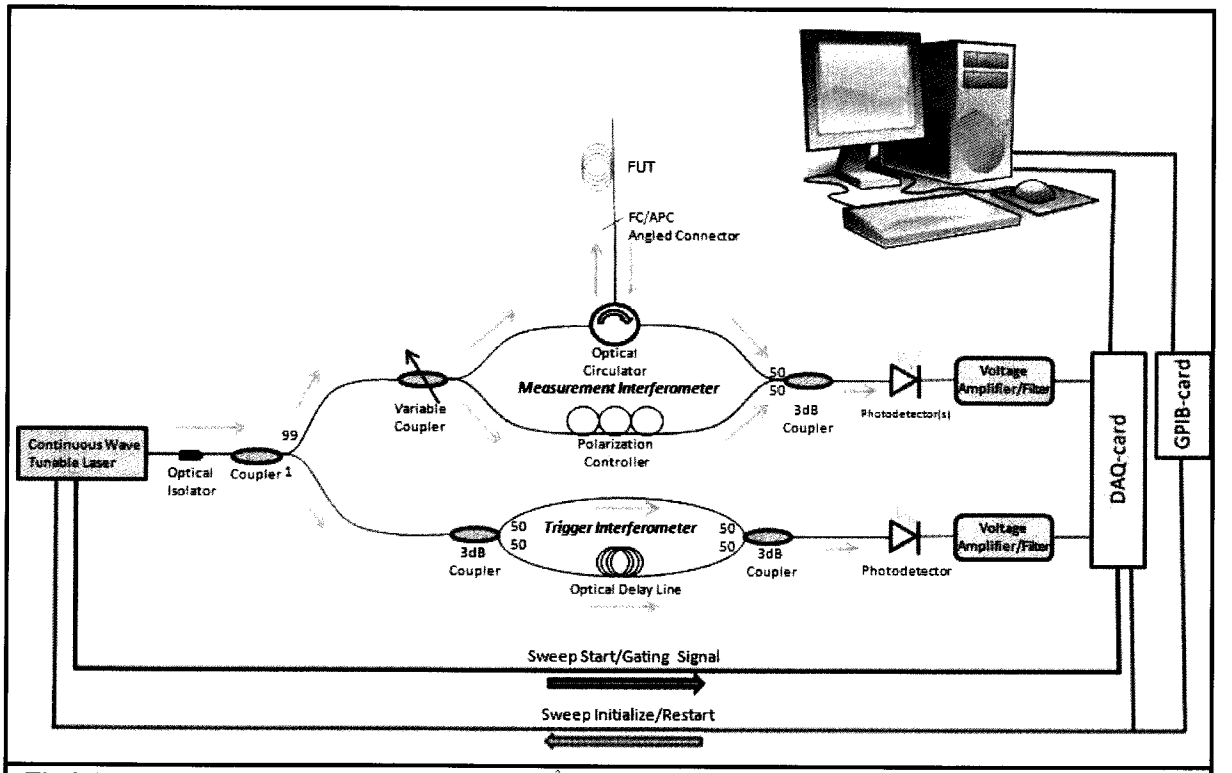

Fig.2.1 – A *generalized* version of the basic experimental setup built and used for the research presented herein.

The diagram above is a generalized version of that used throughout my research. A command is sent from the computer to the laser to sweep between a specific wavelength

range $\Delta\lambda$, at a specific rate $\Delta\lambda/\Delta t$. The light from the laser passes through an optical isolator which is used to keep any back-reflected light out of the laser cavity that could affect its stability. From the isolator it enters into a 1x2 coupler where it is split into the ratio of 99/1. The 1% signal travels down to an auxiliary interferometer (with a delay line in one of the arms) whereby a beating signal is created which has a frequency that is proportional to both the length of the delay line as well as the sweeping speed of the laser. This beating signal is then converted to a voltage signal at a photodetector, is amplified/filtered before being measured by the DAQ-card and serving as an external clock for acquisition of the other data channels.

The other 99% of the light travels to the measurement interferometer where it enters in through a variable coupler. Depending on the FUT used, one is able to adjust the output ratio to maximize the visibility for the interferometer (1.26-1.27). From here a portion of the light travels through a reference arm with a paddle polarization controller used to make the polarization of the light in that arm approximated 50/50 between the s and p-states. The rest of the light travels up through a measurement arm where it enters port 1 of an optical circulator. This light exits port 2 of the circulator and travels up into a fiber under test (FUT). The light that gets back-reflected by Fresnel reflection points and/or experiences general Rayleigh backscattering travels back down through port 2 to exit out port 3 of the circulator. This back-reflected/backscattered signal recombines with reference arm signal via another 1x2 50/50 coupler to create another beating signal with a complex response specific to that particular FUT. As before, this signal is then converted to a voltage signal at photodetector(s), potentially passing through additional amplification and filtering electronics before being measured by the DAQ-card that has measurement times based on the

auxiliary interferometer/external clock. As well, during the sweep an electronic TTL signal is output from laser that has a high state (2.5V) width which is the duration of the sweep $\Delta\lambda$. This TTL signal is used to gate the data acquisition such that only data is acquired while the TTL is in the high state (aka – the instantaneous wavelength λ of the sweep is only in the range of $\lambda_{init} \leq \lambda \leq \lambda_{final}$). This is electronically equivalent to performing the convolution of an impulse function as shown in (1.50-1.51).

Once the sweep has completed this data is transferred to the computer and analyzed using a LabVIEW program. Once the analysis is complete, the program sends a command to the computer (either via GPIB or using an analog output pulse depending on the laser) to the given laser to start another sweep and repeat the process as is required.

2.2 Lasers, DAQ-cards, Gating and Signal Amplification/Filtering

2.2.1 Lasers

Throughout the course of this research, three different tunable laser systems were used. These are the New Focus TLB-6600-H-CL, Thorlabs TXP-ECL5000D, and Agilent 8163B/81980A lasers. Main features of these lasers can be found in Tables 2.1 & 2.2 below:

Table 2.1 – OFDR Laser Tuning Range, Rate, Linewidth and Coherence Length Specifications

Name/Model	**λ Sweeping Range (nm)**	**λ Sweeping Rate (nm/s)**	**Linewidth (kHz) $\Delta\upsilon_c$**	**Coherence Length (m) $\Delta L_c = c/2\Delta\upsilon_c$**	**Max. Beating Freq. per Length (Hz/m)**
New Focus TLB-6600-H-CL	1520-1630	2 - 2000	75	2000	2.5MHz*L
Agilent 8163B/81980A	1465-1575	0.5 – 50	100 - 50000	1500 – 3	62.5kHz*L
Thorlabs TXP-ECL5000D	1519-1630	0 - 130	150	1000	162.5kHz*L

Table 2.2 – OFDR Laser Optical Power, Trigger Out, Computer Control Specifications			
Name/Model	**Optical Power (dBm/mW)**	**Trigger Out**	**Computer Sweep Control Interface**
New Focus TLB-6600-H-CL	10dBm (10mW)	TTL of sweep duration	GPIB
Agilent 8163B/81980A	14dBm (25mW)	1μs (sweep start pulse)	GPIB and/or TTL Trigger Input Pulse
Thorlabs TXP-ECL5000D	50nm: 6dBm (4mW) full range: 3dBm (2mW)	TTL of sweep duration	LAN/Ethernet or TTL Trigger Input Pulse

2.2.2 DAQ-cards & Gating

Throughout the period of research two data acquisition cards were used: a) the Acqiris DP240, and b) the National Instruments PCI-6115. The Acqiris DP240 was a 2-Channel, 8-bit resolution card which was capable of using an external variable speed clock

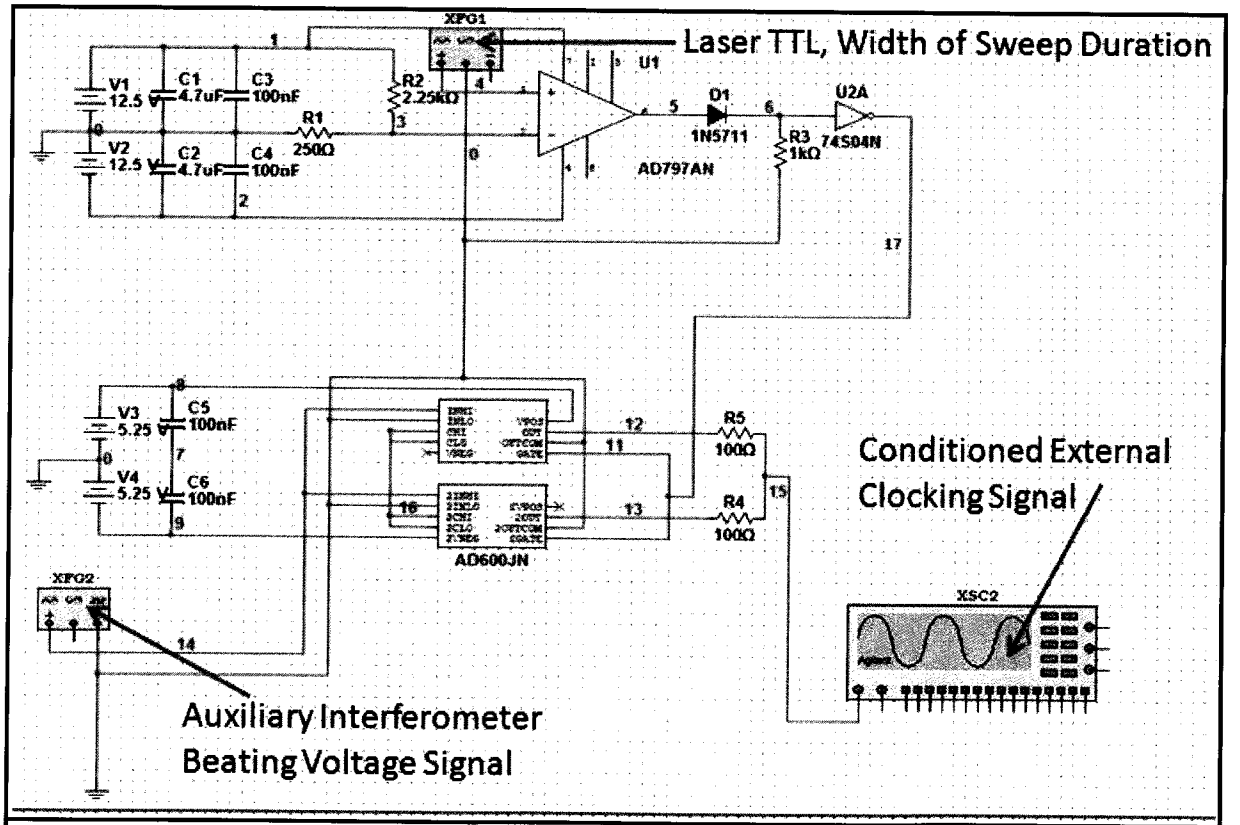

Fig.2.2 – Circuit diagram of the 1st generation external clock signal conditioner/amplifier.

but while doing so it lost the capability of gating (start/stopping) the acquisition. This meant that the acquisition ran constantly even outside of the requested sweeping range whenever there was a beat that was above a specified voltage threshold. Based on such, specialized gating/external clock amplifier circuitry had to be designed to go along with this DAQ-card. The first generation of this circuitry can be seen in Fig.2.2 on the previous page. The signal conditioning can be seen in Fig. 2.5 below:

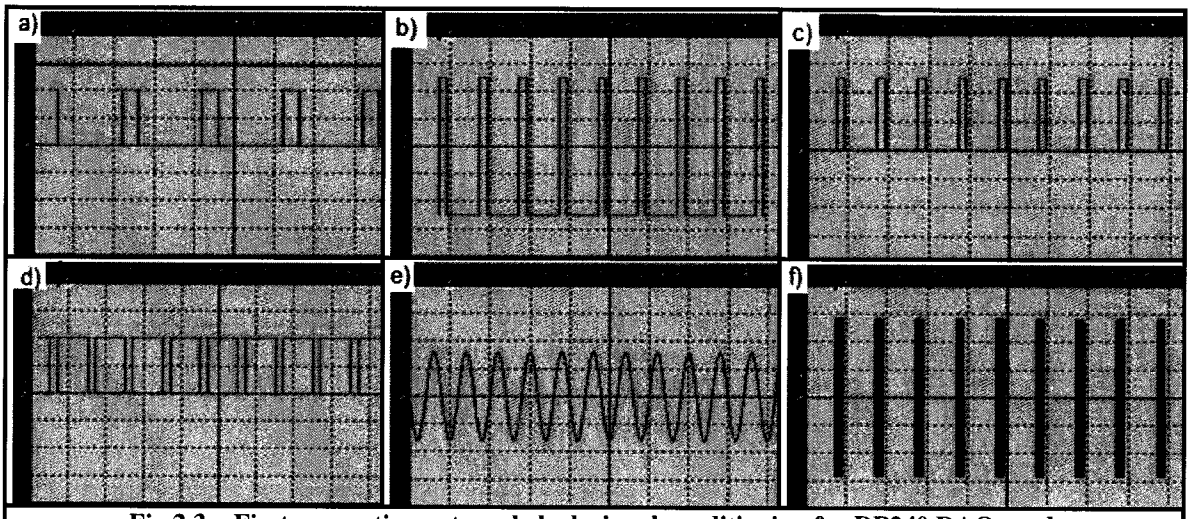

Fig.2.3 – First generation external clock signal conditioning for DP240 DAQ-card.

The laser trigger out TTL that has a width of the sweep duration can be seen in Fig.2.3(a) and is at position 4 on Fig.2.2. This signal enters into a comparator arrangement that goes from one extreme of the power supply for the op-amp to the other when the TTL signal passes through a threshold of roughly 10% of the power supply voltage. In this case that is about 1.25V. This converts the 0 to 2V TTL signal into one that is stretched to +5 and -5V as is seen in Fig.2.3(b) and is the output at location 5 on Fig.2.2. From there the TTL signal is passed through a half-wave rectifier turning it into a TTL with a low of 0V and a high of 5V (Fig.2.3(c)) and is the output at location 6 on the circuit diagram. This then passes through an inverter so that what was 0V in now 4V, and what was 5V is now 0V which is

demonstrated in Fig.2.3(d). This is the signal at location 17 on the diagram. This is then used as the gating input for an Analog Devices AD600 op-amp whereby whenever the gating voltage is < 0.5V the gate is open and ≥ 0.5V it is in a closed state. The beating signal coming from the photodetector of the auxiliary interferometer shown as Fig.2.3(e) is then passed through the inputs of the AD600 op-amp such that the output of the op-amp is the conditioned signal shown in Fig.2.3(f) whereby when the gate is closed the output is 0V and when the gate is open it outputs the beating signal from the external clock with amplitudes of approximately ±3V. Although for the most part this circuit worked quite well, the conditioned output signal contained some extra jitter and noise that came from both the op-amps and their power supplies that at times resulted in extra triggers and data points that were not spaced Δv apart.

To try to improve upon the design (i.e. - lessen the jitter and noise) I created a second generation of the auxiliary interferometer conditioning circuit as it seen below:

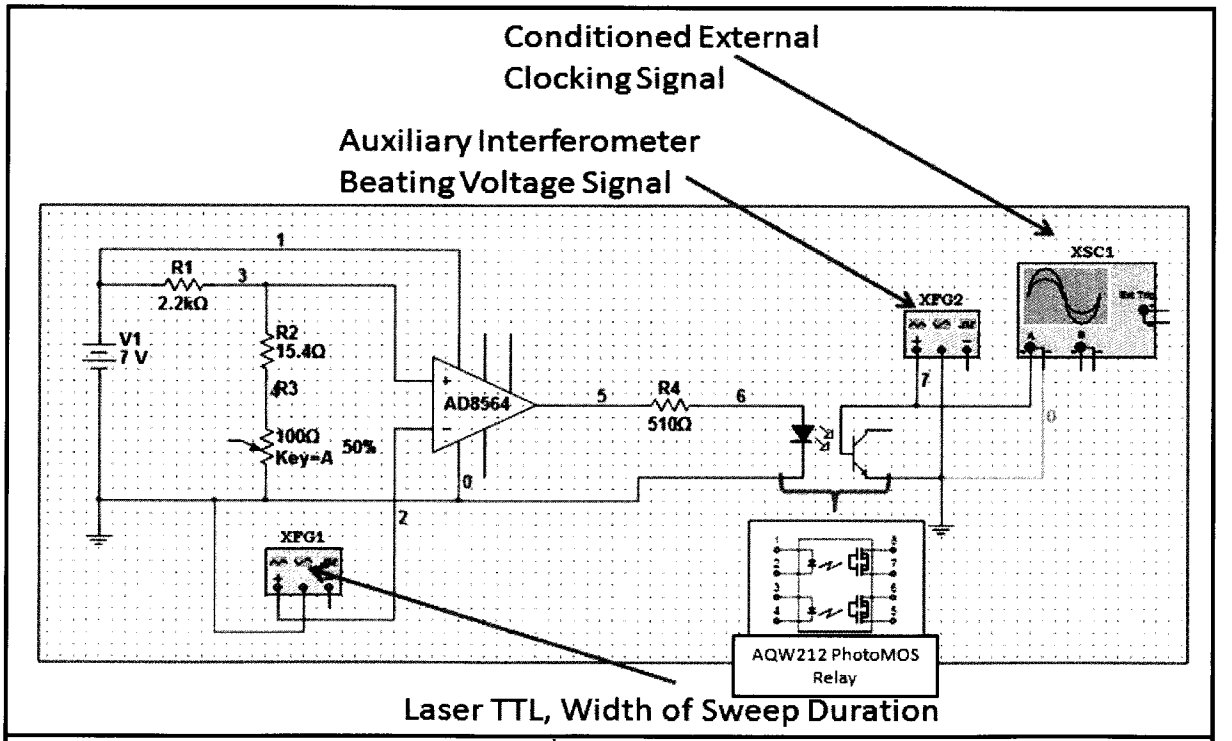

Fig.2.4 – Circuit diagram of the 2nd generation external clock signal conditioner.

The AD8564 component in Fig.2.4 is an integrated, single-sided power supply comparator chip. The AQW212 PhotoMOS relay doesn't require a power supply. This circuit works by inputting the laser trigger out TTL which is the again is the width of the sweep duration. This can be viewed as Fig.2.5(a) and is sent through the negative input of the AD8564 comparator. The positive input of the comparator is a variable voltage from 1 to 5% of the 7V power supply, so from 70mV to 350mV. The output of the comparator is an inverted signal whereby what was 0V is now 4V, and what was 2V was now 0V. This can be seen in Fig.2.5(b). This output drives the photoMOS relay such that on the other side when the beating signal (Fig.2.5(c)) is connected as at 7 on the circuit diagram and the potential is measured across those two pins, when the input TTL is high, the measured potential of the beating signal is almost 0V. At the same time when the TTL input signal is low, the beating signal has the full amplitude. Accordingly, the conditioned external clocking looks as in

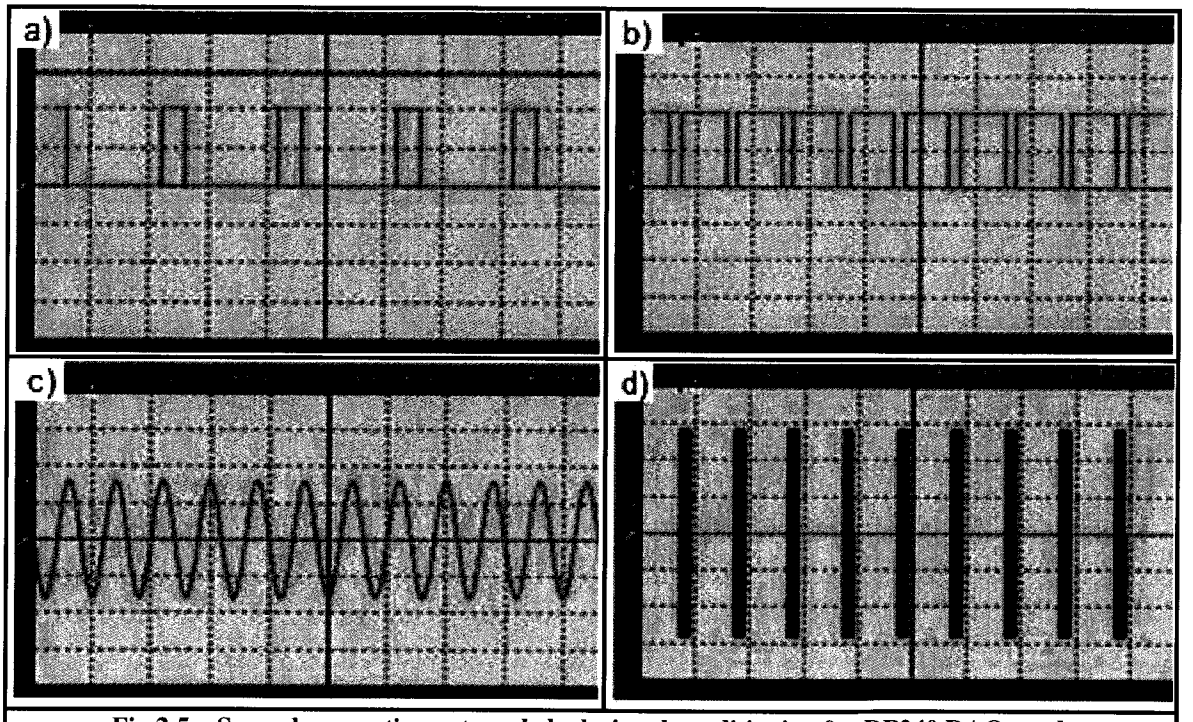

Fig.2.5 – Second generation external clock signal conditioning for DP240 DAQ-card.

Fig.2.5(d). Although this version of the external clock conditioning circuit did not amplify the signal coming from the photodetector of the auxiliary interferometer as was the case of the initial circuit, the much lower noise was worth the tradeoff and performed quite well.

When either of these circuits were used with the New Focus laser a command was sent to the laser via GPIB to do a single sweep. The TTL trigger out from the laser (which had the width of the sweep duration) was then sent out once the sweep began. This TTL pulse in conjunction with the beating voltage from the auxiliary interferometer's photodetector and either of the above circuits created the gated external clock signal that was used for the acquisition of data on the other main channels of the Acqiris card.

On the other hand, when the DP240 was used in conjunction with the Agilent laser an extra step was required. The Agilent laser only output a short microsecond TTL trigger pulse when the sweep started – it was not the duration of the sweep itself. To get around this the trigger output of the laser was sent into the trigger in of an Agilent 33120A function generator. The generator was then programmed to output a TTL pulse that was the width of the sweep duration. This function generator output was then run into the circuits above as before. Even with the function generator being used as a bridge, no noticeable error was introduced because of the fact that a scan usually lasted seconds in duration where the circuitry was fast enough to only exhibit a synchronization delay of about a microsecond.

Later on into the research a National Instruments PCI-6115 data acquisition card was acquired for the research. This card has 4 analog-in channels of 12-bit resolution, 2 analog-outs, a 64 MSample memory, onboard counters and other multifunction hardware. This card has the capability of using one of the analog-in channels for the input of the variable frequency external clock which comes from the photodetector of the auxiliary interferometer.

The TTL trigger out from the laser could also be directly connected to the card's PFI9 pin and programmed to pause the acquisition when it experienced a voltage > 1V. This onboard option basically eliminated the need for the circuits shown in Fig.2.2 and Fig.2.4. As well, when the NI card was used together with the Agilent laser, instead of using the function generator to create a pulse of the sweep duration the trigger out of the laser was alternatively connected to pin PFI2 which is the trigger-in for the onboard counter. The counter was then configured to output a TTL pulse of the sweep duration. This new pulse that was output from pin 2 (counter out) was then re-routed back in through the PFI9 pin and proceeded as before.

The Thorlabs laser which was used for the NRC fuel cell project shall be discussed more in chapter 5. What is important to note though is that over a 40nm sweeping range it had about a 5mW optical power output. This is ½ the power that the New Focus laser has, and about 1/5 the power of the Agilent laser. It is because of this that a larger ratio of the light from the laser needed to be routed to the auxiliary interferometer to have a strong enough beating/external clocking signal. Thus, instead of a 99/1 initial coupler a 90/10 was used for that setup instead. The trigger out configuration for this laser was the same as the New Focus laser, and a PCI-6115 DAQ-card was also used. This negated the need for the external clock gating circuitry.

2.2.3 External Clock/Auxiliary Interferometer Voltage Amplifier

When using either the Agilent or New Focus lasers in conjunction with the PCI-6115 DAQ-card the following voltage amplifier circuit was built for the external clock signal as can be seen in Fig.2.6 on the following page. Since a Thorlabs FPD510 DC photodetector was used for the external clock the signal was first passed though a 10μF capacitor to get rid

of all frequency components < roughly 1.6 kHz. The clocking signal then passed through a non-inverting op-amp configuration that allowed for a 40dB (100x) voltage gain factor. The AD797 also tends to apply a DC offset to its output amplified signal so to get rid of that, I then passed the signal though a high-pass passive filter to eliminate all frequency components < 16Hz. Although relatively simple in design this amplifier works well with one exception. Although the low noise AD797 has a *gain bandwidth* of 110 MHz, when setting the gain to 100 as is the case above, the actual bandwidth of the amplifier drops down to approximately 1 MHz. When a 50m delay line is put into the auxiliary interferometer (so up to a 12.5m FUT) it means that the maximum allowable sweep rate of the laser is 20nm/s. This creates a beating frequency of 1.2 MHz, any faster than this and the amplified clocking signal drops off quickly and no longer is an acceptable clocking source with respect to amplitude. One work around for this is to put two of the AD797's in series with one another and configure each for a gain of 10. This still gives the same amplification but now allows for a 6 MHz bandwidth which then allows for sweep rates up to 100nm/s for that same 50m delay line. For the NRC project the clocking amplifier used was a commercial Mini-Circuits ZHL-32A amplifier which had a high bandwidth range from 50kHz to 130MHz and applied a 25dB gain.

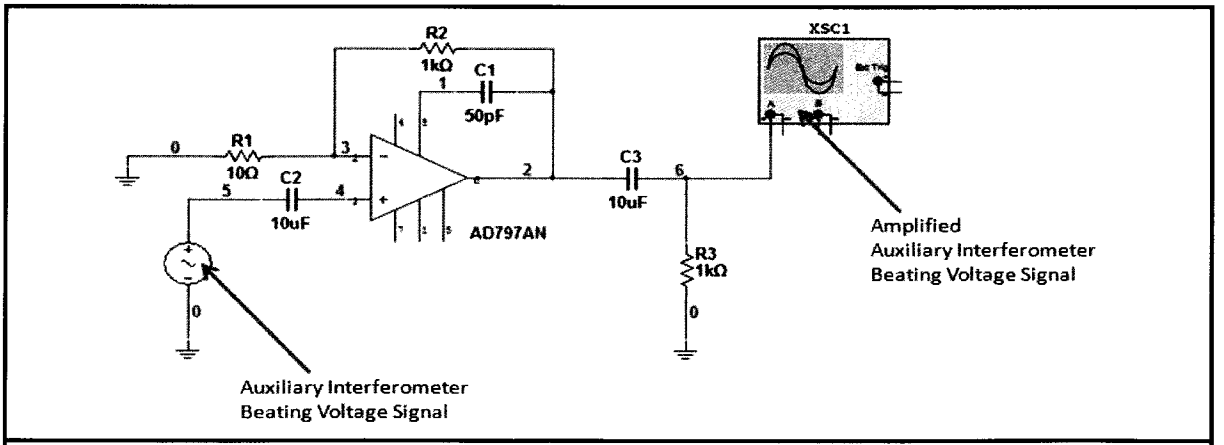

Fig.2.6 – Circuit diagram for external clock voltage amplifier.

2.2.4 Measurement Interferometer Voltage Amplifier(s) and Filtering

For the beating signals emerging from the measurement interferometer, when the Agilent or New Focus lasers were used the voltage signals that came out of the corresponding photodetector(s) were large enough that extra amplification was not needed. The PCI-6115 cards that were measuring these signals were set to AC coupling as well as had the 500kHz onboard low-pass filter turned on. As for the when Thorlabs laser was used, because of the weaker signal (< 5mW) as well as from using the 90/10 coupler instead of the 99/1, voltage amplifiers were used for the beating signals coming from the measurement interferometer. It ended up being the HVA-10M-60-B commercial amplifiers from Femto that were used. These amplifiers had a very low input noise of 0.9nV/√Hz, a switchable gain between 40dB (100x) and 60dB, switchable between AC & DC coupling and a bandwidth from DC-10MHz. For most of the experiments carried out during the project the onboard 500kHz low-pass filter was also used on the DAQ-card.

2.3 Auxiliary Interferometer/External Clock

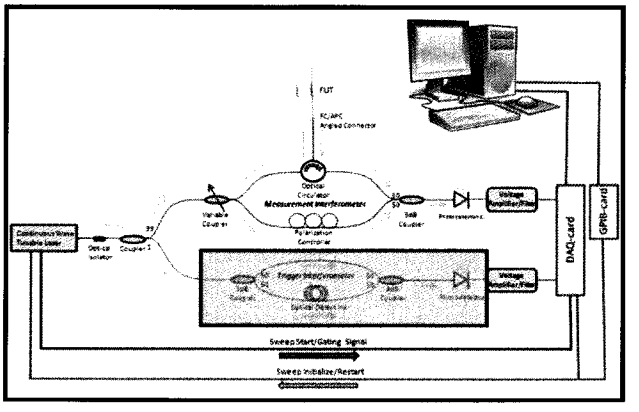

The theory of the auxiliary interferometer/external clock was provided in §1.7. From an experimental standpoint though, the main thing to know is its relationship to the FUT and the means of calculating the average beating frequency of the signal that emerges from it. As was mentioned in Eq.1.41:

$$\upsilon_{BEAT} = 2nL\frac{(\Delta\lambda/\Delta t)}{\lambda_C^{\,2}}, \tag{2.1}$$

where L represents the maximum length of the fiber under test that you wish to observe. To be able to measure this whole FUT length, then the length of the delay line must be at least 4 times greater. This factor of four is due to the Nyquist frequency sampling theorem requirement (factor of two), as well as the double-pass nature of the measurement interferometer since the signal in the FUT is back-reflected/backscattered as opposed to transmission. Another way of putting this is if we let τ represent the optical time delay in the auxiliary interferometer then: $L_{\max} = c\tau / 4n$, where L_{max} is the maximum length of the FUT. For most of my experiments I used a 50m optical delay in my auxiliary interferometer. This meant that the maximum allowable FUT I could use was 12.5m.

2.4 Tunable Directional Coupler

The tunable directional coupler that was used in these experimental setups

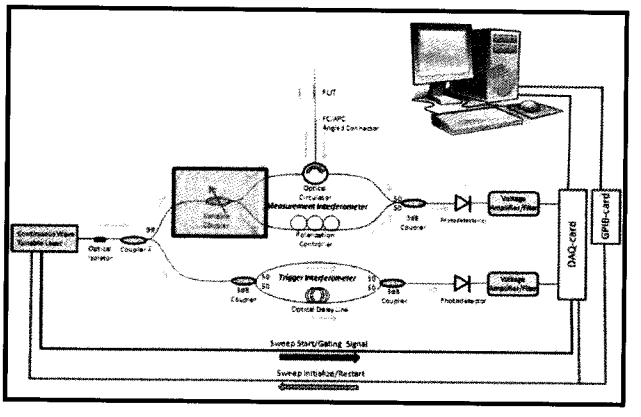

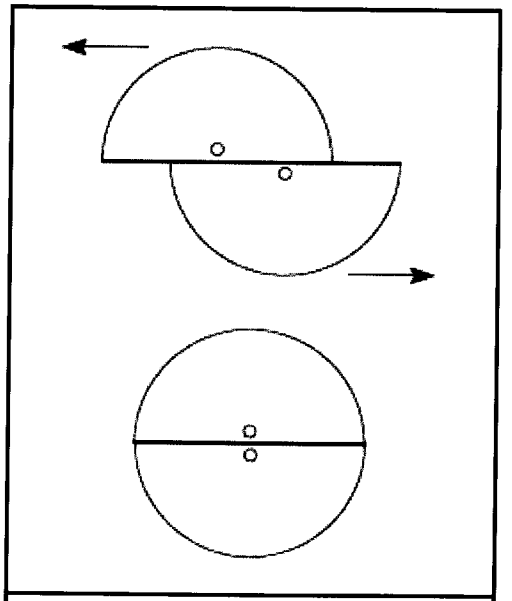

Fig.2.7 – Tunable directional coupler: (top) minimum coupling, (bottom) maximum coupling.

was the Newport F-CPL-155-N-FP. This fiber optic device performs the same function as bulk optic beam splitters with a controllable splitting ratio via a micrometer. The coupling of the light takes place by putting two fiber cores close together such that one can get evanescent field coupling. Controlling

of the ratio is carried out by adjusting the relative lateral position of the fibers via a micrometer. A thin layer of index matching gel is inserted in between the fibers to improve the coupling. Since all the inputs and outputs of this coupler are spliced into the setup the insertion loss is very low (< 0.1dB). The internal workings of this is demonstrated in Fig. 2.7. Typical splitting ratios for the two arms with respect to micrometer positions can be seen in the table below:

Table 2.3 – Micrometer position versus splitting percentage of the tunable coupler for the two arms of the measurement interferometer

Micrometer Position	Measurement Arm Percentage	Reference Arm Percentage
0.5	99	1
20	95	5
24	90	10
33	80	20
39	70	30
44	60	40
47.2	50	50

The visibility definition was given in (1.27):

$$V = \frac{2\sqrt{I_{FUT} I_{REF}}}{I_{FUT} + I_{REF}}. \tag{2.2}$$

As was mentioned back on Pg.19, the AC portion of the measurement interferometer – which is the portion that contains all the useful phase information, is optimized when the intensities of the two arms are balanced and in turn V has the maximum value. The problem is, is that different FUT's (be it SMF-28, linear FBG's, chirped FBG's or other specialty fibers) all have different backscatter/back-reflection profiles. Some FBG's might reflect up to close to 100% of the light for specific wavelength ranges, whereas when using a 100m piece of regular SMF-28 that is attenuated at the other end so as to get very little back-reflection from the cleave the measured backscattered signal can be < 40dB from the input signal. This means that to optimize the measurement interferometer one would have to be constantly

cutting and re-splicing in different ratio input couplers every time they use a different FUT. Using the tunable coupler greatly simplifies this process and shortens the optimization time. Now all that one needs to do is: [(i)]connect the desired FUT, [(ii)] make sure the detector/DAQ-card are set to AC-coupling, [(iii)]start the laser sweeping process to repeat constantly, and [(iv)]adjust the micrometer on a sweep-by-sweep basis so as to find the position whereby the amplitude of the raw incoming data is maximized. In a few minutes the system is optimized for sensing purposes. In general though, when using FBG's for the FUT the ratio is to be set very close to 50/50 where on the other hand when using a piece of standard SMF-28 fiber about 99.5% of the light is sent through the sensing arm and only 0.5% in the reference arm.

2.5 Optical Measurement Schemes

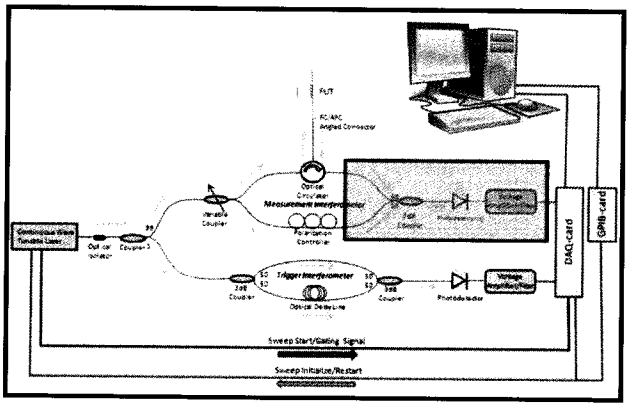

Throughout the course of this research there have been five variants of the measurement schemes. These are: a) a variant on the basic setup as is seen in Fig.1.11, b) a polarization diverse setup, c) a balanced detector version, d) a quadrature interferometer method, as well as a finally e) a *differential* quadrature interferometer scheme. Diagrams, descriptions, and extra theory for each are provided in the following subsections.

Since Eq.1.58 also showed that the beating intensity at the coupler where the two signals recombined can also be a function of frequency, then I shall put it in a slightly more simple form to further express all the measurement signals of the different schemes. To begin with I'll let $\sum_{n=1}^{N}(\xi_n)=\phi(\omega)$ represent the phase response of the complex reflectivity of

the FUT, and $\sum_{n=1}^{N}\left|r_{eff}\right|_n = \rho(\omega)$ represent the amplitude response of the complex reflectivity of the FUT. Thus the general frequency response of the FUT can be written as:

$$F(\omega) = \rho(\omega)e^{-i\phi(\omega)}. \tag{2.3}$$

If we define the initial field sent by the laser as E_{init}, and have the variable coupler set to say 50/50, then when the two signals recombine at the other coupler the sum of the fields would be:

$$E_{BEAT} = \frac{1}{\sqrt{2}}E_{init} + \frac{1}{\sqrt{2}}E_{init}\rho(\omega)e^{-i(\phi(\omega)+\omega(t)\Delta\tau)}, \tag{2.4}$$

where $2\pi\upsilon(t) = \omega(t)$, and $\sum_{n=1}^{N}\left(\tau_{n\,gr}\right) = \Delta\tau$ is the instantaneous angular frequency and the sum of all the time delays respectively. Thus the intensity measured at the detector is proportional to:

$$\begin{aligned}
I &\propto \left|E_{BEAT}\right|^2 \\
&= \frac{1}{2}\left|E_{init}\right|^2 + \frac{1}{2}\left|E_{init}\right|^2\left|\rho(\omega)\right|^2 + \frac{1}{2}\left|E_{init}\right|^2\left(\rho(\omega)e^{-i(\phi(\omega)+\omega(t)\Delta\tau)} + \rho^*(\omega)e^{i(\phi(\omega)+\omega(t)\Delta\tau)}\right) \\
&= \frac{1}{2}\left|E_{init}\right|^2 + \frac{1}{2}\left|E_{init}\right|^2\left|\rho(\omega)\right|^2 + \frac{1}{2}\left|E_{init}\right|^2\left(\rho(\omega)e^{-i(\phi(\omega)+\omega(t)\Delta\tau)} + \rho(\omega)e^{i(\phi(\omega)+\omega(t)\Delta\tau)}\right) \\
&= \frac{1}{2}\left|E_{init}\right|^2 + \frac{1}{2}\left|E_{init}\right|^2\left|\rho(\omega)\right|^2 + \frac{1}{2}\left|E_{init}\right|^2\left(2\rho(\omega)\cos[\phi(\omega)+\omega(t)\Delta\tau]\right) \\
&= \frac{1}{2}\left|E_{init}\right|^2 + \frac{1}{2}\left|E_{init}\right|^2\left|\rho(\omega)\right|^2 + \left|E_{init}\right|^2\rho(\omega)\cos[\phi(\omega)+\omega(t)\Delta\tau] \\
&= I_0\left[1+\left|\rho(\omega)\right|^2 + 2\rho(\omega)\cos[\phi(\omega)+\omega(t)\Delta\tau]\right]
\end{aligned}, \tag{2.5}$$

which is the same as Eq.1.57 where when taking the AC portion of this we have:

$$I_{AC} = 2I_0\rho(\omega)\cos[\phi(\omega)+\omega(t)\Delta\tau], \tag{2.6}$$

that is of the same form as Eq.1.58.

2.5.1 Basic OFDR Measurement Scheme

For the basic OFDR measurement scheme as is shown in Fig.2.8 on the following page, all of the theory that has been covered up to this point applies such that when AC coupled – the signal that is measured at the detector is the same as that given in Eq.2.6 above. This version uses a 2x1, 50/50 coupler to recombine the two arms of the interferometer whereby the combined signal goes directly into a Thorlabs FPD510 photodetector which is a DC detector but the DAQ-card that the voltage signal goes into is set to AC coupled mode. When using the New Focus and Agilent lasers no extra voltage amplification was used.

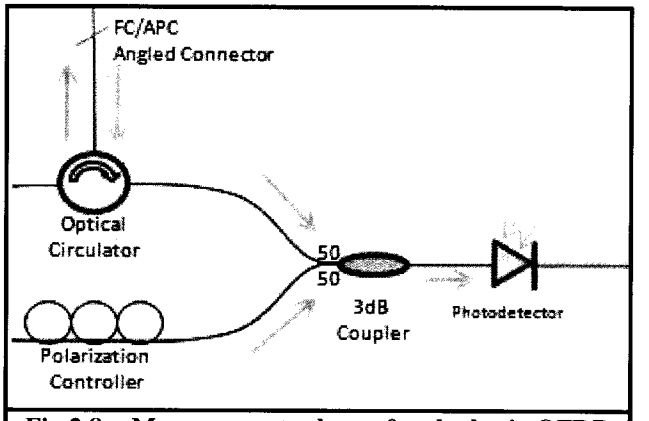

Fig.2.8 – Measurement scheme for the basic OFDR setup.

Table 2.4 – FPD510 Photodetector Specifications	
Spectral Range	850 - 1650nm
3dB Bandwidth	0 - 200MHz
Gain	4 x 10^4 V/W
Dark State Noise Level	-120 dBm
NEP	6 pW/$\sqrt{Hz}$
Coupling	DC

2.5.2 Polarization Diverse OFDR Measurement Scheme

The polarization diverse measurement scheme has been widely used for many years. Going back through being used in open beam optics,

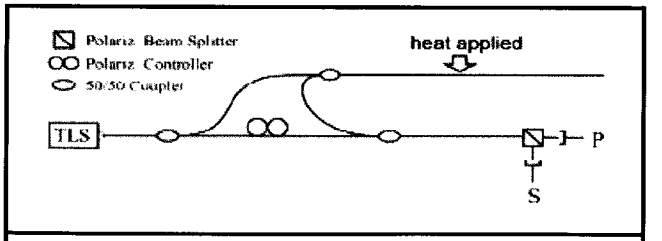

Fig.2.9 – Experimental polarization setup used by Soller, Froggat et al. [18-20]

and then making the transition over into many OCT style setups. With regards to fiber optic based OFDR, Mark E. Froggatt *et al.* widely popularized this configuration as is seen in Fig. 2.9 in several papers [18-20]. The main differences between my polarization diverse setup and theirs boils down to optimization. Their setup was originally designed for network characterization. In the case of strong back reflecting components and/or break detection almost all of the light sent up the FUT could be returned to the output coupler to interact with the reference arm signal. Accordingly they used a 3dB coupler to split the signal from the laser into the two arms of the interferometer. For that application this ratio would be close to an optimized Visibility (1.27). For many of my measurements though, I was needing greater than a 99/1 split ratio to maximize the Visibility (or anywhere from that down to 50/50 depending on the FUT). Accordingly the tunable coupler was used instead. Besides this optimization in visibility it also allows for a larger fraction of the light to travel up to the FUT. When Rayleigh backscatter is used as the primary sensing mechanism the higher the intensity incident light (at least within the linear regime), the greater the backscatter the signal measured by the detector and the better the SNR.

As well, they used a 3dB (50/50) coupler to couple the light from the interferometer to the FUT. The problem with this is that upon exiting the FUT, half of the light travels out the wrong output back towards the laser and is not measured by the detectors. I used a 3-port

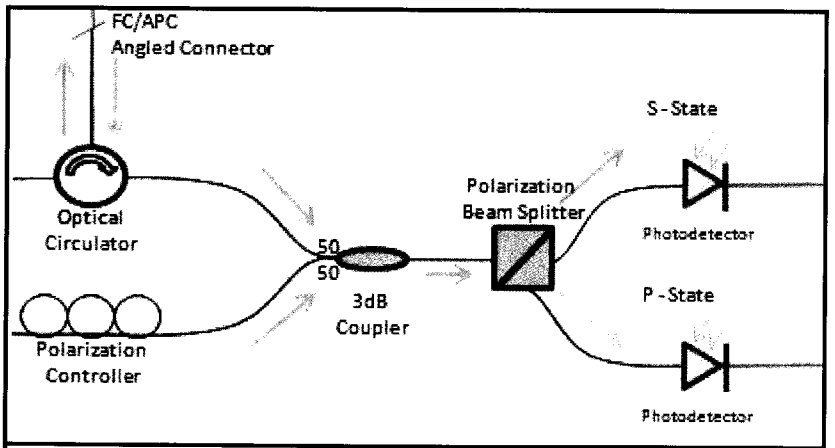

Fig.2.10 – Polarization Diverse OFDR measurement setup.

optical circulator instead so that all of the back-reflected light (minus insertion losses) travels to the detectors. The polarization diverse measurement scheme of my setup can be seen in Fig.2.10. As was the case with the previous basic setup the PD version still has the two arms of the interferometer at a 50/50 2x1 coupler – so that that location the signal can still be described by Eq.2.6. The combined signal then passes through a polarization beam splitter such that the signal gets separated into its two separate projections of the orthogonal S & P-states which are then measured at the respective FPD510 photodetectors. To extend upon Eq.2.6, the signals measured at the two detectors can be treated as:

$$I_{S\,AC} = 2\rho(\omega)[(T_S E_{MEAS})\cdot(T_S E_{REF})]\cos[\phi(\omega)+\omega(t)\Delta\tau], \tag{2.7}$$

$$I_{P\,AC} = 2\rho(\omega)[(T_P E_{MEAS})\cdot(T_P E_{REF})]\cos[\phi(\omega)+\omega(t)\Delta\tau], \tag{2.8}$$

where T_S and T_P represent the projection operators for the orthogonal S and P states respectively while E_{MEAS} and E_{REF} represent the electric fields propagating down the measurement arm and reference arm.

One of the main purposes of using the PD setup over the basic setup is that the initial field leaves the laser it is normally linearly polarized. As it passes through the initial measurement interferometer, if the polarization controller was not in the reference arm the light would remain predominantly in its original polarization state. On the other hand, the light travelling along the measurement arm when exposed to the FUT (especially if it is a type of specialty fiber) could in theory make the exiting light an orthogonal polarization state to what it was to when it entered. Thus, when the two arms of the interferometer recombine since the two signals would be predominantly orthogonal to one another then there would be very little resulting beating from the interaction of the two fields – which is what is needed to provide both the location information of the events as well wavelength shift information. So

just to be on the safe side, the light in the reference arm is passed through a polarization controller so that it becomes roughly 50/50 for the S and P states. Then no matter what type of FUT is used, and what the polarization state is that emerges from the measurement arm, there will be at least some interaction (and accordingly beating) with the light from the reference arm.

2.5.3 Balanced OFDR Measurement Scheme

Although balanced detection schemes are commonly used in OCT research[21,22], from what I could find - no research has been published using balanced detection within an OFDR configuration. The balanced amplified photodetector used for this setup was a Thorlabs PDB150-AC which has variable gain/bandwidth. A block diagram of this detector can be seen in Fig.2.11. Two very well-matched photodiodes are connected in series. Their difference is then amplified through a low noise, high-speed transimpedance amplifier (TIA) that generates an output voltage proportional to the difference between the photocurrents. If the two optical inputs originate

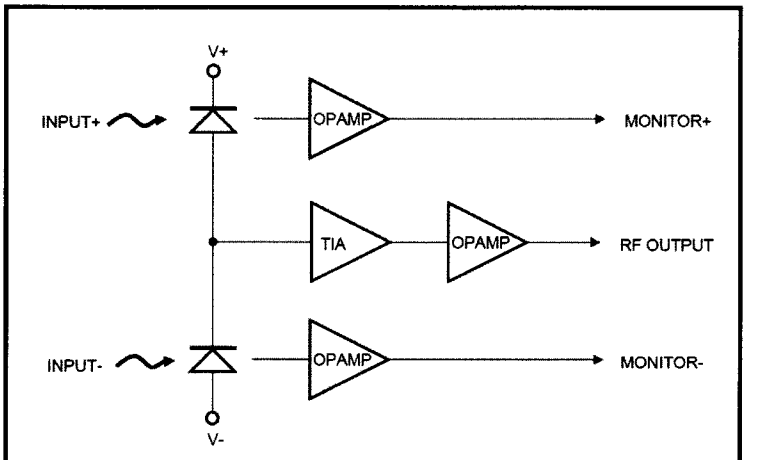

Fig.2.11 – Functional block diagram of the PDB150-AC balanced detector.[23]

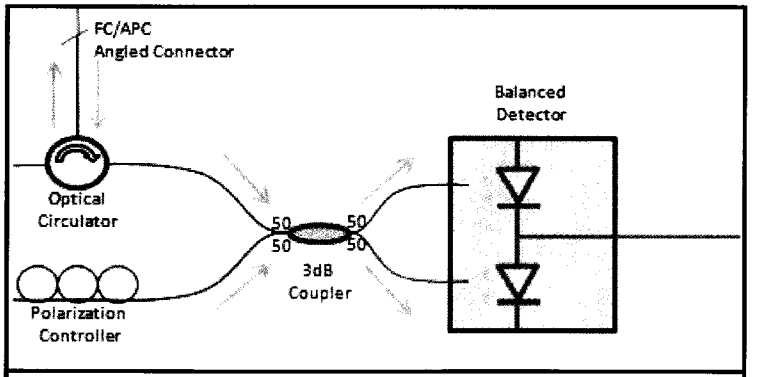

Fig.2.12 – Balanced OFDR measurement scheme.

from the same source and their intensities are closely matched then the difference between the photocurrents results in the cancellation of common mode noise. This allows to detect smaller changes on the signal path to be extracted from the interfering noise floor.

The balanced OFDR setup used can be seen in Fig.2.12. The signals from the two arms recombine in a very well balanced 50/50 2x2 coupler. The outputs of the coupler then enter into the detector. For ideal 2x2 50/50 couplers, the matrix scattering coefficients have a magnitude of $1/\sqrt{2}$, allowing the power to be split equally between the two outputs. The Maxwell equation solutions for such a coupler require that the scattering matrix coefficients have phases such that:

$$A = \frac{1}{\sqrt{2}}\begin{bmatrix} e^{-i0} & e^{-i\pi/2} \\ e^{-i\pi/2} & e^{-i0} \end{bmatrix}, \tag{2.9}$$

in order to preserve the conservation of energy. Accordingly the two outputs from the 2x2 would be of the following form:

$$I_{1AC} = \sqrt{2} I_0 \rho(\omega) \cos[\phi(\omega) + \omega(t)\Delta\tau], \tag{2.10}$$

$$I_{2AC} = \sqrt{2} I_0 \rho(\omega) \cos[\phi(\omega) + \omega(t)\Delta\tau] e^{-i\pi/2}. \tag{2.11}$$

If g represents the gain factor applied by the balanced detector then the output sign from it is of the following form:

$$\begin{aligned} I_{Diff} &= I_{1AC} - I_{2AC} \\ &= \sqrt{2} I_0 g \rho(\omega) \cos[\phi(\omega) + \omega(t)\Delta\tau](1 - e^{-i\pi/2}) \end{aligned}. \tag{2.12}$$

2.5.4 Quadrature Interferometer OFDR Measurement Scheme

This version of the measurement scheme as well as the one in the next

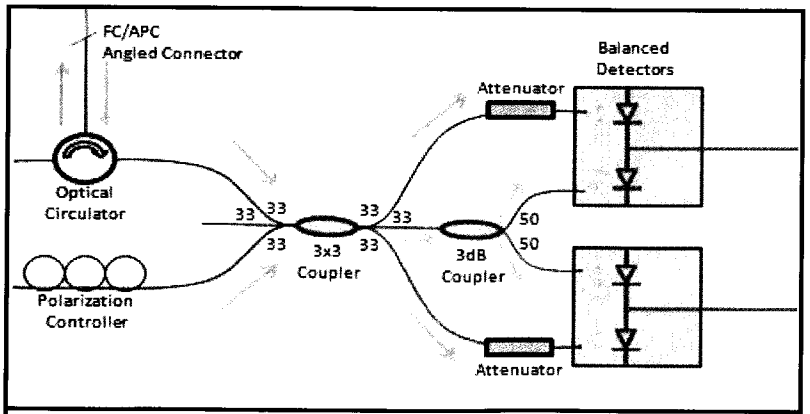

Fig.2.13 – Quadrature Interferometer OFDR Measurement Scheme.

subsection was inspired from the following references [25,26]. Although this detection method has been used in OCT experiments, it has not been incorporated into any OFDR setups. The diagram can be seen in Fig.2.13. For this setup the two arms of the measurement interferometer recombine in a 3x3 coupler. Each of the outputs are separated by a phase of $2\pi/3$. Thus, since all the outputs are supposed to be of ideally equal intensity, if measured at the outputs the signals would be of the form:

$$I_{1AC} = \frac{2}{\sqrt{3}} I_0 \rho(\omega) \cos[\phi(\omega) + \omega(t)\Delta\tau], \tag{2.13}$$

$$I_{2AC} = \frac{2}{\sqrt{3}} I_0 \rho(\omega) \cos[\phi(\omega) + \omega(t)\Delta\tau] e^{-i2\pi/3}, \tag{2.14}$$

$$I_{3AC} = \frac{2}{\sqrt{3}} I_0 \rho(\omega) \cos[\phi(\omega) + \omega(t)\Delta\tau] e^{-i4\pi/3}. \tag{2.15}$$

From here, one of the outputs then passes through a 1x2 50/50 coupler (say 2.14), and the other two outputs (2.13 & 2.15) are attenuated down to the same amplitude as those emerging from the 1x2 coupler. In the end we have 4 equations of the following form:

$$I_{1AC} = \sqrt{\frac{2}{3}} I_0 \rho(\omega) \cos[\phi(\omega) + \omega(t)\Delta\tau], \tag{2.16}$$

$$I_{2aAC} = \sqrt{\frac{2}{3}} I_0 \rho(\omega) \cos[\phi(\omega) + \omega(t)\Delta\tau] e^{-i2\pi/3}, \tag{2.17}$$

$$I_{2bAC} = \sqrt{\frac{2}{3}} I_0 \rho(\omega) \cos[\phi(\omega) + \omega(t)\Delta\tau] e^{-i7\pi/6}, \tag{2.18}$$

$$I_{3AC} = \sqrt{\frac{2}{3}} I_0 \rho(\omega) \cos[\phi(\omega) + \omega(t)\Delta\tau] e^{-i4\pi/3}. \tag{2.19}$$

Equations (2.16 & 2.19) represent the two outputs from the 3x3 coupler which run through the manual attenuators; (2.17 & 2.18) are the two outputs which emerge from the 1x2 50/50

coupler. Initially, (2.13) and (2.17) were connected into one of the balanced detectors, while (2.15) and (2.18) ran into the other one. As you can see the two inputs of each detector had a significant intensity difference which resulted in a large DC offset. To balance these, the one arm was attenuated while: a) monitoring the two inputs through the balanced detector, as well as b) observed the combined signal on an oscilloscope. As the value of one input approached the other the DC portion of the signal also disappeared such that only the AC remained. This balancing process on both detectors also removed 1/3 of the optical power. The gain on both detectors was set the same so that the outputs on each detector is as follows:

$$\Delta I_{1AC} = \sqrt{\frac{2}{3}} I_0 g\rho(\omega)\cos[\phi(\omega)+\omega(t)\Delta\tau](e^{i0} - e^{-i2\pi/3}), \tag{2.20}$$

$$\Delta I_{2AC} = \sqrt{\frac{2}{3}} I_0 g\rho(\omega)\cos[\phi(\omega)+\omega(t)\Delta\tau](e^{-i7\pi/6} - e^{-i4\pi/3}). \tag{2.21}$$

In other words, one of the balanced detectors has a phase difference of 120° between its inputs while the other detector has a phase difference of 30°.

For this version of the setup the two signals are acquired on different channels and like the polarization diverse version of the setup the vector sum is taken.

2.5.5 Differential Quadrature Interferometer OFDR Measurement Scheme

This version of the scheme can be seen in Fig.2.14 below:

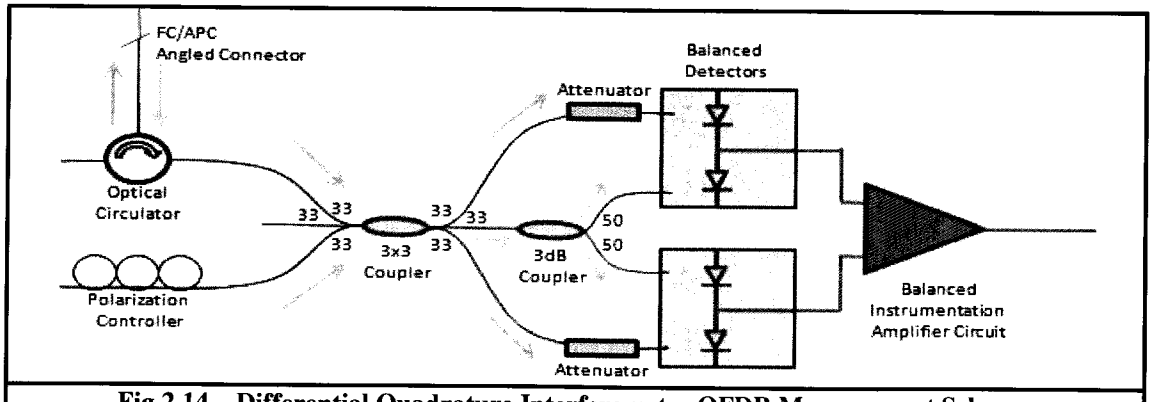

Fig.2.14 – Differential Quadrature Interferometer OFDR Measurement Scheme.

The layout is exactly the same as that described in §§2.5.4 with the exception that the outputs from the two balanced detectors are now passing through a balanced instrumentation amplifier circuit that I designed. The details of this circuit can be found in the following diagram:

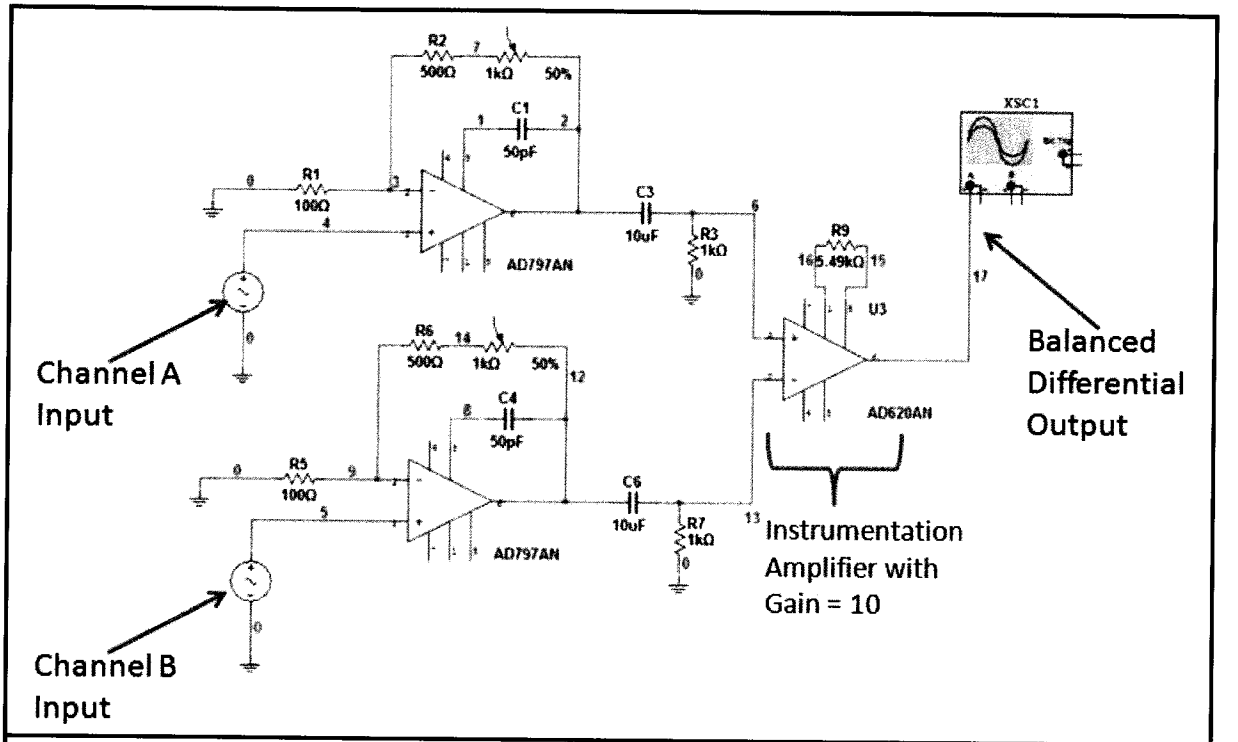

Fig.2.15 – Balanced Instrumentation Amplifier Circuit

The outputs from the balanced photodetectors enter into the inputs as seen above. The op-amp arrangements they first pass through have gains that are tunable from about 5 to 15. These are mainly only used for fine tuning of the amplitudes of the two channels so that they're properly matched up. They then pass through 16Hz high-pass filters to remove the DC offset which was introduced by the op-amps. Accordingly when measuring the signals at point 6 and 13 on the diagram and properly adjusted, the two signals are both AC and have exactly the same amplitudes. These two balanced signals then enter into an AD620 amplifier that takes the difference between the two inputs and applies a further gain factor of 10. This

gain factor is initially (and equally) applied to each channel before taking the difference. The details of the AD620 instrumentation amplifier can be seen in Fig.2.16.

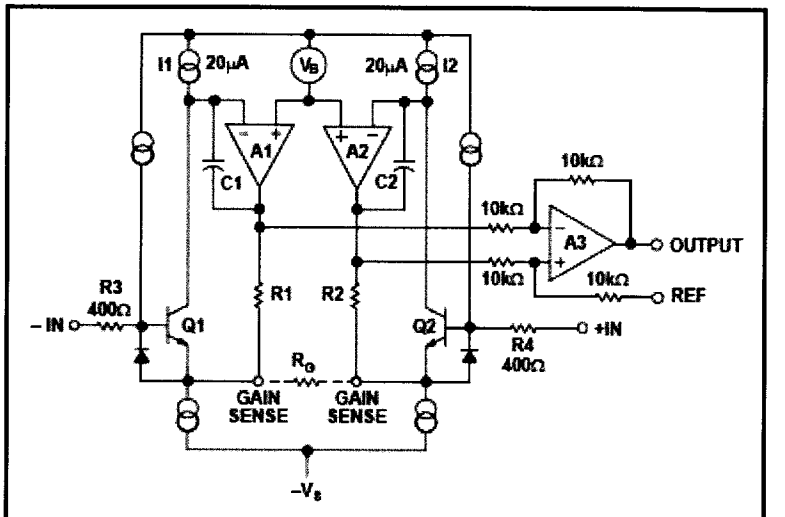

Fig.2.16 – Simplified Schematic of the AD620 Instrument Amp.[27]

As was mentioned in the last subsection, the net phase coming from the first balanced photodetector is 120° while the other net phase difference of the other balanced photodetector is 30°. Based on such, after these two signals pass through the balanced instrumentation amplifier circuit the final phase difference is 90°. This is the same net phase difference as the balanced OFDR measurement scheme as was discussed in §§2.5.3.

2.6 Signal-to-Noise Ratio Comparisons Between the 5 OFDR Configurations

The purpose of this section is to compare the overall performance, dynamic range, and SNR ratios between specific Fresnel reflectors and neighboring Rayleigh backscattering levels given in the attenuation profile distributions of a typical FUT. On the following page are the signals measured at the detector(s) for the 5 different configurations over a 40nm sweeping range (1470-1510nm) at a rate of 20nm/s using the Agilent laser set to 25mw output power and linewidth of 100 kHz. The same FUT was used for all – the specifics of which can be found in the *strain* section of chapter 4. Based on the gating circuitry described

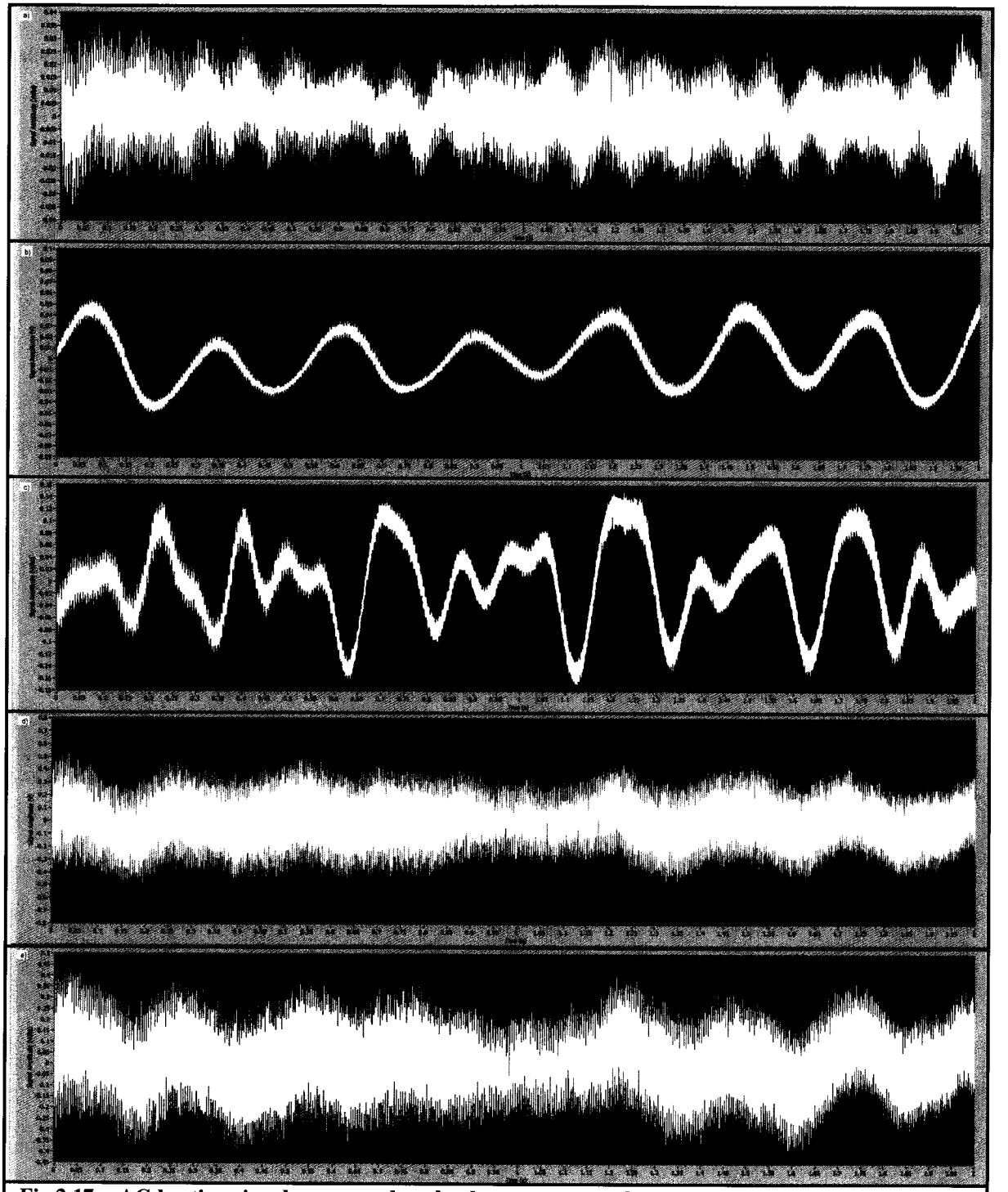

Fig.2.17 – AC beating signals measured at the detectors over a 2s sweep, 40nm range (1470-1510nm) at 20nm/s for the following respective OFDR configurations: a) Basic OFDR Setup, b) Polarization Diverse OFDR Setup, c) Balanced OFDR Setup, d) Quadrature Interferometer OFDR Setup, and e) Differential Quadrature Interferometer OFDR Setup.

in the previous sections, the above data is the convolution of the continuous electric field distribution from (-∞,∞) in the time domain with an impulse function that has a width which is the duration of the sweep. Taking the Fourier transform of this data retrieves the beating distribution (attenuation function) of the FUT with respect to the reference arm. For the results that will be presented as follows, the variable coupler was set such that the measurement arm of the interferometer had 99.5% of the light travelling along it, while only 0.5% going to the reference arm. Since the output power from the laser was 25mW (14dBm) this split ratio corresponded to 13.9578 dBm, and -0.903 dBm powers to the measurement and reference arms respectively. The backscattered light that travelled along the measurement arm had an attenuation of approximately 40dB compared to the injected light (taking into account insertion losses from the couplers and circulator, splice losses, etc..), while the reference arm's flight path only experienced a loss of 0.5 dB from the coupler insertion losses and splices. Thus the final intensities of these two signals when recombining are -26.04dBm and -1.403dBm for the measurement and reference arm respectively. Once combined this means the DC portion of the signal is I_{DC}=*-1.418 dBm* and the AC portion, I_{AC}=*-24.515 dBm*. Being that the detectors/DAQ-cards are AC-coupled then when looking at the beating distribution of the data we need to normalize the data by a shift that is the difference between I_{AC} and I_{DC} or 23.097 dB. All the data shown in the following subsections shall take this normalization factor into account.

As well, assuming that the sweep is linear then the beating frequency and position along the FUT are proportional by the following scaling factor:

$$F_{BEAT} = \left(2n_g \frac{\partial\lambda/\partial t}{\lambda_{INIT}\lambda_{FINAL}} \right) \cdot x . \tag{2.22}$$

When sweeping at a rate of 20nm/s through the range of 1470nm to 1510nm this translates into an average beating frequency of 26457.63 Hz/m along the FUT and is reflected in the second x-axis in the following figures. As well, these graphs have also taken into account the gain from the photodetectors which is 40V/mW for the FPD510 detectors, and 1kV/mW for the balanced detectors. This results in a shift down by 16.02dB, 17.53dB, 30dB, 31.51dB, and 30dB for setups 1 to 5 respectively. In the figures below there will be 5 main points of interest that I will look at: A) the backscatter peak of a point on the end of the FUT which is would tightly to attenuate the signal, B) the Rayleigh backscatter level prior to this peak, C) the Rayleigh backscatter level after the peak, D) the photodetector dark state noise level (ie – background noise level from detector when no optical signal is detected), and E) is the average noise level seen past D. The SNR will be measured for this peak for comparison purposes between the setups which is equal to: $SNR = |D - A| - |D - E|$. The contrast level between the two Rayleigh backscatter levels around the event is also observed which is $|C - B|$, as well as the dynamic range which is $|D|$.

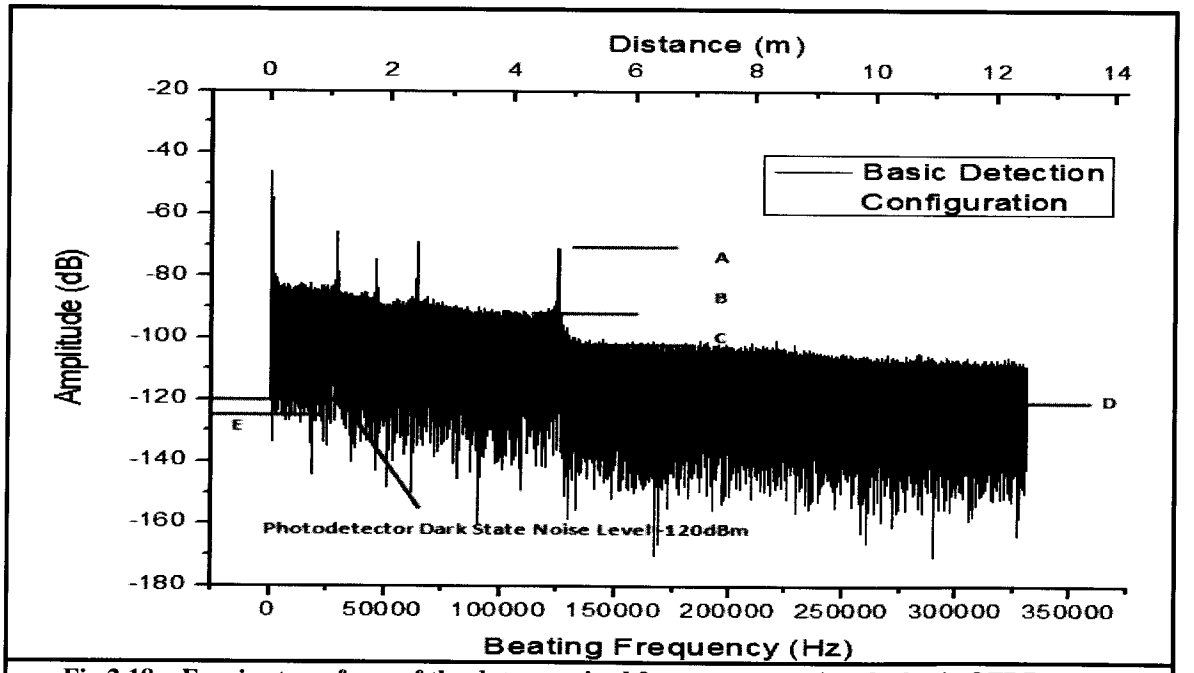

Fig.2.18 – Fourier transform of the data acquired from a sweep using the basic OFDR setup.

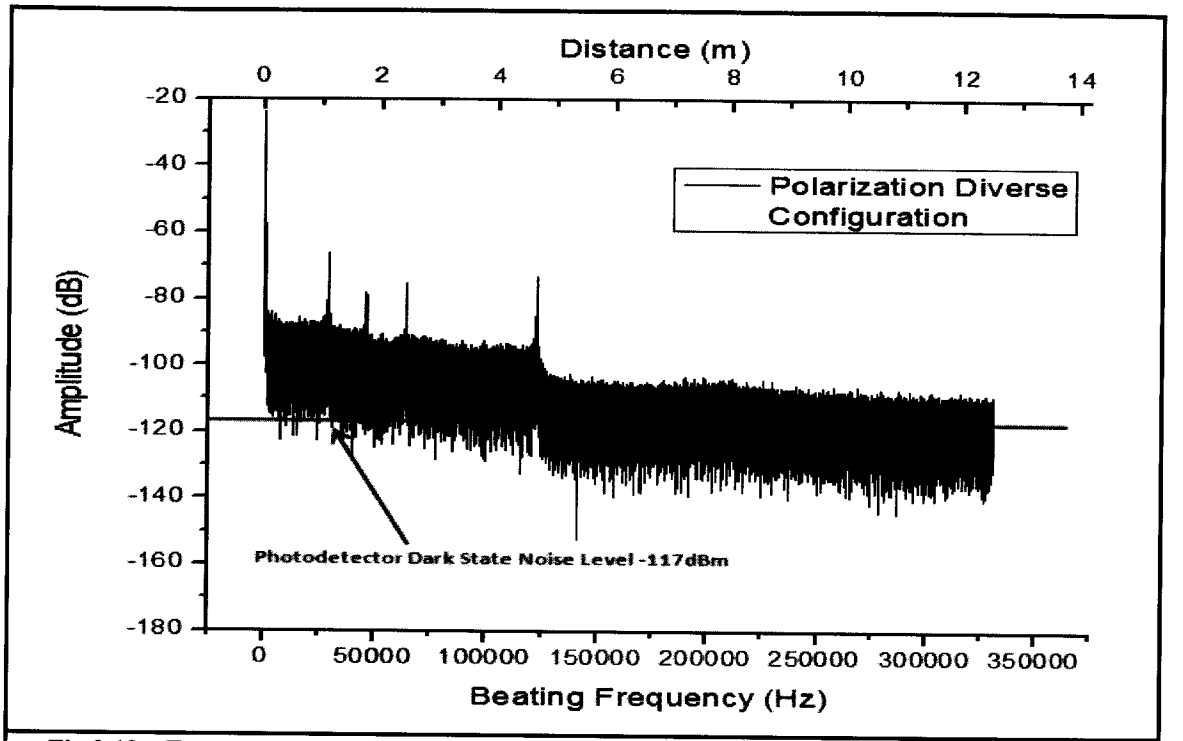

Fig.2.19 – Fourier transform of the data acquired using the polarization diverse OFDR setup.

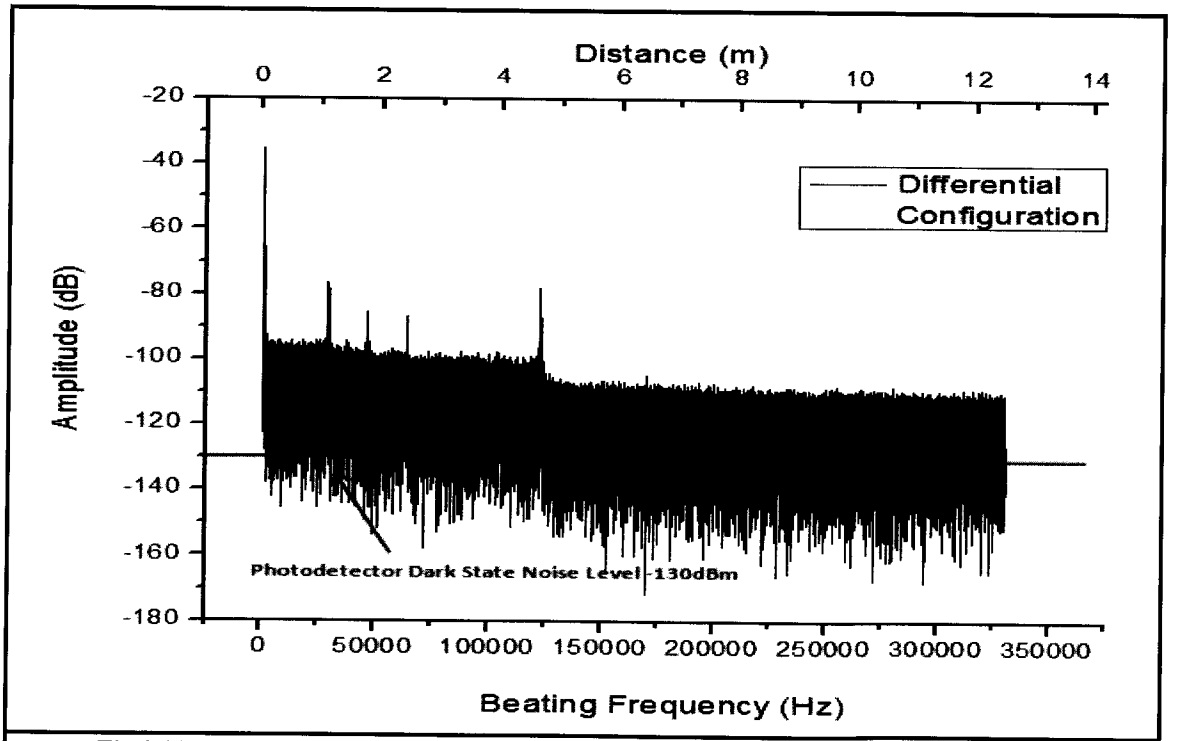

Fig.2.20 – Fourier transform of the data acquired using the differential OFDR setup.

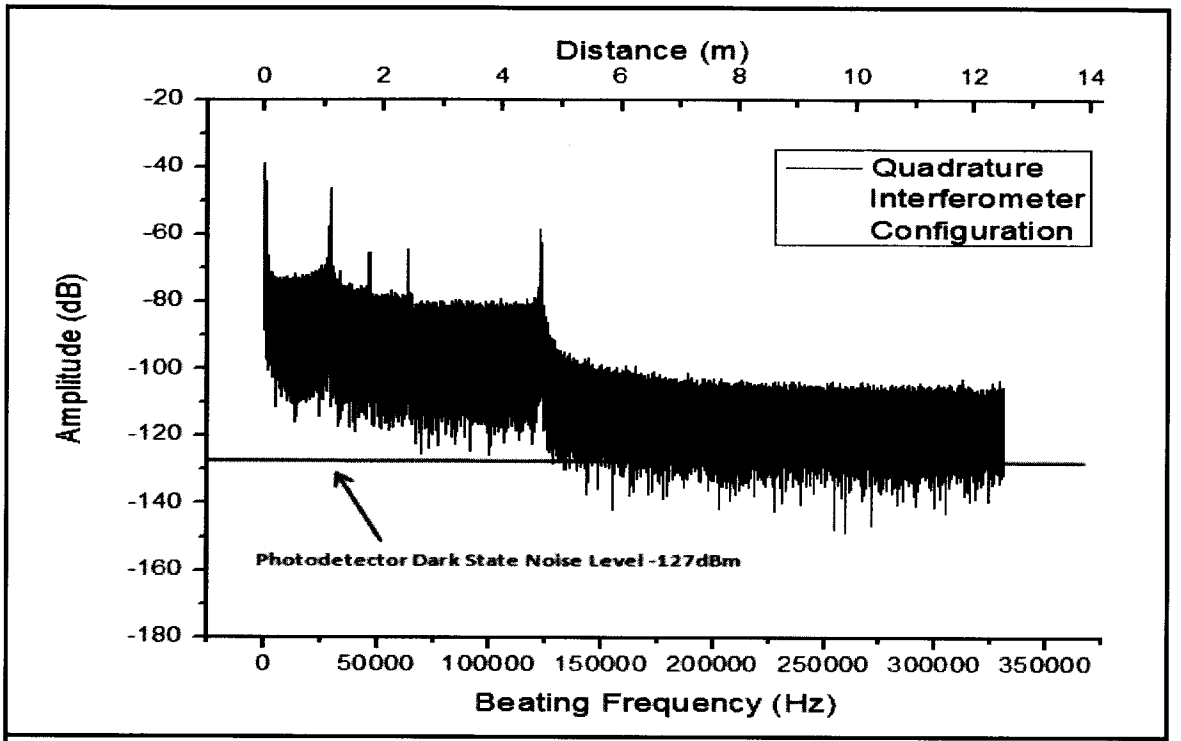

Fig.2.21 – Fourier transform of the data acquired using the quadrature interferometer OFDR setup.

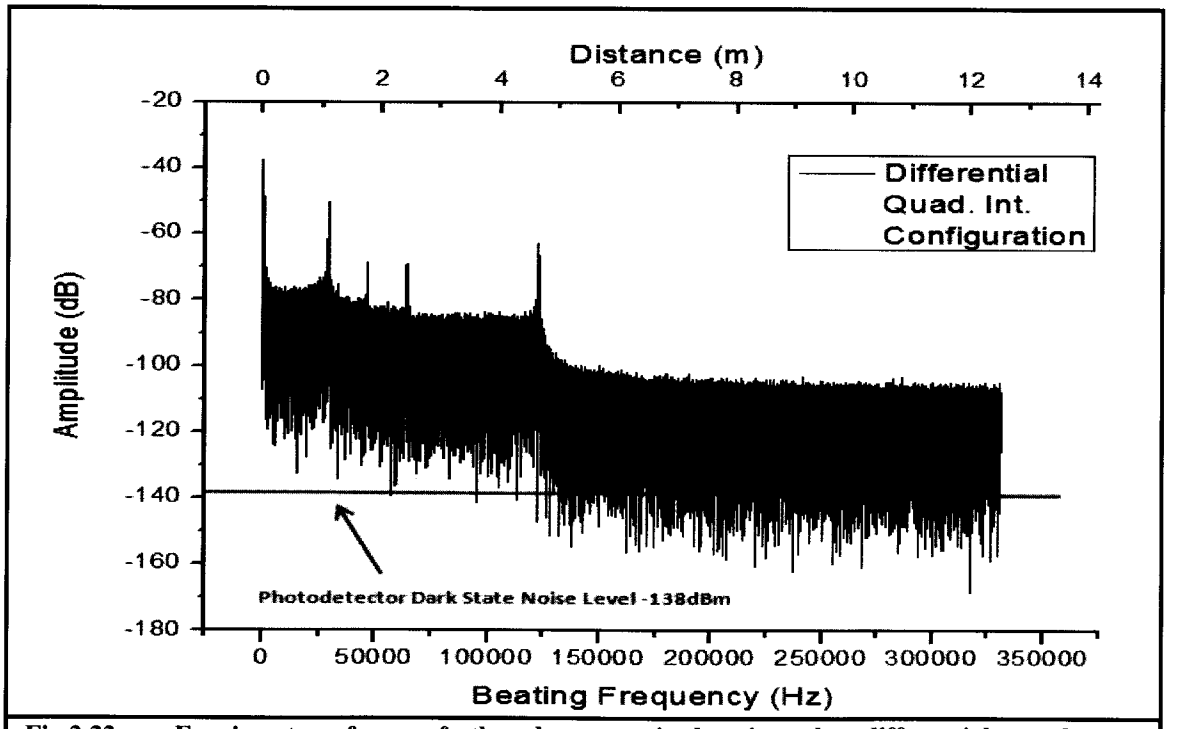

Fig.2.22 – Fourier transform of the data acquired using the differential quadrature interferometer OFDR setup.

Table 2.5 – Overall Performance of the 5 OFDR Configurations (±0.2 dB uncertainty A – E)								
Setup Configuration	**A (dB)**	**B (dB)**	**C (dB)**	**D (dB)**	**E (dB)**	**SNR |D - A| - |D - E|**	**Rayleigh Scattering Contrast |C – B|**	**Sensitivity (D – max det. Power)**
Basic	-71	-92.5	-102	-120	-125	44	9.5	130
Pol. Div.	-73	-94	-104	-117	-120.5	41.5	10	127
Differential	-78	-100	-108	-130	-135	47	8	140
Quad. Int.	-57	-80	-103	-127	-130	67	23	137
Diff. Quad. Int.	-63	-84	-103	-138	-141.5	71.5	19	148

From the above Table 2.5 you can seen that with respect to SNR and Sensitivity it is the differential quadrature interferometer setup that performed the best, while for Rayleigh scattering contrast – the quadrature interferometer scored the best. The polarization diverse setup scored the poorest in these parameters because the Fourier transformed data is only showing the x-polarized, y-polarized, and circularly polarized light components in the higher beating frequency distribution. The randomly polarized portions as well as the elliptically polarized light signals are averaged out (DC) to very slow frequency variation. So even though the transforms were AC-coupled you still see that the overall Rayleigh scattering thickness of the PD results shown in Fig.2.19 is about 9dB thinner than the scattering thickness shown in Fig.2.18. Yet when you look at the frequency components close to the 0 mark, the PD setup is 22dB greater than that of the basic setup. This is evident when you look at Fig.2.17(b) where you can see the low frequency cyclic repetitions of the two polarization states. One of the advantages the PD setup does have over the others is that it can differentiate where (or if) there are polarization dependent losses (PDL's) in the fiber under test.

Chapter 3

Data Analysis Algorithms

The previous two chapters outlined the basic theory of OFDR's, provided details of the various setups used in my research, and compared the results they provided in the time domain for the same FUT. For the better part of 30 years, this has been the primary usage of the OFDR setups – to analyze and characterize networks and optical waveguides[11 - 13, 19, 20, 28]. Since about 1998, the OFDR setups have also been used not only to characterize an FUT, but also to use that fiber as distributed temperature sensor, stress/strain sensor or both[29 - 35]. The purpose of this chapter is the go through the details of this analysis in how to retrieve the wavelength shift information which is proportional temperature changes and/or stress/strain changes at specific locations.

3.1 Classical Analysis and its Hereditary Shortcomings

When using any of the setups which were discussed in chapter 2 along with the auxiliary interferometer the spatial resolution of the measurement Δz, in the time domain is determined by the spectral bandwidth of the scanning range by the following equation:

$$\Delta z \cong \frac{c}{2n_g \Delta \upsilon} \cong \frac{\lambda_{INIT}\lambda_{FINAL}}{2n_g \Delta\lambda}, \tag{3.1}$$

where $\Delta\lambda$ is the wavelength range of the sweep, λ_{INIT} is the starting wavelength, and λ_{FINAL} is the stopping wavelength. Also, as a variant of Eq.2.1 we know that the clocking rate (and in turn the data sampling rate) from the external clock is:

$$\upsilon_{CLOCK} = n_g L \frac{(\Delta\lambda/\Delta t)}{\lambda_{INIT}\lambda_{FINAL}}, \tag{3.2}$$

where L is the length of the delay line in the auxiliary interferometer and $\Delta\lambda/\Delta t$ is the average sweeping rate of the laser. The total sweep duration, T_s can be viewed as the sweeping range divided by the sweeping rate: $T_s = \Delta\lambda/(\Delta\lambda/\Delta t)$. Thus the total number of data samples acquired is:

$$\begin{aligned} S_{TOTAL} &= \upsilon_{CLOCK} * T_S = n_g L \frac{(\Delta\lambda/\Delta t)}{\lambda_{INIT}\lambda_{FINAL}} * \frac{\Delta\lambda}{(\Delta\lambda/\Delta t)} \\ &= n_g L \frac{\Delta\lambda}{\lambda_{INIT}\lambda_{FINAL}} \end{aligned} . \tag{3.3}$$

When taking the FFT of this data, because of the Nyquist frequency requirement, the number of samples drops by a factor of 2:

$$S_{FFT} = \frac{n_g L}{2} \frac{\Delta\lambda}{\lambda_{INIT}\lambda_{FINAL}}, \tag{3.4}$$

but since $L = 4*L_{FUT}$, where L_{FUT} is the maximum length of the FUT we have:

$$S_{FFT} = 2n_g L_{FUT} \frac{\Delta\lambda}{\lambda_{INIT}\lambda_{FINAL}}. \tag{3.5}$$

The number of points/m is simply S_{FFT}/L_{FUT} or:

$$S_{P/m} = S_{FFT} / L_{FUT} = 2n_g \frac{\Delta\lambda}{\lambda_{INIT}\lambda_{FINAL}}. \tag{3.6}$$

Based on such, the inverse of (3.6) is of course the spatial resolution which is given in (3.1). Now suppose I want to isolate a specific segment of size Δx. Then the total number of points in that section is:

$$S_{\Delta x} = S_{P/m} * \Delta x = 2n_g \frac{\Delta\lambda}{\lambda_{INIT}\lambda_{FINAL}} \Delta x. \tag{3.7}$$

When performing the FFT^{-1} on this segment to return to the spectral domain the number of

points remains the same as in (3.7) but now they are spread across the original scanning range $\Delta\lambda$. Thus the spectral resolution (pts/nm) can be viewed as follows:

$$R_\lambda = S_{\Delta x} / \Delta\lambda = \frac{2n_g \Delta x}{\lambda_{INIT}\lambda_{FINAL}} * 10^{-9} \ . \tag{3.8}$$

When using a segment size Δx of 1cm, an initial wavelength of 1470nm, and a final wavelength of 1510nm we get from (3.8) a spectral resolution of 13.22 points/nm or 75.6 pm/point. Now if we want to keep the segment size the same, varying the sweeping range does very little to improve the overall resolution. If doing temperature measurements using SMF-28 fiber this 75.6pm spectral resolution corresponds with a temperature resolution of 8.3°C. A larger sweeping range will add more points to the segment size in the time domain and thus improve the *spatial resolution*. When transformed back to the spectral domain though, and compared with the same segment's data at an earlier time using a cross-correlation to measure the wavelength shift - the larger array will make the results more *accurate*, and provide a larger spectral range to allow for a larger dynamic range of the sensor, but it *can't* improve the overall *spectral resolution*. So classically speaking, if wanting a sensor/segment size of 1cm, the spectral resolution of 75.6 pm/point is etched in stone. Based on this classical analysis then it is always a trade-off. If you increase the segment size you can improve your spectral resolution but you have decreased your distributed sensor spatial resolution in the process. So one can have a 1cm segment with 8°C temperature resolution, or an 8cm segment with 1°C temperature resolution, but classically speaking it is not possible to have a 1cm segment with 1°C temperature resolution.

In the following sections what I shall cover are novel data analysis algorithms which try to maintain similar accuracies as the classical version, while also trying to improve the spectral resolution (and in turn sensing resolution) as well as the overall SNR of the sensor

data without having to increase the segment size – only at a compromise of possibly the sensor's dynamic range.

3.2 Basic Process for Detecting Wavelength Shift at Specific Locations

The following process is the basic/classical method used for extracting the scatter pattern profiles for specific fiber segments Δx, and retrieving their respective spectral responses. Taking these spectral responses at different times when the section received some external stimulus and comparing them provides the relative wavelength shift which is proportional to the applied temperature, stress/strain or both.

At some initial time when no stimulus is being applied to the FUT:

Step 1: Sweep the tunable laser of any of the configurations described in Chapter 2 to acquire the complex data set of the FUT with respect to the reference arm.

Step 2: Take the power spectrum of the data set X which is equal to:

$$P_{spect} = \frac{\left|FFT\{X\}\right|^2}{n^2}, \tag{3.9}$$

where n is the number of points in the data set. If the Polarization Diverse or Quadrature Interferometer configurations are being used which have 2 data channels then take the combined vector sum power spectrum as follows:

$$P_{spect} = \frac{\sqrt{\left|FFT\{X\}\right|^2 + \left|FFT\{Y\}\right|^2}}{n^2}. \tag{3.10}$$

Step 3: Using (2.22) convert the x-axis of this power spectrum from beating frequency into position along the FUT. Upon inspecting this data decide where in the array is your 'region of interest' along the FUT - say from the 2m to 8m region out of a 12.5m FUT.

Now with this array element range in mind, take the corresponding subsets from FFT{X} (and FFT{Y} if using 2-Channel configurations). Unlike the power spectrum data sets which are real, the FFT{X} data sets are actually complex so contain the phase information which is needed to retrieve the wavelength shift information.

Step 4: At a later time after a stimulus (heat, pressure, bending, twisting, longitudinal stress, etc...) has been applied to the fiber – repeat steps 1 to 3. Again saving the subset in memory that pertains to the same 'region of interest' of length m.

Step 5: Decide on a segment size Δx which corresponds to a sensor.

Save this array subset in memory.

Step 6: Using (3.7) find out the number of points in the array n which are associated with that segment size.

Step 7: For both (or 4 if using the 2 channel configurations) of the 1-D array subsets acquired at the end of step 3 and step 5 (of element range 0 to m-1), reshape them to a 2-D array of width n and length m. Each row represents a subsequent sensor such that the total number of sensors in the 'region of interest' is equal to m/n and of size n.

Step 8: Perform the inverse Fourier transform $FFT^{-1}\{\Delta x\}$ on each row for all of the 2-D arrays so that each 'sensor element' is back in the spectral domain.

Step 9: For each frequency domain segment calculate the amplitude (magnitude) of the complex numbers at each point in each row. If using the 2 channel configurations then carry out the vector sum of the two amplitude arrays at time t_0 and the two amplitude arrays at the later time t.

Step 10: For each of the 2 amplitude arrays coming out of step 9, calculate the mean value for each row. Subtract the mean value found for each row from each point in the row.

Step 11: To determine the amount of spectral shift for each sensor, carry out the cross-correlations between each corresponding row of the 2 arrays. Thus the cross-correlation is being carried out for the first and second spectral responses for the same location. Where the cross-correlation is:

$$R_{xy}(\omega) = x(\omega) \otimes y(\omega) = \int_{-\infty}^{\infty} x^{*}(\tau) \cdot y(\omega+\tau) d\tau \ , \tag{3.11}$$

or:

$$R_{xy_i} = H_{i-(N-1)} \ , \tag{3.12}$$

where

$$H_j = \sum_{k=0}^{N-1} x^{*}_k \cdot y_{j+k} \ , \tag{3.13}$$

N is the segment size, and i = 0 to (2N – 2). In step 10 the mean is subtracted from the segment points before doing the cross-correlation because if not removed, when the cross-correlation is carried out a triangular shaped bias is added into the result which can be seen in Fig.3.1 below:

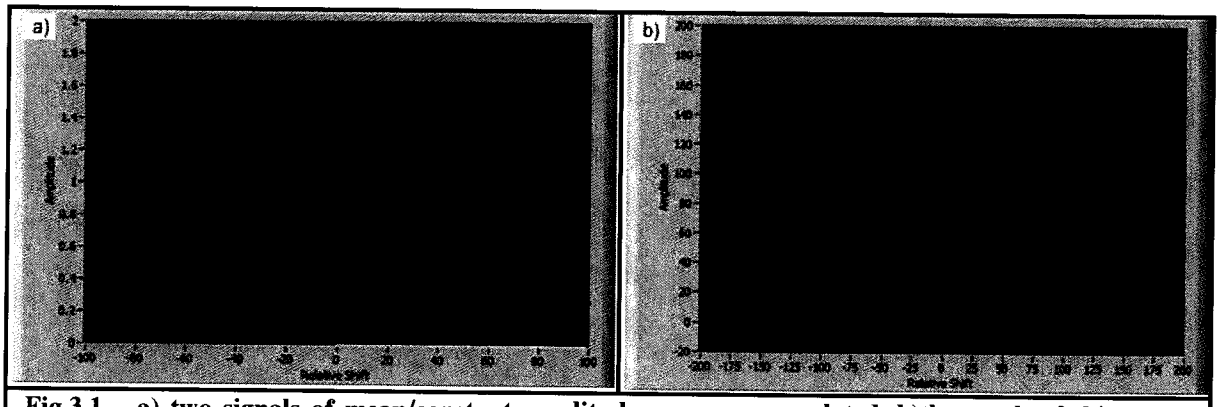

Fig.3.1 – a) two signals of mean/constant amplitude are cross-correlated, b)the result of this cross-correlation is a triangularly shaped bias.

This triangularly shaped bias does not provide any extra useful information and can actually introduce an error/distortion when trying to find the tallest peak in actual frequency shifted data - so is accordingly removed.

Step 12: One other important setup to this basic process which as far as I know has not been mentioned in other papers (at the time of this thesis write-up) is that once the mean was subtracted from each of the spectral responses and the cross-correlation was carried out – often the resulting correlation has a sinc shaped bias that comes out of the fact that the segment size which is being examined is finite, small and windowed. If the stimulus is uniformly distributed across the whole fiber segment Δx then this sinc bias is symmetric about the 0nm (center) point of the cross-correlation. If it is a non-uniform stimulus distribution then this sinc shaped bias begins to become asymmetric and distorted. Since this sinc bias (as was the case with the triangular shaped bias described in step 11) provides no additional information and at times can lead to an identification of the wrong (highest) peak of interest it is in turn removed from the cross-correlated data for the segment.

To remove this bias first a low-pass filter is applied to the data set to provide an averaged/smoothed out profile of the cross-correlation. The problem with most low-pass filters though (ie – Butterworth, Chebyshev, etc....) is that a phase shift occurs to the filtered data. This filtered data set when subtracted from the original in turn also lead to identification of the wrong peak of interest. To deal with this a zero phase shift low-pass filter is used. This step is illustrated in Fig.3.2 on the following page. Fig.3.2(a) illustrates a cross-correlation (with the mean subtracted first) of a section of fiber where a longitudinal strain is being applied (equivalent to 4.9N of force). As you can see this sinc function shaped bias is quite evident. If one wanted to find the peak of highest amplitude to identify the wavelength shift because of this bias the wrong peak would be taken. Fig.3.2(b) is the same data with a zero phase shifted filter applied to it which extracts the sinc shaped function with any other distortions resulting from non-uniform stimuli. Fig.3.2(c) is the function of

Fig.3.2(b) subtracted from (a). This now corrected cross-correlation properly identifies the highest peak which is also the peak of interest that reflects the amount of wavelength shifting that has occurred to that segment of fiber.

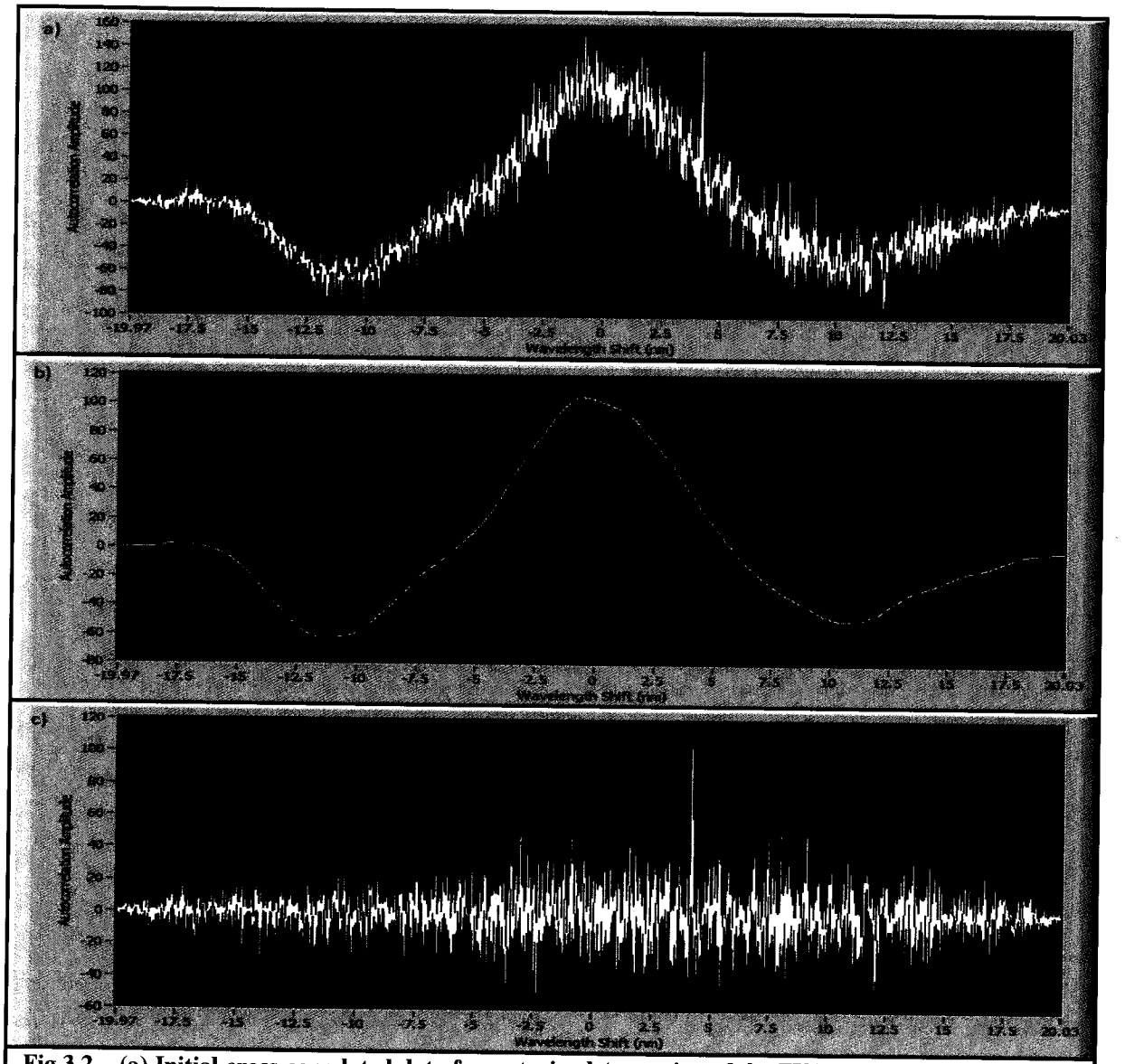

Fig.3.2 – (a) Initial cross-correlated data for a strained Δx section of the FUT, (b) this same data after passed through a zero phase shifting low-pass filter, (c) the corrected cross-correlated data by subtracting (b) from (a).

Step 13: The peak location of the resulting correlation is measured. If there was no wavelength shift then the peak remains in the center, if there was a shift then the location is

measured with respect to the center, divided by N and then multiplied by $\Delta\lambda$ to calculate the full wavelength shift for that sensor. This shift is then calibrated with respect to temperature, stress/strain, or any other stimuli. An example of this wavelength shift is given in Fig.3.3 below there the unheated sensor is shown in white, while when the same sensor is later heated is shown in red. The relative stimuli change is proportional to the difference in position of the two peaks.

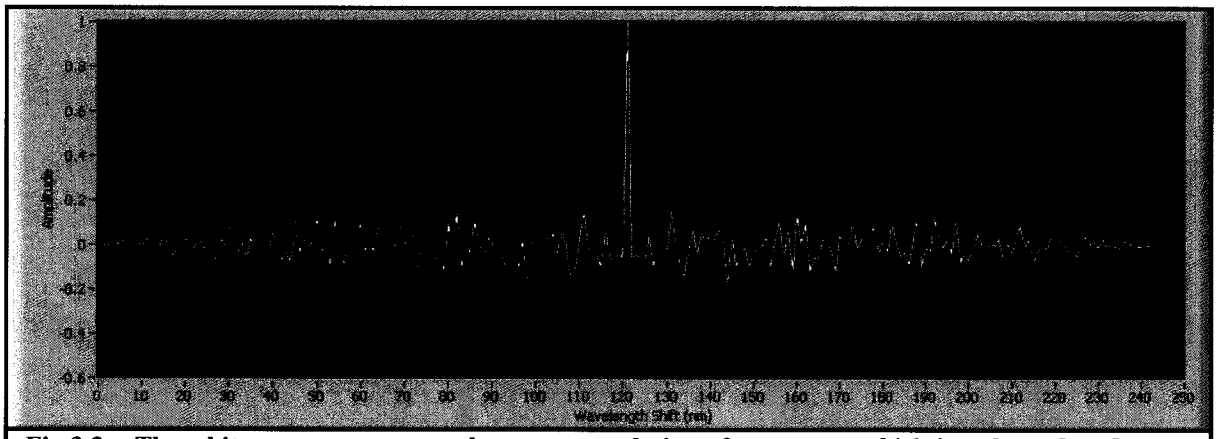

Fig.3.3 – The white curve represents the cross-correlation of a segment which is unheated, red curve represents the cross-correlation of that same segment when heated. The shift in position of the peaks is proportional to the wavelength shift, which in turn is proportional to the relative temperature change.

The following sections discuss how the algorithm that was described in this section was improved upon to try to increase the resolution so that it was higher than 75.6 pm/point, while also improving the SNR of the cross-correlations and in turn making the sensor readings more reliable.

3.3 Fourier Interpolation Algorithm (FIA)

The Fourier Interpolation Algorithm (FIA) was the first *extra* step of data analysis which built upon the classical process described in §3.2[36,37] to increase the resolution of the

spectral response for specific segments of the FUT without having to increase the segment size. The first step of FIA is to take the FFT of the signal data of size a. The output from this transform has the both the statistical positive frequency and negative frequency components whereby - since this is a complex data set, $-\upsilon = \upsilon^*$.

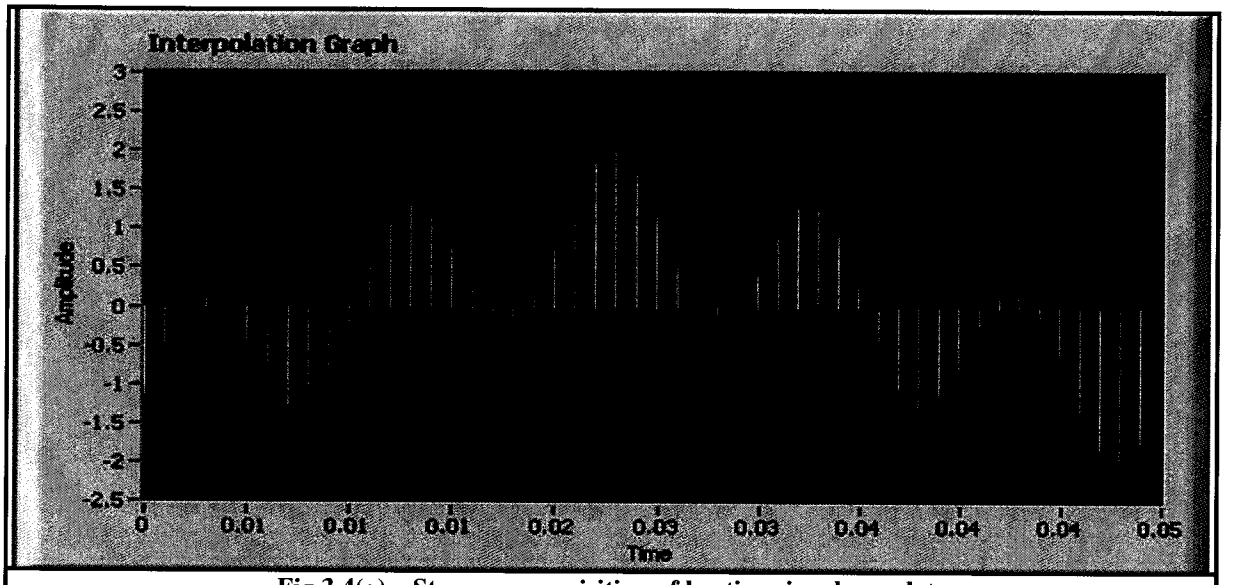

Fig.3.4(a) – Step one, acquisition of beating signal raw data

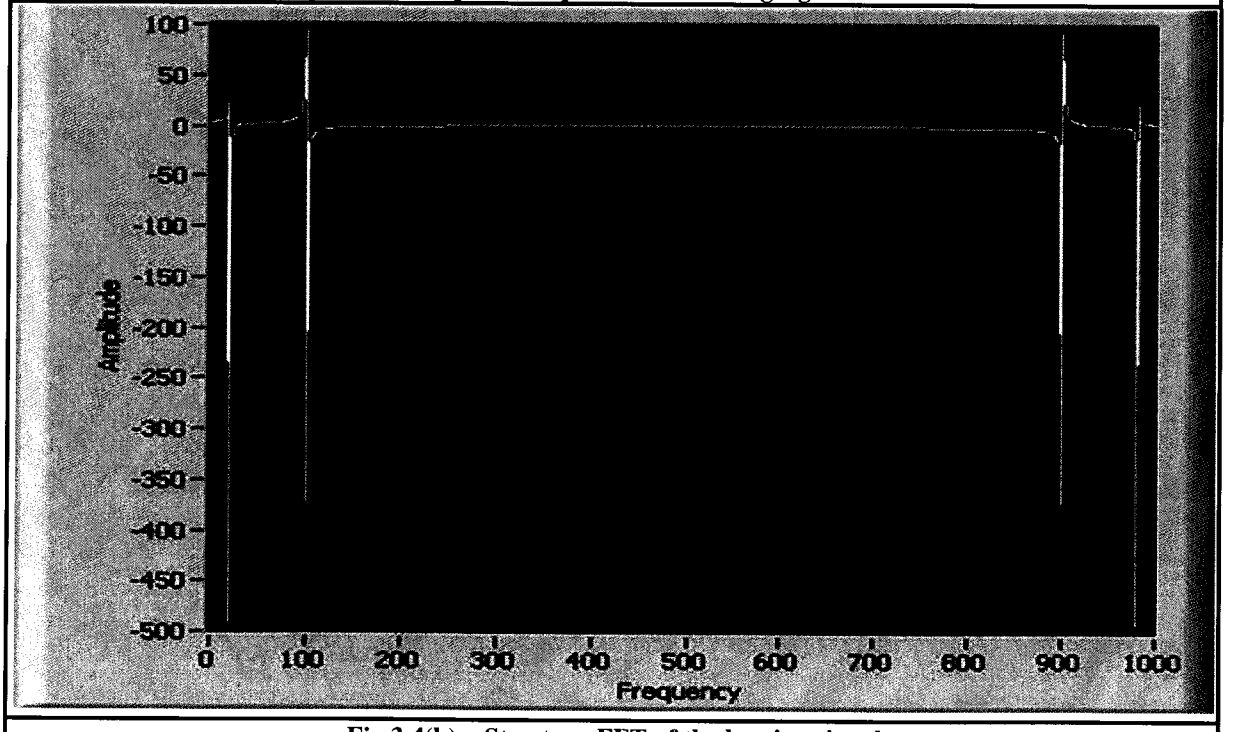

Fig.3.4(b) – Step two, FFT of the beating signal

Once an interpolation factor n has been chosen, then all of the FFT array elements are multiplied by this value, and at the array position $a/2$ (the position where the positive frequency elements end and the negative frequency components begin) a new subset is inserted into the array of size $(n - 1) \cdot a$ with values of $0 + 0i$. This actually increases the total number of points to the factor of n, while keeping the frequency components proportional to their original values and still normalized to the total number of elements of the array. This new data set is then inverse Fourier transformed (FFT^{-1}) back into the domain of the original signal data. By carrying out this process the original signal is preserved (to within the accuracy of the FFT and FFT^{-1} algorithms) but now the resolution has been increased by a factor of n. If we are to assume an interpolation factor of $n = 10$ then the above process is illustrated in the following Fig.3.4 simulations where two signal tones of 20 Hz and 100 Hz are combined, and measured at a sampling rate of 1000 Samples/s for 1 second (so 1000 samples in total).

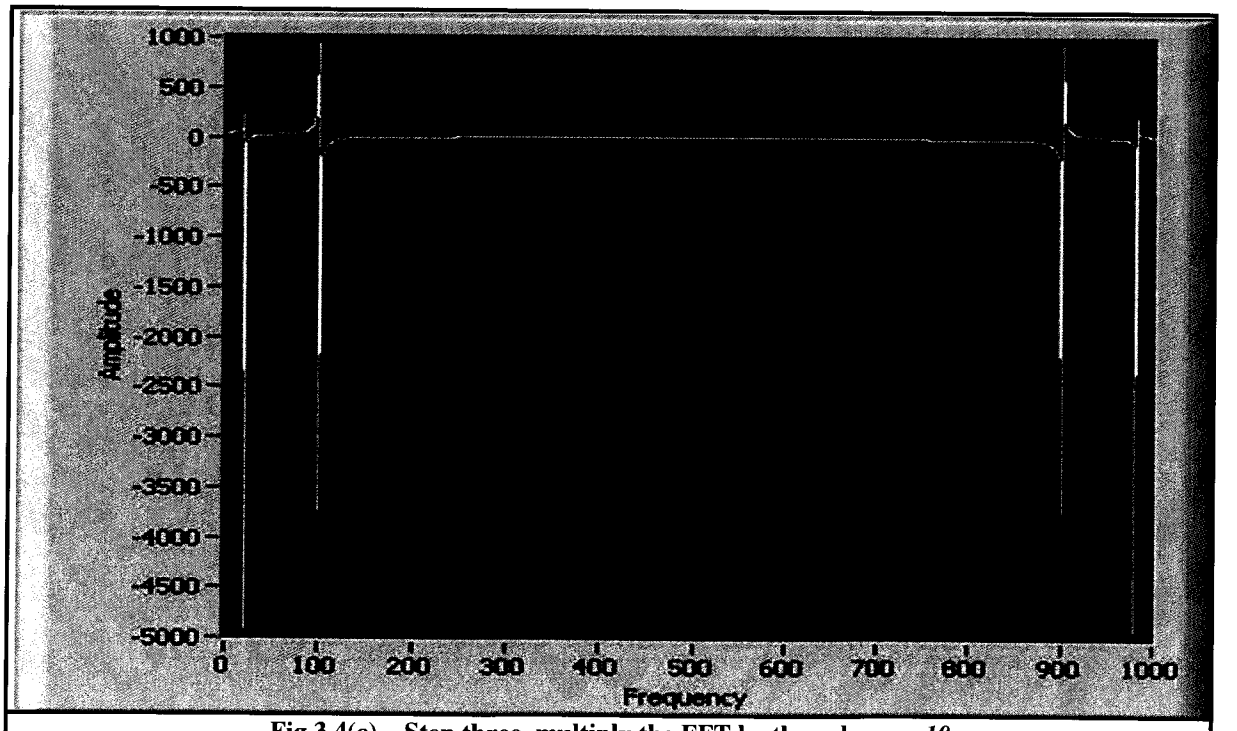

Fig.3.4(c) – Step three, multiply the FFT by the value $n = 10$

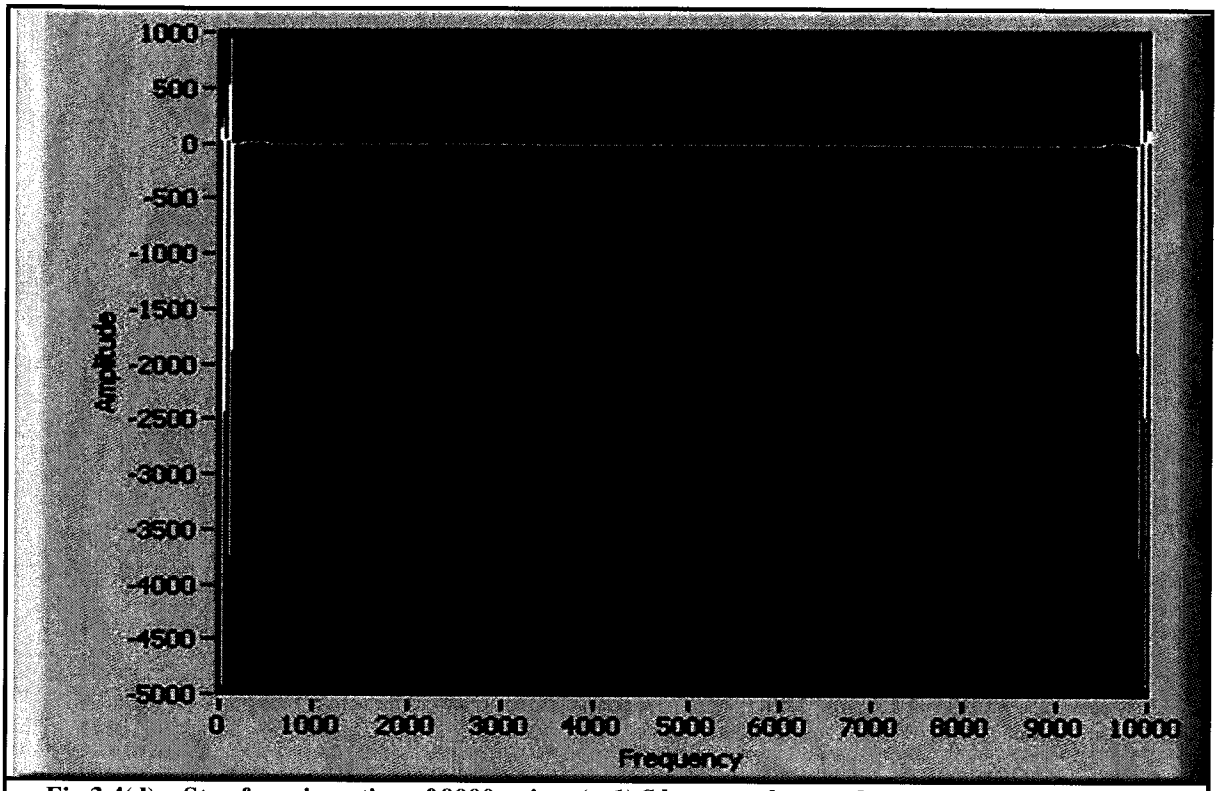

Fig.3.4(d) – Step four, inserting of 9000 points *(n-1)·S* between the υ and –υ components of the FFT

Fig.3.4(e) – Step five, the FFT^{-1} of Fig.3.3d back into the original domain of the beating signal. The white lines represent the positions of the original un-interpolated data while the extra red dots represent those that were added from the Fourier interpolation process.

This LabVIEW coding can be seen in Fig.3.5 below:

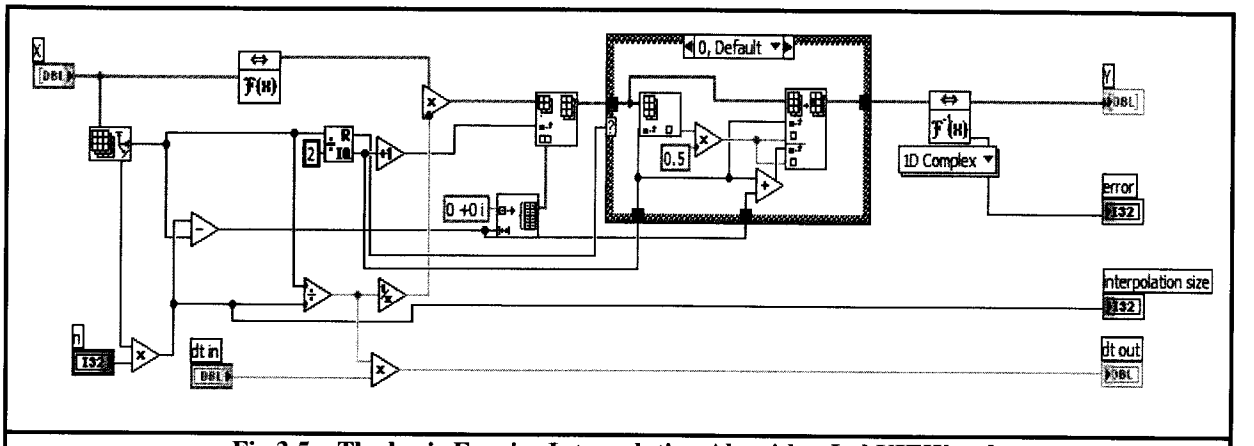

Fig.3.5 – The basic Fourier Interpolation Algorithm LabVIEW code

which is applied to the end of step 7 and step 8 in §3.2 to each Δx segment which in turn increases the resolution of its spectral response by a factor n.

3.4 Extended Optical Sweep Range (EOSR) Algorithm

In Chapter 6, I will discuss how much of an improvement to SNR is obtained by averaging over several identical sweeps. Although significantly improving the accuracy of the wavelength shift measurements at specific locations, this type of averaging also greatly increases the overall measurement time since a single scan can take several seconds each. If the stimulus applied to the FUT is slowly varying with respect to time then this is not a problem, but if the temperature changes, stress/strain, etc.... are more dynamic in nature (changes over a few seconds or less) this can present a problem because the final averaged wavelength shift can become distorted and will not reflect the true status of the FUT at that location. As a workaround to this problem, to try to maintain the accuracy from the averaging over several sweeps, yet cut down on the time needed - I developed the EOSR algorithm.

From (3.1), we know that the spatial resolution is: $\Delta z \cong \frac{\lambda^2}{2n_g \Delta\lambda}$. Accordingly, if we have a central wavelength of $\lambda=1520nm$, and a sweeping range of $\Delta\lambda=10nm$ then our spatial resolution, Δz is approximately 79μm for an effective index $n_g = 1.4682$. On the other hand, if we were to use a sweeping range of 100nm then the spatial resolution would drop down to 7.9μm or 10 times smaller. This same fiber segment Δx now has 10 times the number of points in it compared to its respective 10nm sweep. Since there is effectively 10 times the data for the same segment, the EOSR works by effectively downgrading the spatial resolution across the entire FUT by summing n adjacent elements of the spatial domain FUT array and then dividing them by the same factor. By doing so, the dynamic wavelength shift sensing range in the frequency domain is decreased by a factor of n, yet the SNR is increased because of the averaging. The LabVIEW coding of this grouping/averaging is seen in Fig.3.6 below:

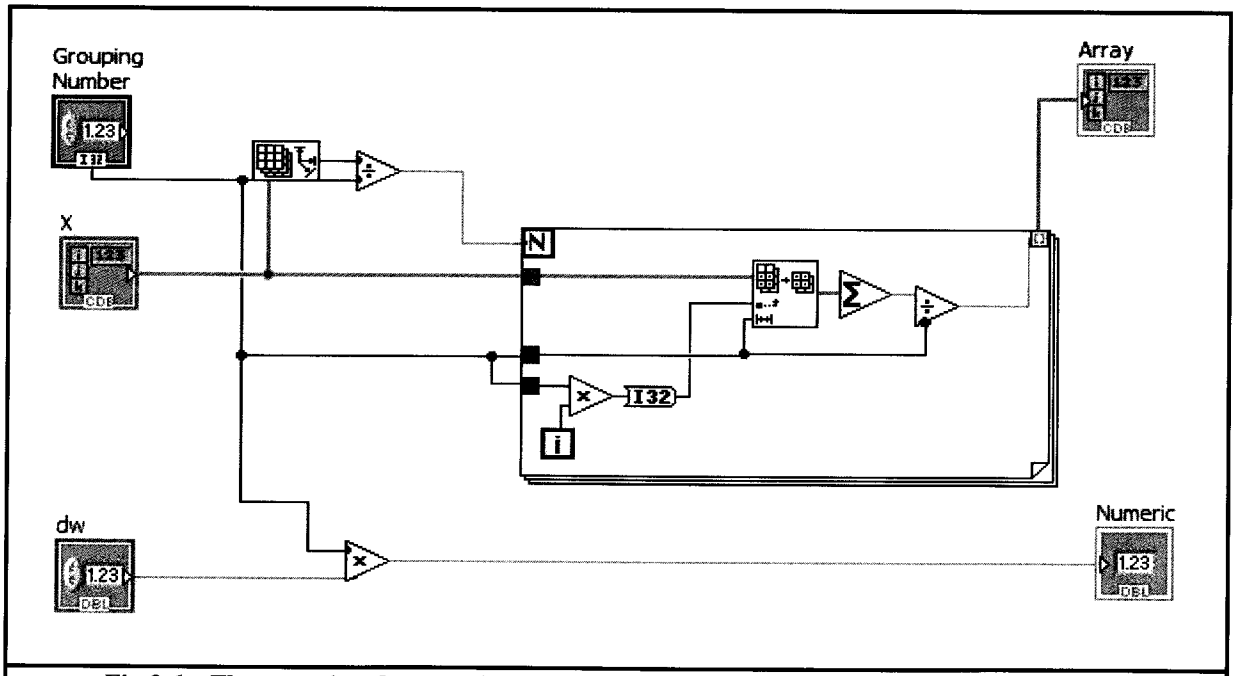

Fig.3.6 – The grouping & averaging portion of the LabVIEW code of the EOSR algorithm

and is applied at the end of step 3 and step 4 of the process in §3.2 for the FUT. The Fourier Interpolation Algorithm as described in §3.3 is applied to each segment Δx by that same factor n to increase the resolution spectral response by the same degree.

3.5 Boxcar Filter (BF) Algorithm

When a FUT is either heated and/or having stress applied to it at a specific location Δx, the stimulus is never totally confined to just that location but diffuses into the surrounding region. Likewise, if the stimulus is applied at the position *(x-1)* its effects are also manifested to varying degrees also at the positions *(x-2),* and *x*. To better take these effects into account as well as minimize the background noise from multiple scatters and oscillator noise this algorithm applies a boxcar filter/moving mean window at the end of steps 3 and steps 4 of the process in §3.2 for the FUT. The LabVIEW code for this Boxcar Filter Algorithm can be seen in Fig. 3.7 below:

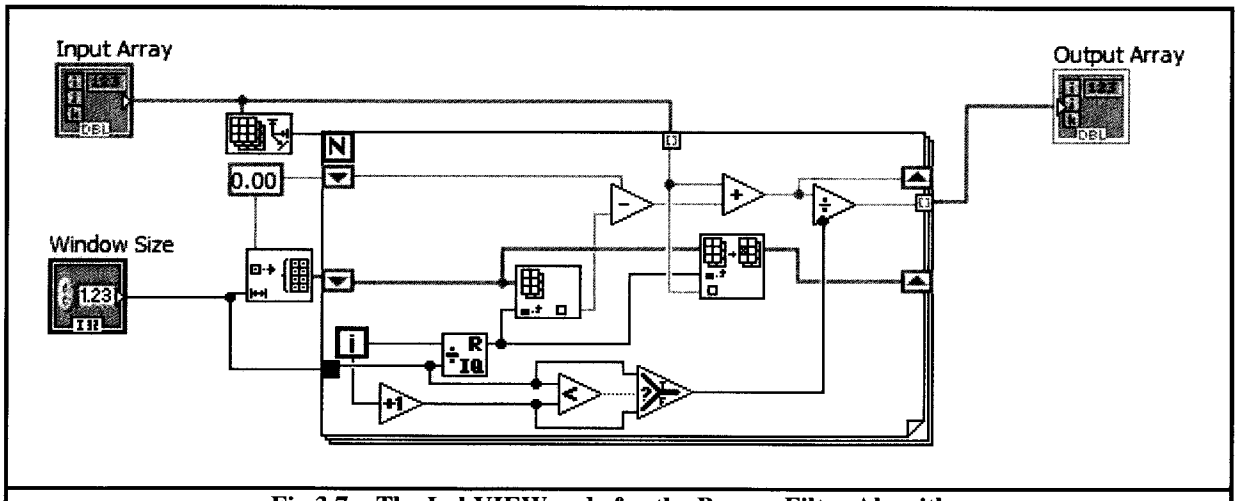

Fig.3.7 – The LabVIEW code for the Boxcar Filter Algorithm

After the running mean was applied to the FUT then like EOSR algorithm the Fourier Interpolation Algorithm, as described in §3.3, is applied to each segment Δx by that same factor *n* to increase the resolution spectral response by the same degree - which in this case is the same size as the boxcar filter window.

3.6 Extended Segment Size (ESS) Algorithm

As was pointed out in (3.8), when doing the classical analysis to detect the wavelength shift for sensing purposes the resolution of the spectral response is primarily dependent on the segment size - the larger the segment size, the better the spectral resolution. The larger the segment size the better SNR as well, so long as the stimulus is applied uniformly across the section. To use this segment size strength to its fullest potential the ESS algorithm was developed which is similar to the BF algorithm in many regards. For this algorithm a segment size, Δx of say 1cm is used in the analysis for the wavelength shift, but instead of shifting a full $|\Delta x|$ increment in the array to repeat the process, the shift is instead $|\Delta x/n|$ such that n wavelength shift values are obtain throughout the increment Δx. This leaves several options of what to do with these n values: a) the peak positions of each of these n values can be averaged to further improve the SNR, or b) the actual amplitudes for each of these n values can be individually inspected. The purpose for this is that the higher the peak value measured from a cross-correlation, the more uniform the stimuli that is applied across the whole segment. Although this cross-correlation is carried out in the spectral domain, the peak amplitude which is inversely proportional to the degree of distortion/uniformity of the stimulus also provides information regarding the *precise position* and *symmetry* of the stimulus itself in the spatial domain. This is extra information that the other algorithms do not directly provide. A diagram data grabbing process can be seen in Fig.3.8. This is a modified version of steps 7 and 8 described in §3.2. As with the other algorithms this is also followed up by the carrying out of the FIA of factor n.

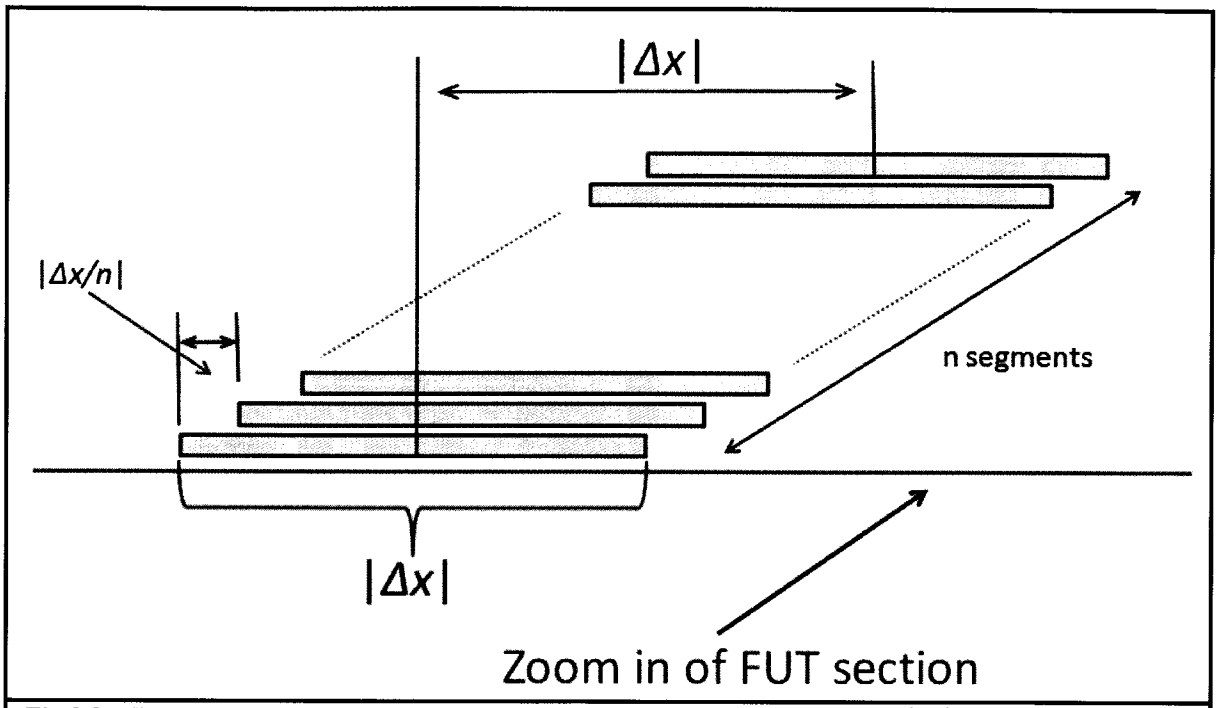

Fig.3.8 – The ESS algorithm, from center-to-center *n* array segments of size |*Δx*| spread over distance |*Δx*| uniformly shifted by |*Δx/n*|

The LabVIEW code for the ESS algorithm can be seen in Fig.3.9 below:

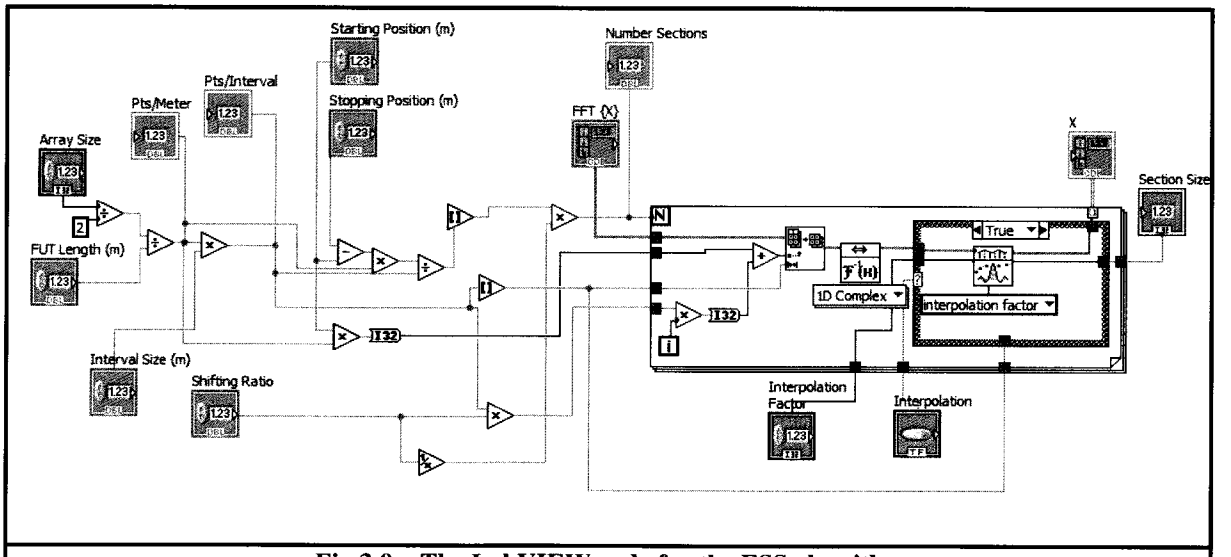

Fig.3.9 – The LabVIEW code for the ESS algorithm

3.7 Accuracy, Resolution, and SNR Comparisons of These Algorithms

The purpose of this section is to compare the performance of the algorithms which were described in §3.2-3.6. This will be done by looking at the cross-correlations of the initial and final spectral responses using a 5cm FUT section of data which was acquired using the polarization diverse setup described in chapter 2. Accordingly, the setup and raw data shall remain the same for this comparison – the only thing varying shall be the way the data is manipulated to detect the wavelength shift in 5 consecutive 1cm segments on the FUT.

A typical cross-correlation in the spectral domain of a 1cm section of the FUT can be seen in Fig. 3.10 below:

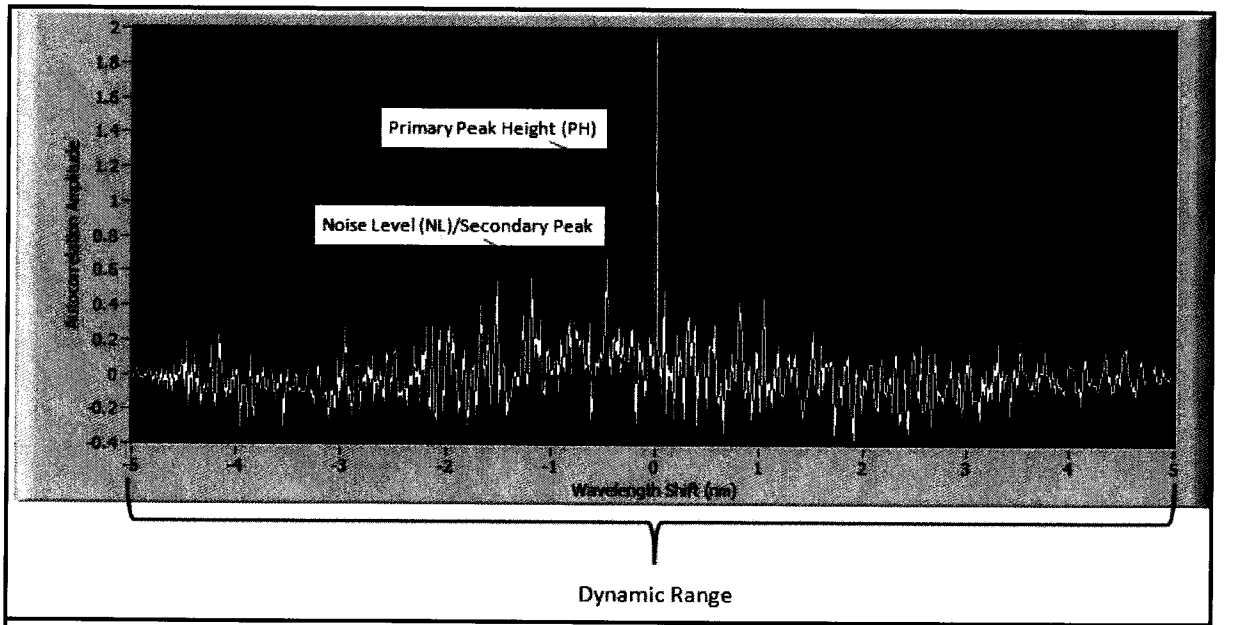

Fig.3.10 – A complex cross-correlation of a 1cm section of an FUT in the spectral domain with Rayleigh backscattered light as the primary sensing mechanism

From this figure, the parameters which shall be compared among the different algorithms are the: **a)** *dynamic range (DR)*, **b)** spectral *resolution (SR)* = *(dynamic range/# points)*, **c)** *SNR* = *PH/NL* (where PH is the primary peak height while NL is the noise level), and **d)**

wavelength shift accuracy of temperature measurement compared to a thermocouple reference source. Out of the 5cm fiber section that shall be looked at, its centre is heated across a 1cm span. The measured temperature using a thermocouple is 77.6 ± 3.0 °C. The room temperature at the time was 24.0 °C so the relative temperature was 53.6 ± 3.0 °C. It should be noted that the ± 3.0 °C for the previous two measurements is so large because of the inaccuracy of the thermocouple used – not the optical setup. As will be covered in Ch.6 the temperature calibration value for this setup and fiber type is a wavelength shift of 9.04 ± 0.65pm/°C. Thus the reference source comparison value for (d) will be 484.5 ± 44.1 pm.

3.7.1 Results from the Classical Algorithm Described in §3.2

For this algorithm, 5 different wavelength sweeping ranges are looked at. These are: 5nm (1470-1475nm), 10nm (1470-1480nm), 20nm (1470-1490nm), 40nm (1470-1510nm), and 60nm (1470-1530nm) respectively and the results are shown in Table 3.1. It should be noted that the first two ranges as well as the last two experienced a 0nm wavelength shift.

Table 3.1 – Classical Algorithm Performance

Δλ (nm)	*DR (nm)*	*SR (pm)*	*SNR Over 5 Consecutive 1cm Segments (dB)*					*Avg. SNR*	*Central Wavelength Shift Value (nm)*	*Measured λ Shift Minus Ref. (pm)*
5	±2.5	78.1	3.6	0.06	0.65	2.50	1.70	1.89	0.4883	3.8
10	±5.0	78.1	0.68	0.62	0.64	2.31	3.22	1.63	0.4331	51.4
20	±10.0	78.1	0.95	1.57	0.57	2.30	0.31	1.20	0.4545	30.0
40	±20.0	78.1	0	0.49	0.33	0.87	0.86	0.52	0.5501	65.6
60	±30.0	78.1	2.36	0.07	0.11	0.93	0.04	0.80	0.5330	48.5

Looking at Table 3.1 one can see that with the classical algorithm in the spectral domain no improvement in spectral resolution is achieved, as well there is also a slight degradation in the average SNR as the sweeping range is increased. The only real benefit that one gets by

increasing $\Delta\lambda$ is that the dynamic sensing range increases linearly with it. All of the above measured wavelength shift values are accurate to within their errors (which half of the SR) and those of the reference value taken by the thermocouple but of these the one with the largest overlap is that of the 5nm sweep which is good because: a) it is the smallest data set of the 5, as well as b) the dynamic range is the closest to the actual temperature range used.

3.7.2 Results from the Fourier Interpolation Algorithm described in §3.3

Since in the previous subsection the 5nm sweep performed the best then this is the sweeping range that shall be used in the following analysis. The interpolation factors n that are used are 2, 5 ,10, 15 and 20 and the results can be seen in Table 3.2 below:

Table 3.2 – Fourier Interpolation Algorithm Performance

Interpolation Factor n	*DR (nm)*	*SR (pm)*	*SNR Over 5 Consecutive 1cm Segments (dB)*					*Avg. SNR*	*Central Wavelength Shift Value (nm)*	*Measured λ Shift Minus Ref. (pm)*
2	±2.5	39.05	0.75	0.84	1.18	2.24	1.59	1.35	0.4980	13.5
5	±2.5	15.62	2.02	0.62	0.35	2.09	1.12	1.30	0.4961	11.6
10	±2.5	7.81	2.08	0.78	0.55	2.10	1.29	1.41	0.4961	11.6
15	±2.5	5.21	3.18	0.86	0.30	2.21	1.09	1.66	0.4961	11.6
20	±2.5	3.90	2.76	0.76	0.26	2.13	1.06	1.49	0.4961	11.6

From Table 3.2 one can see that although the dynamic range and SNR basically stay the same we can get a factor of 20 improvement in the spectral resolution whereby it decreases from the 78.1pm down to 3.9pm. From a temperature resolution standpoint, this means that it goes from 8.6°C resolution down to 0.43°C for a 1cm segment.

3.7.3 Results from the Extended Optical Sweep Range (EOSR) Algorithm described in §3.4

As in the last two subsections I shall again use the 5nm as the *simulated* base sweeping range. I say *simulated* because in the spatial domain if I had done a 10nm sweep

but summed and averaged the array elements into groups of 2 then the number of elements that remained would be the same as if I had just carried out a 5nm sweep. The same holds if I do a 25nm sweep and sum them into groups of 5 in the spatial domain and so on. The results for this algorithm can be seen in Table 3.3 below:

Table 3.3 – Extended Optical Sweep Range (EOSR) Algorithm Performance

Δλ (nm)	*Interpol. Factor n*	*DR (nm)*	*SR (pm)*	*SNR Over 5 Consecutive 1cm Segments (dB)*					*Avg. SNR*	*Central Wavelength Shift Value (nm)*	*Measured λ Shift Minus Ref. (pm)*
10	2	±2.5	39.05	1.50	1.43	1.93	0.14	1.55	1.35	0.5177	33.1
20	4	±2.5	19.53	0.81	0.82	0.86	1.6	1.39	1.11	0.4915	7.0
40	8	±2.5	9.76	-0.11	0.29	1.54	-0.17	-0.04	-0.14	0.490	5.5
70	14	±2.5	5.58	0.42	0.30	0.4891	-0.65	0.26	-0.39	0.460	24.5

One of the things that was immediately noticed as larger sweeps were carried out and the neighboring array elements were clustered and averaged was that the SNR's of the cross-correlations started to degrade significantly. To the point that from about 40nm and higher the actual peak containing the wavelength shift information was of the same amplitude or even shorter than the peaks created by the surrounding noise. This in turn makes it difficult, if not impossible to tell which peak in fact is the correct one and in turn what is the correct temperature.

This could be attributed to the fact that these Rayleigh backscatter profile elements are in fact wavelength dependent. The sections of the SMF-28 FUT can be viewed equivalent to very weak FBG's with random periods. If one averages in the time/spatial domain over several sweeps then the wavelength/phase information is preserved. By averaging with neighboring elements from a single sweep as has been done with this algorithm one is in fact combining elements of different wavelength/phase dependency. This means the larger the grouping/averaging the more the actual wavelength shift information

that gets lost. It is because of the poor performance of this algorithm that it will no longer be looked at for the remainder of this thesis.

3.7.4 Results from the Boxcar Filter Algorithm described in §3.5

The boxcar filter can be viewed as a localized, sliding low-pass filter and has many applications among others things – real-time audio filtering. The results from the usage of this algorithm can be seen in Table 3.4:

Table 3.4 – Boxcar Filter Algorithm Performance

Window Size	*Interpol. Factor n*	*DR (nm)*	*SR (pm)*	*SNR Over 5 Consecutive 1cm Segments (dB)*					*Avg. SNR*	*Central λ Shift Value (nm)*	*Measured λ Shift Minus Ref. (pm)*
2	2	±2.5	39.05	0.62	0.16	0.11	0.04	0.19	0.23	0.15625	328.2
4	4	±2.5	19.53	0.03	1.92	0.64	0.14	0.37	1.75	0.03906	445.44
8	8	±2.5	9.76	0.11	0.02	0.58	1.03	1.04	0.68	0.03173	452.77

Although the BG algorithm is performing better than the EOSR algorithm as discussed in the previous §§, it has some negative attributes which are common to such filters. Among those, although smoothing of the frequency response data (thus eliminating potential noise spikes), it also inherently broadens (distorts) the peaks generated in the cross-correlation which in turn can potentially make it more difficult to determine in some cases both the primary peak position as well as its amplitude. It is because of this that the algorithm usually will not be the best choice if trying to detect the wavelength shift in regular SMF-28 fiber that is using Rayleigh backscatter as its sensing mechanism whereby the secondary peaks and noise may be of comparable amplitudes. One can use this algorithm though where FBG's are being used to detect the wavelength shift since Fresnel reflection is the primary mechanism in this case - which can be over 20dB stronger than the surrounding Rayleigh backscatter. This

means that the primary peak from the cross-correlation can be 20+ times higher in amplitude than its secondary peaks making differentiation between peaks not a problem, but the filter can still be used to smooth out the Rayleigh backscattering and noise peaks that can be superimposed on top on the main Fresnel peak, in turn reducing jitter and in turn temperature fluctuations on a sweep-to-sweep basis.

3.7.5 Results from the Extended Segment Size (ESS) Algorithm Described in §3.6

The results from this last algorithm are shown in Table 3.5 below:

Table 3.5 – Extended Segment Size (ESS) Algorithm Performance

Shifting Size (mm)	*Interpol. Factor n*	*DR (nm)*	*SR (pm)*	*SNR Over 5 Consecutive 1cm Segments (dB)*					*Avg. SNR*	*Central Wavelength Shift Value (nm)*	*Measured λ Shift Minus Ref. (pm)*
5	2	±2.5	39.05	1.39	2.09	1.17	3.10	0.51	1.74	0.5078	23.3
2	5	±2.5	15.62	1.18	1.13	1.18	1.16	1.34	1.20	0.4944	9.9
1	10	±2.5	7.81	0.64	3.09	1.96	0.58	2.17	1.79	0.5109	26.4
0.5	20	±2.5	3.90	1.48	2.06	0.68	1.38	3.59	1.96	0.4945	10.0
0.25	40	±2.5	1.95	3.45	3.60	1.17	1.08	0.84	2.20	0.5057	21.2

The dynamic range and spectral resolution for the ESS algorithm are the same as those of the FI algorithm since the FIA is incorporated into it. Two additional improvements though are as follows: a) if we let n represent the segment size to shifting size ratio, then we have n values that can be averaged over. This in turn improves the SNR by a factor of $0.5\sqrt{n}$. The other strength is that: b) one can inspect the primary peak amplitudes, and SNR's for each of the individual sub-segments. Segments with lower amplitudes and SNR's represent segments that have a non-uniform/asymmetric stimuli being applied across it so these are the wavelength shift values that one could discard from the averaging process if one so wanted to further improve the accuracy.

Since this it is the algorithm that performed the best in all of the parameters looked at then this will be the one used in the two chapters that are to follow.

Chapter 4

Temperature, Longitudinal Stress and Twisting Measurement Results

In Chapter 2 I discussed the various OFDR setups used in this research, where as in Chapter 3 I discussed the limitations of using the classical methodology and introduced 4 additional algorithms that could be used to improve upon this. In Chapter 4 I shall now go into details into the performance of these setups and algorithms when using a stand SMF-28 as the FUT to do temperature measurements, longitudinal measurements, as well as torsional stress/twisting measurements.

4.1 Preliminary Temperature Measurements Using The PD OFDR Setup and the Classical Analysis Algorithm

The results presented in this section were some of my preliminary results meant to demonstrate that I could carry out temperature measurements with the polarization diverse OFDR setup using the unmodified 'classical' analysis. For this experiment the FUT which was comprised of 900μm SMF-28 fiber can be seen in Fig.4.1:

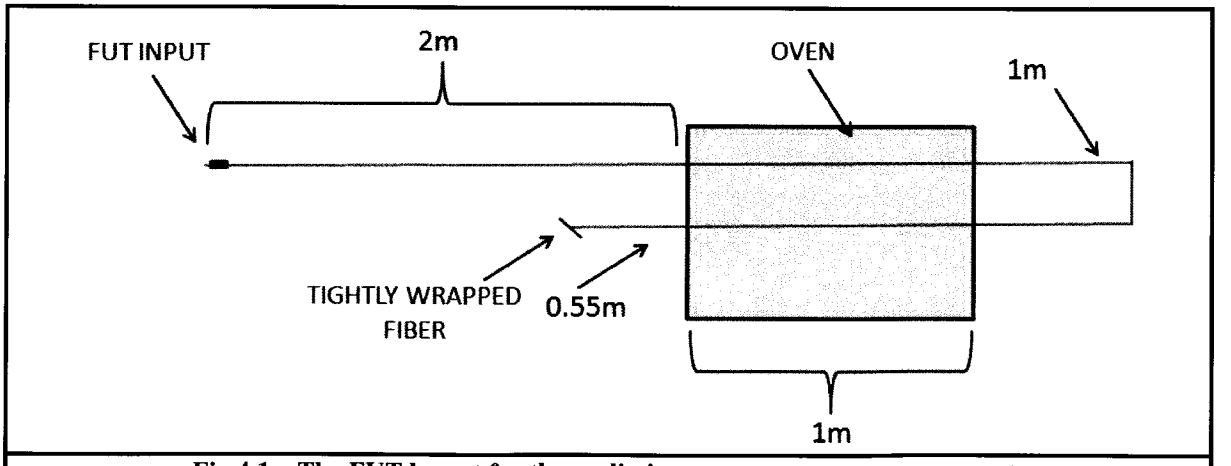

Fig.4.1 – The FUT layout for the preliminary temperature measurements

The cross-correlations with respect to position are shown in the intensity graph in Fig.4.2 below for 2cm segments across the FUT when heated to demonstrate the wavelength shift:

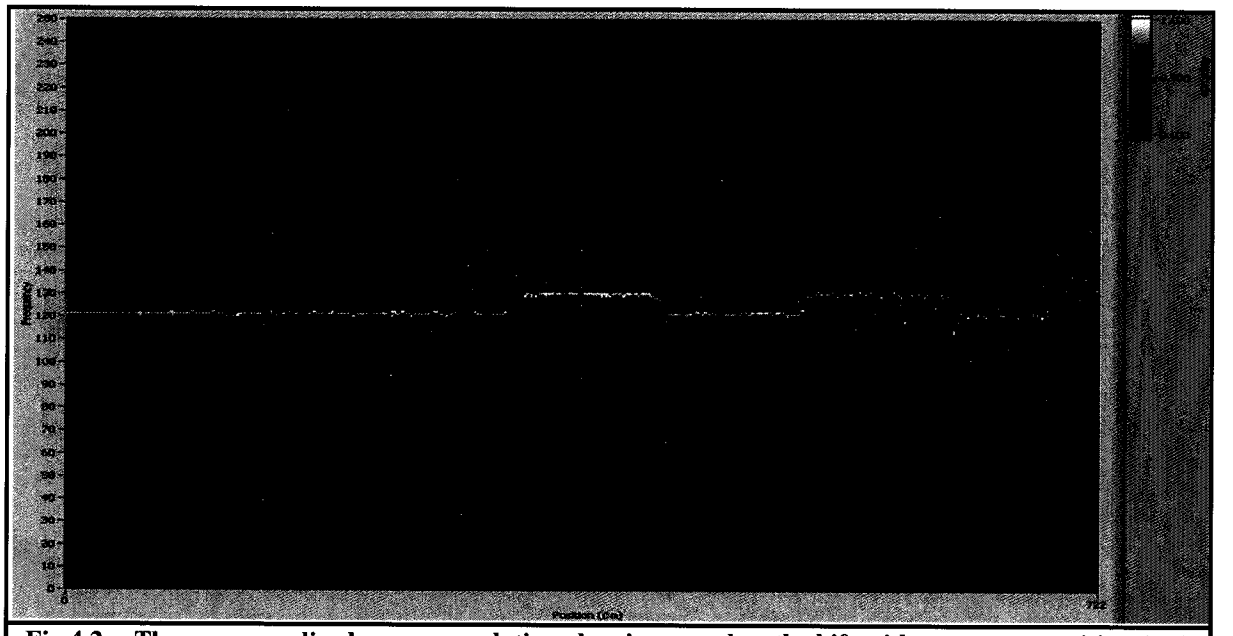

Fig.4.2 – The un-normalized cross-correlation showing wavelength shift with respect to position (cm) for the FUT given in 2cm segments

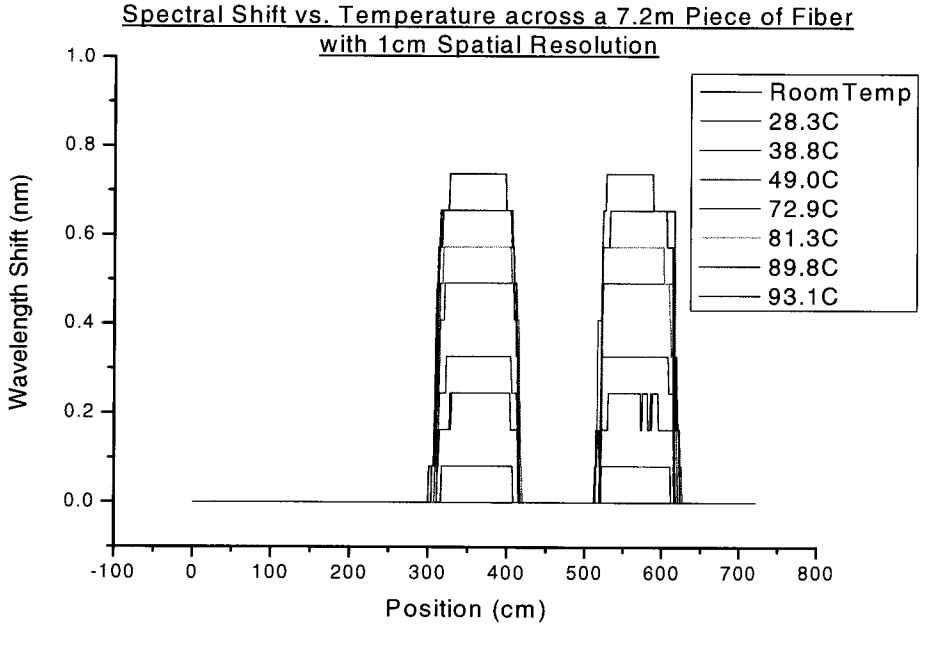

Fig.4.3 – Normalized wavelength shift vs. position for the FUT at various temperatures

The oven temperature was changed several times and the wavelength shifts with respect to position at these various temperatures are seen in Fig.4.3 above where the temperature outputs were given on the digital display of the oven. From the temperature value and wavelength shift information given in Fig.4.3 the wavelength shift vs. temperature relationship for the 900μm SMF-28 can be seen in Fig.4.4 below:

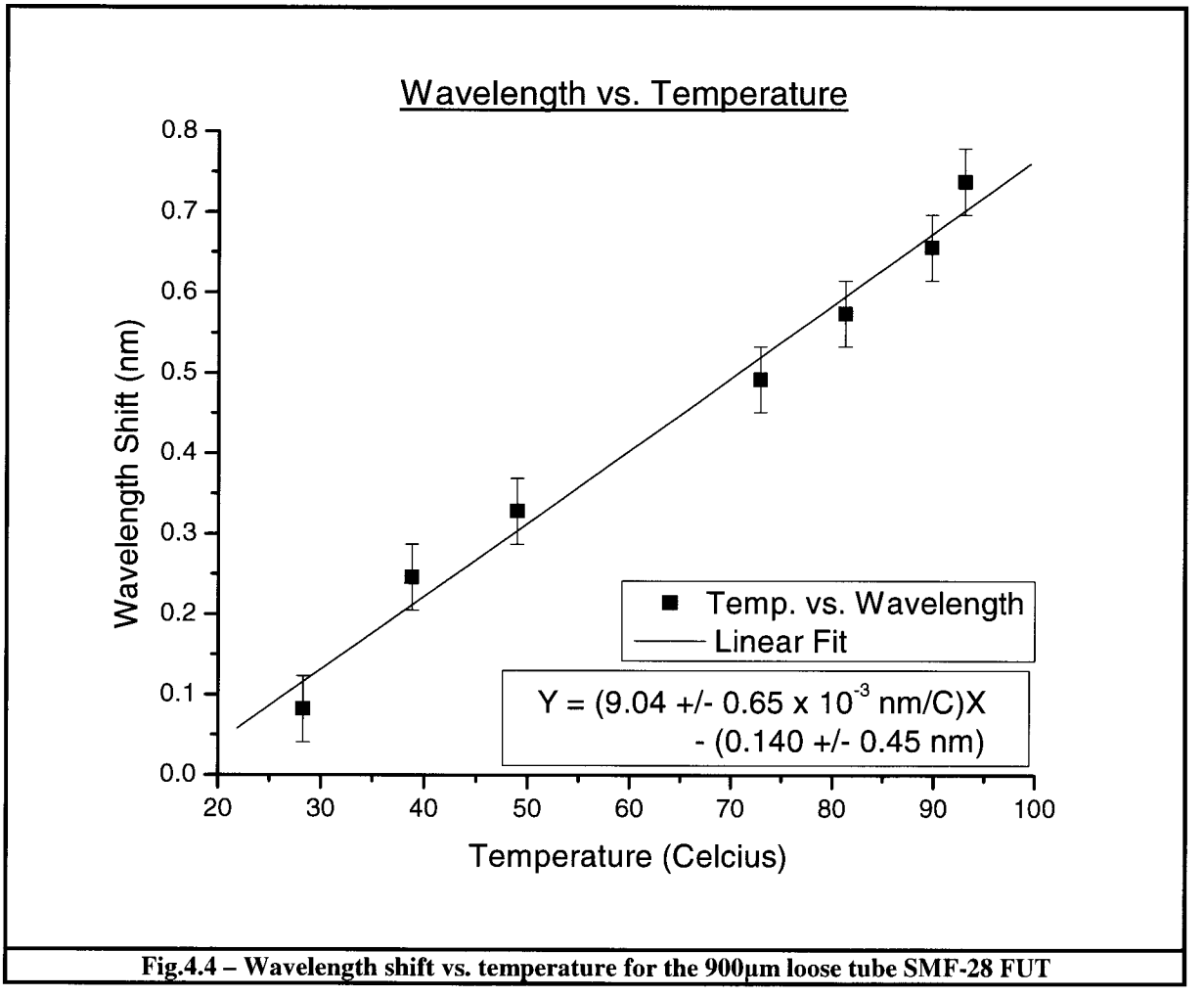

Fig.4.4 – Wavelength shift vs. temperature for the 900μm loose tube SMF-28 FUT

Accordingly for this fiber type the wavelength shift vs. temperature relationship was found to be 9.04 ± 0.65 pm/°C.

4.2 Temperature Measurement Performance of the 5 OFDR Setups using the ESS Analysis Algorithm

The previous section showed that the PD OFDR setup in conjunction with the classical algorithm was capable of doing temperature measurements when 1m sections of the FUT were heated. The purpose of this section is: a) to show that in fact temperature measurements can still be carried out when only a 1cm section of the FUT is heated, b) to compare the jitter and noise performance of the 5 different OFDR setups back in the spectral domain by looking at the cross-correlations and accordingly the wavelength shifts of the frequency responses when heated, and c) to show how much of an improvement in resolution and accuracy was achieved in finding the wavelength vs. temperature shift of standard SMF-28e fiber.

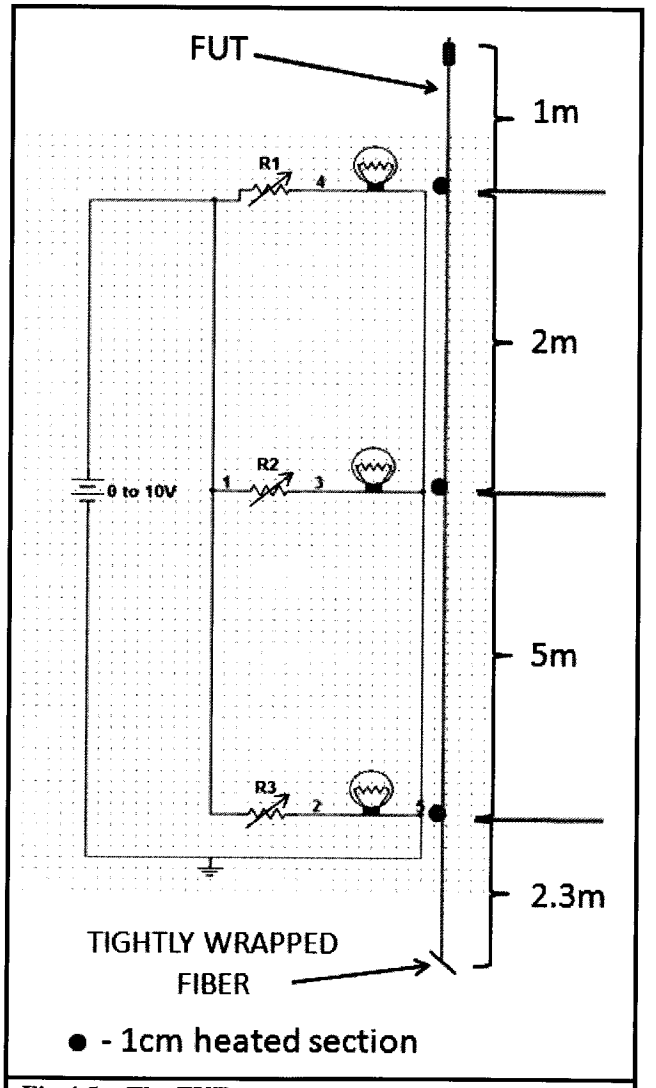

Fig.4.5 – The FUT temperature setup used to test the 1cm resolution.

A diagram of the FUT used to test the 1cm resolution of the 5 OFDR setups can be seen in Fig.4.5. The FUT is comprised of an 10.3m piece of regular SMF-28e fiber where there is an FC/APC connector at one end and the other end is wrapped tightly to attenuate the signal and minimize back-reflection from the end of the fiber. At the 1m, the 3m, and the 8m positions there are 1cm heating elements. The

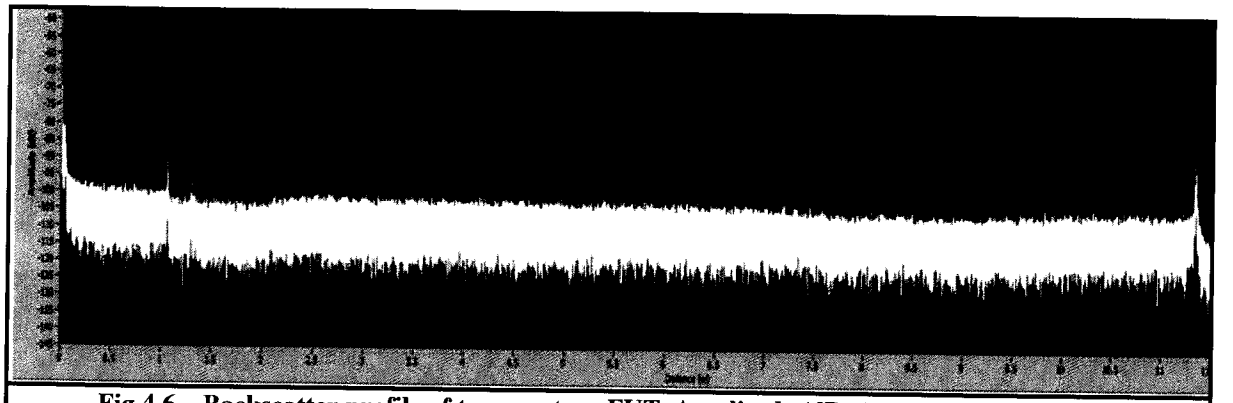

Fig.4.6 – Backscatter profile of temperature FUT, Amplitude (dBm) vs. FUT Distance (m)

voltage on the power supply is varied which in turn varies the temperature proportionally at the 3 separate elements. In Fig.4.6 one can see the backscatter distribution of this FUT as was interrogated using the *Polarization Diverse OFDR Setup* described in §2.5.2 across a 5nm sweep. The temperatures of the heating elements as they were measured by an in-lab thermocouple can be found in Table 4.1:

Table 4.1 – Temperature measurement values of the 3 heating elements by thermocouple

#	T1 (°C)	Rel. T1 (°C)	Rel. Δλ1 (pm)	T2 (°C)	Rel.T2 (°C)	Rel. Δλ2 (pm)	T3 (°C)	Rel. T3 (°C)	Rel. Δλ3 (pm)
1	22.3±0.2	0.0±0.3	0.0±0.0	22.3±0.2	0.0±0.3	0.0±0.0	22.3±0.2	0.0±0.3	0.0±0.0
2	22.7±0.2	0.4±0.3	3.62±0.30	22.7±0.2	0.4±0.3	3.62±0.30	22.7±0.2	0.4±0.3	3.62±0.30
3	24.2±0.2	1.9±0.3	14.4±2.5	24.4±0.2	2.1±0.3	19.0±3.0	26.0±0.2	3.7±0.3	33.4±3.6
4	25.5±0.3	3.2±0.4	28.9±4.3	26.6±0.3	4.3±0.4	38.9±3.9	26.6±0.3	4.3±0.4	38.8±4.6
5	28.3±0.4	6.0±0.4	54.2±5.3	31.1±0.4	8.8±0.4	79.6±6.8	32.3±0.4	10.0±0.4	90.4±7.68
6	29.9±0.5	7.6±0.5	68.7±6.7	34.3±0.5	12.0±0.5	108.5±9.0	35.6±0.5	13.3±0.5	120.2±9.8
7	36.5±0.5	14.2±0.5	128.4±10.3	39.7±0.5	17.4±0.5	157.3±12.2	37.6±0.5	15.3±0.5	138.3±10.9
8	47.1±0.7	24.8±0.7	224.2±17.3	46.7±0.7	24.4±0.7	220.6±17.1	55.5±0.7	33.2±0.7	300.1±22.5
9	51.7±1.0	29.4±1.0	265.8±21.1	51.7±1.0	29.4±1.0	265.8±21.1	64.7±1.0	42.4±1.0	383.3±29.0
10	65.3±1.5	43.0±1.5	388.7±31.1	57.1±1.5	34.8±1.5	314.6±26.4	82.1±1.5	59.8±1.5	540.6±41.2
11	70.8±2.5	48.5±2.5	438.8±38.8	67.5±2.5	45.2±2.5	408.6±37.1	93.8±2.5	71.5±2.5	646.4±51.7
12	74.6±2.5	52.3±2.5	472.8±40.8	80.6±2.5	58.3±2.5	527.0±44.1	120.1±2.5	97.8±2.5	884.1±67.5
13	88.7±4.0	66.4±4.0	600.3±56.3	83.6±4.0	61.3±4.0	554.2±53.8	131.0±4.0	108.7±4.0	982.6±79.4
14	105.6±6.0	83.3±6.0	753.0±76.6	89.6±6.0	67.3±6.0	608.4±69.7	161.0±6.0	138.7±6.0	1253.8±105.2
15	122.6±8.0	100.3±8.0	906.7±97.4	95.2±8.0	72.9±8.0	659.0±86.5	166.1±8.0	143.8±8.0	1300.0±118.2
16	143.7±10.0	121.4±10.0	1097.5±120.0	104.4±10.0	82.1±10.0	742.2±105.0	173.0±10.0	150.7±10.0	1362.3±133.3

The *Relative Temperature* is just the original measured temperature minus the room temperature of 22.3±0.2, while the relative wavelength shift $\Delta\lambda$ is the *relative temperature* times the conversion factor found in Fig.4.4 (9.04 ±0.65 pm/°C).

When setting the voltage of the heating element's power supply to 14V the temperatures of the 3 elements are shown in row 15 of Table 4.1. For a segment size set at 1cm - using the ESS algorithm with a shifting size of 0.25mm (getting a total of 40 points/cm) then averaging over 0.5cm intervals - Fig. 4.7 presents the wavelength shift profile vs. position for the basic, polarization diverse, differential, quadrature, and differential quadrature OFDR setups respectively. The wavelength shift values presented are the positions of the peaks of the highest amplitude found from the cross-correlations of each segment. Although the positions of the heated sections are visible for each of the setups that carried out the measurements, there is also noise apparent for each of the setups as well. Not surprising, the degree of noise from highest to lowest for these setups in the frequency domain follows the same order of lowest to highest SNR ratios for the setups given in Table 2.3 for the spatial domain. Thus the polarization diverse setup performed the poorest while the differential quadrature setup performed the best. Now it should be noted that if a peak tracking algorithm was used to track the proper peak (not necessarily the highest amplitude peak) based on the approximate wavelength shift vs. temperature relationship given in §4.1, or if the profiles were averaged over several laser sweeps then the noise could be reduced if not eliminated all together – but neither was applied to the results shown in Fig.4.7 to illustrate the capabilities of each setup from just a single sweep and with no prior knowledge of the wavelength shifting range which is often the case out in the field. Since the differential quadrature setup is the one that performed the best in both the spatial as well as frequency domains then this will be the only setup used in presenting the results in the remainder of this section as well as §4.4 and §4.6.

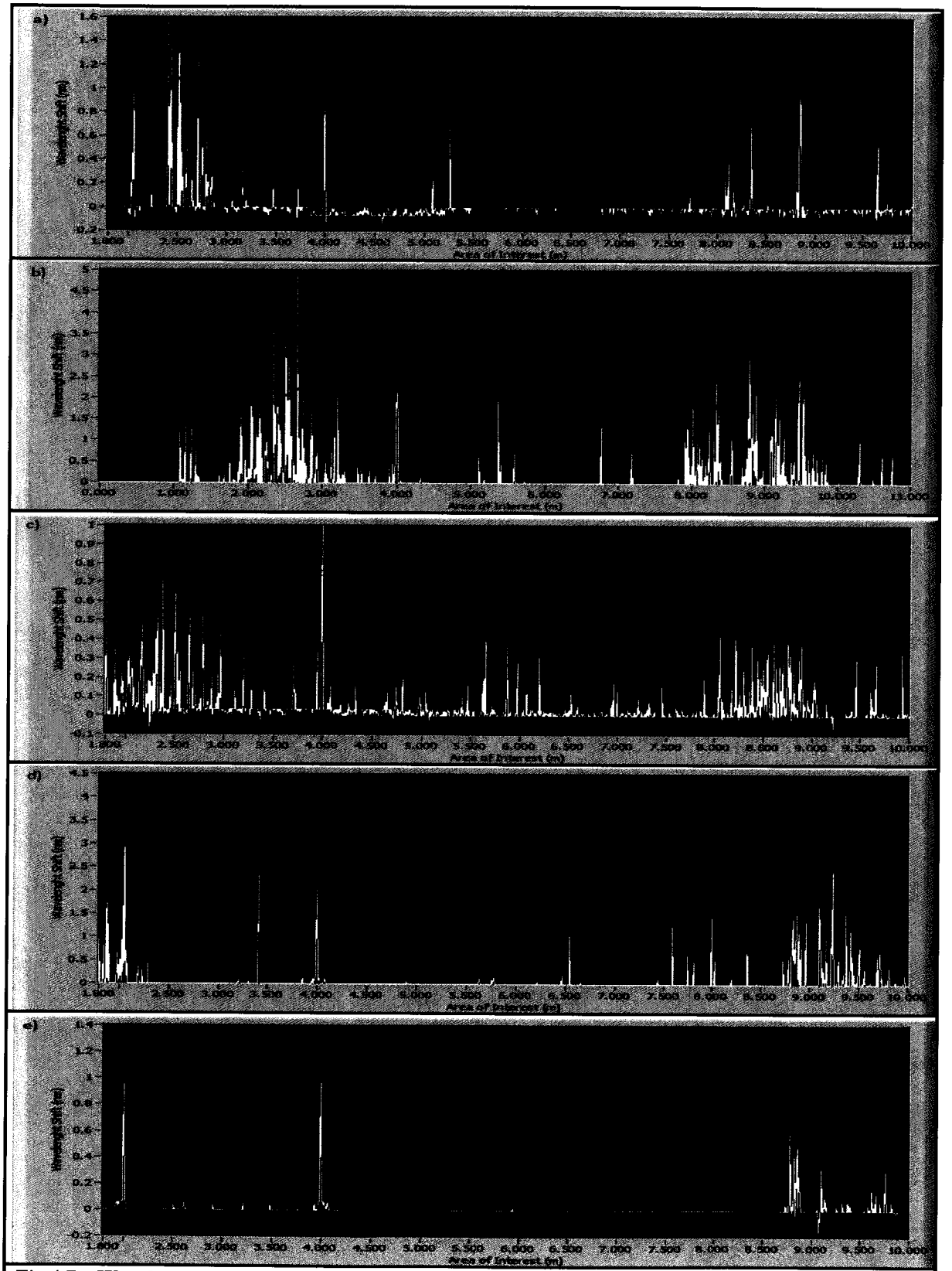

Fig.4.7 – Wavelength shifting profiles for the 5 OFDR setups of: a) the Basic, b) Polarization Diverse, c) Differential, d) Quadrature, and e) Differential Quadrature respectively for a single sweep of the laser.

Temporarily ignoring the few random noise spikes seen in Fig.4.7(e) and focusing in on the area around the heating elements, what is seen in Fig. 4.8 below is the distance vs. wavelength plot for all the temperatures seen in Table 4.1 as well as the wavelength shift vs. temperature relations for each of the 1cm segments that are being heated by the three elements. It should be noted that the temperature axes for Fig.4.8(b), (c), and (d) were obtained using thermocouples where their error increased as the temperature increased. So again the larger error bars are not dependent on the optical setups only on the reference used.

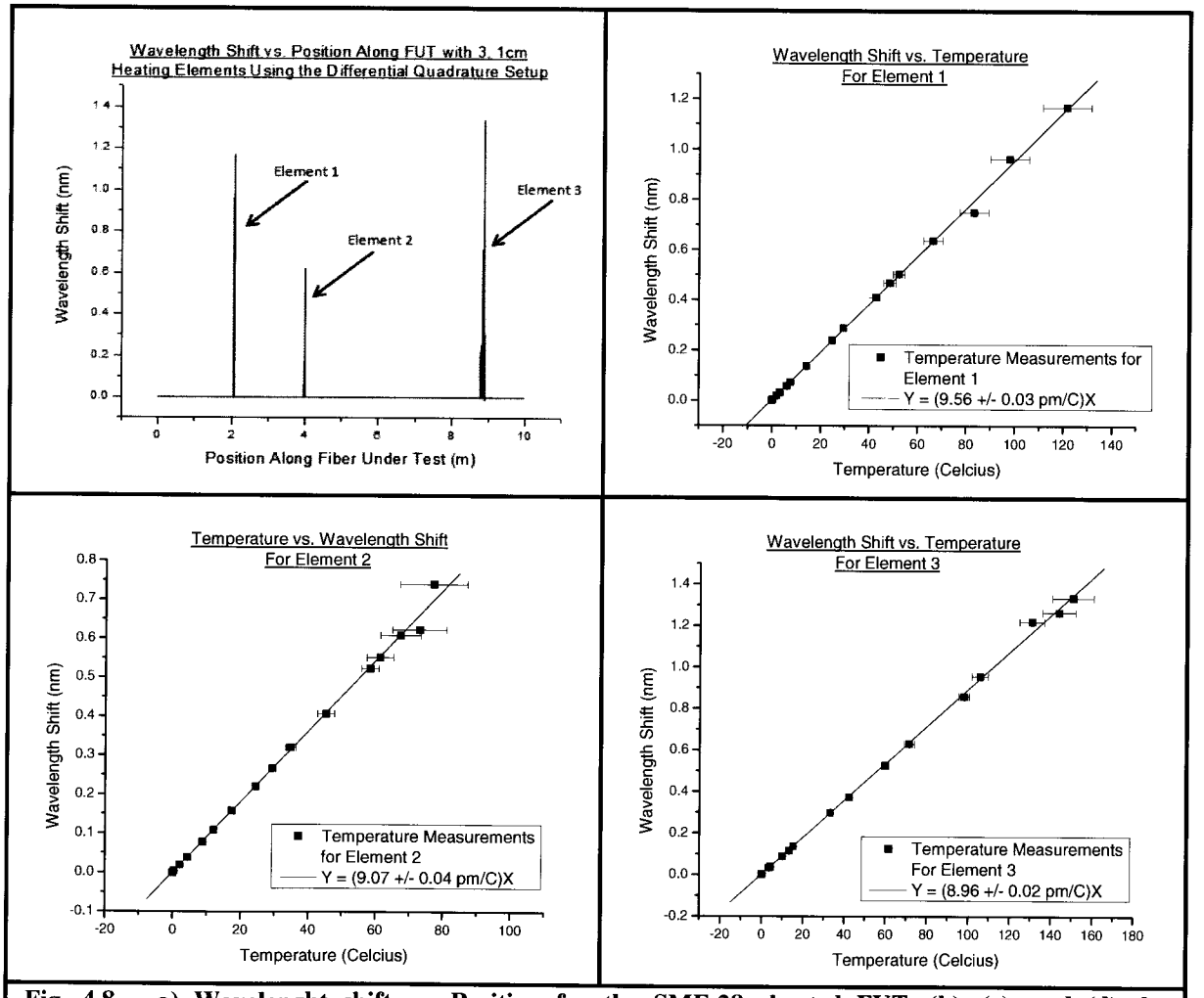

Fig. 4.8 – a) Wavelenght shift vs. Position for the SMF-28e heated FUT, (b), (c), and (d) the wavelength shift vs. temperature curves for each of the 3, heated 1cm sections respectively.

Based on such, the average wavelength shift vs. temperature relationship for the SMF-28e fiber was found to be: 9.20 ± 0.05 pm/°C.

4.3 Preliminary Longitudinal Stress Measurements using the PD OFDR Setup and the Classical Analysis Algorithm

The results presented in this section were my preliminary measurements I had carried out to measure the wavelength shift caused by longitudinal stress being applied to the FUT - which again was 900μm standard SMF-28 fiber. The diagram for this FUT can be seen in Fig. 4.9. An initial spectral response was taken with no weight hanging from the clamp so that later on when weights were hung the cross-correlations were taken with respect to it. Found below is a graph of the wavelength shift with respect to FUT position, as well as

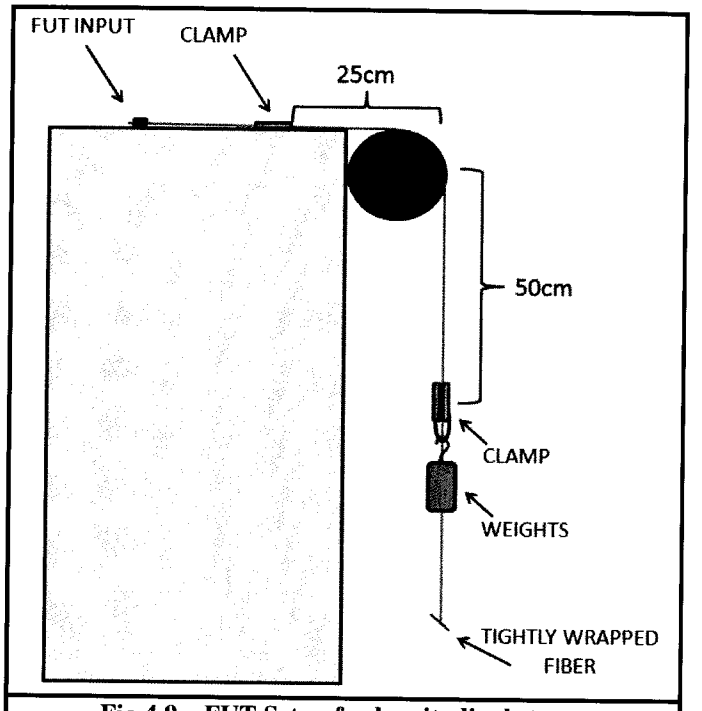

Fig.4.9 – FUT Setup for longitudinal stress.

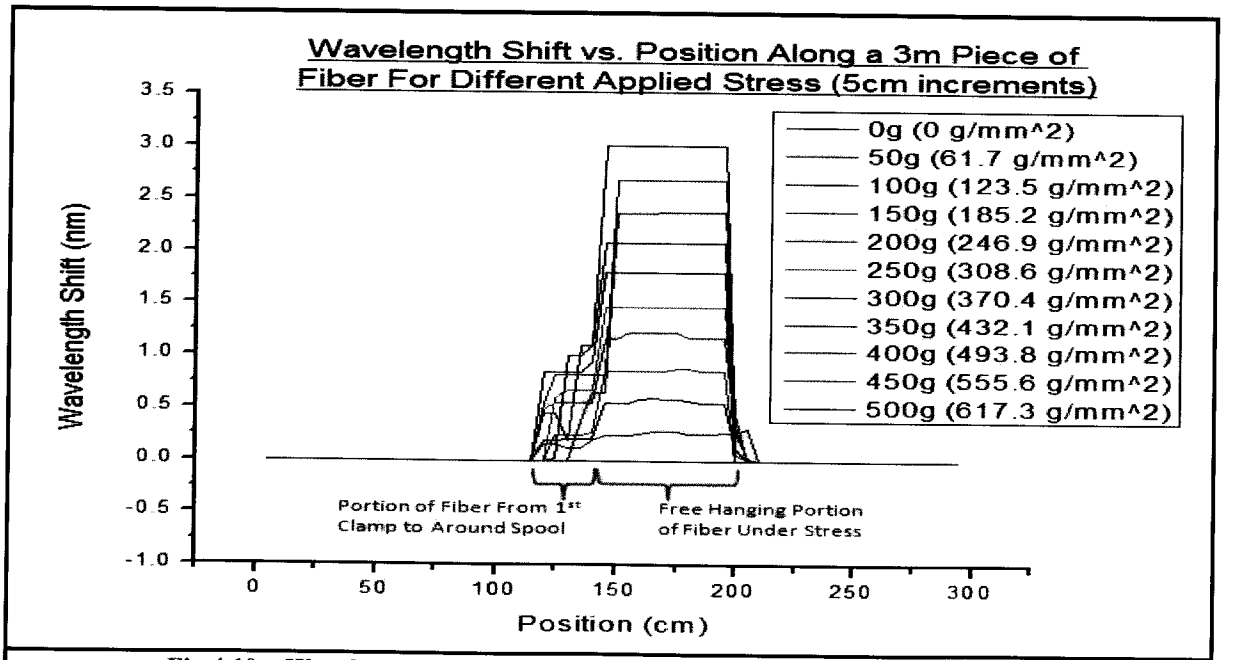

Fig.4.10 – Wavelength shift vs. position for the FUT at various applied masses

the wavelength shift vs. the applied hanging mass. Based on the above graph, for the 900μm SMF-28 fiber the wavelength shift is 6.01 ± 0.02 pm/g or 612 ± 2 pm/N.

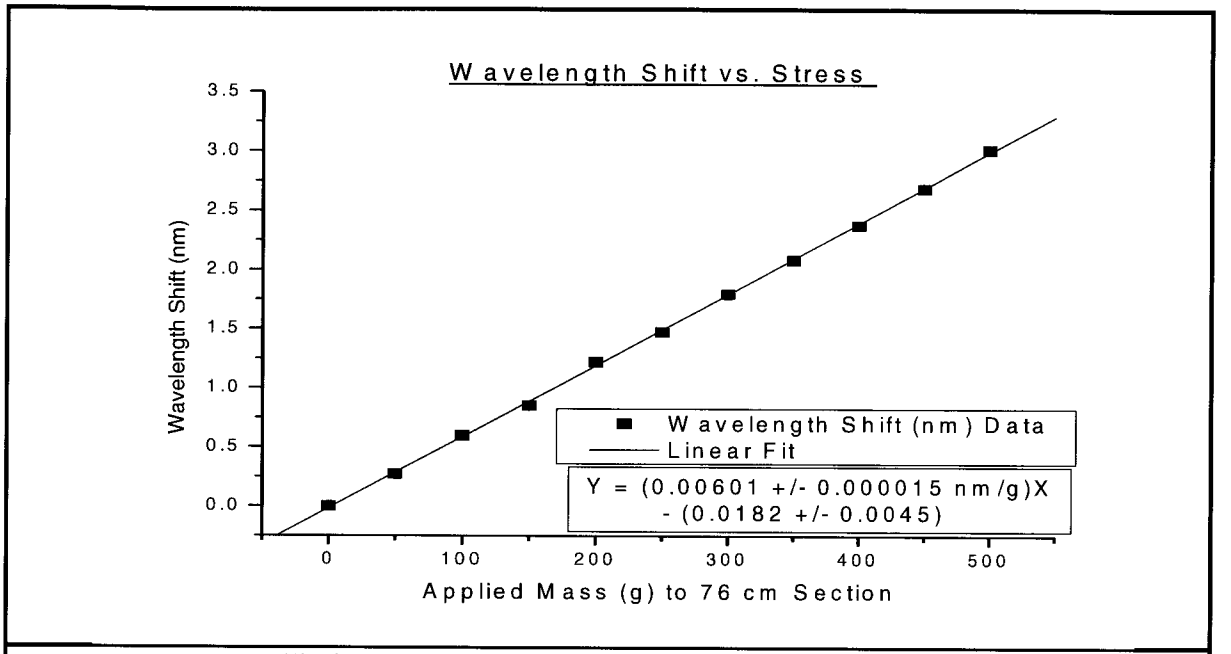

Fig.4.11 – Wavelength shift vs. Applied Mass for the FUT

4.4 Longitudinal Stress Measurement Performance of the 5 OFDR Setups using the ESS Analysis Algorithm

The previous section showed that the PD OFDR setup in conjunction with the classical algorithm was capable of doing longitudinal stress measurements. The following section tries to improve upon these results using the differential quadrature setup along with the ESS algorithm. The FUT setup is basically the same as that

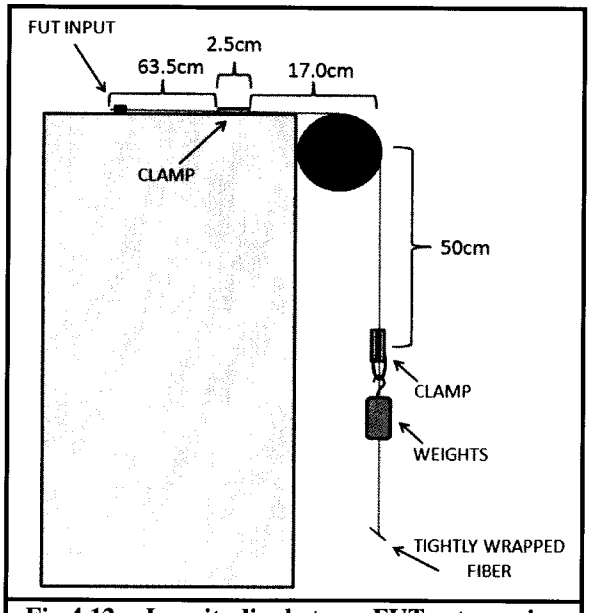

Fig.4.12 – Longitudinal stress FUT setup using 900μm SMF-28 fiber.

which was shown in §4.3 with the exception of slight changes in the lengths of the fiber and can be seen in Fig. 4.12. The backscatter profile for this FUT can be seen in Fig. 4.13 below:

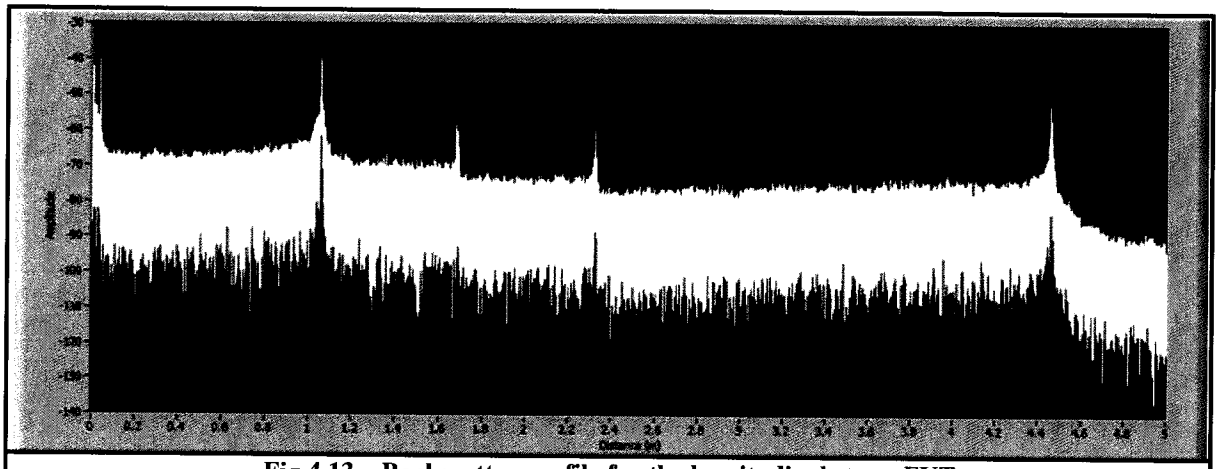

Fig.4.13 – Backscatter profile for the longitudinal stress FUT

The wavelength vs. position graph which focuses on the portion of the FUT under tension can be seen below:

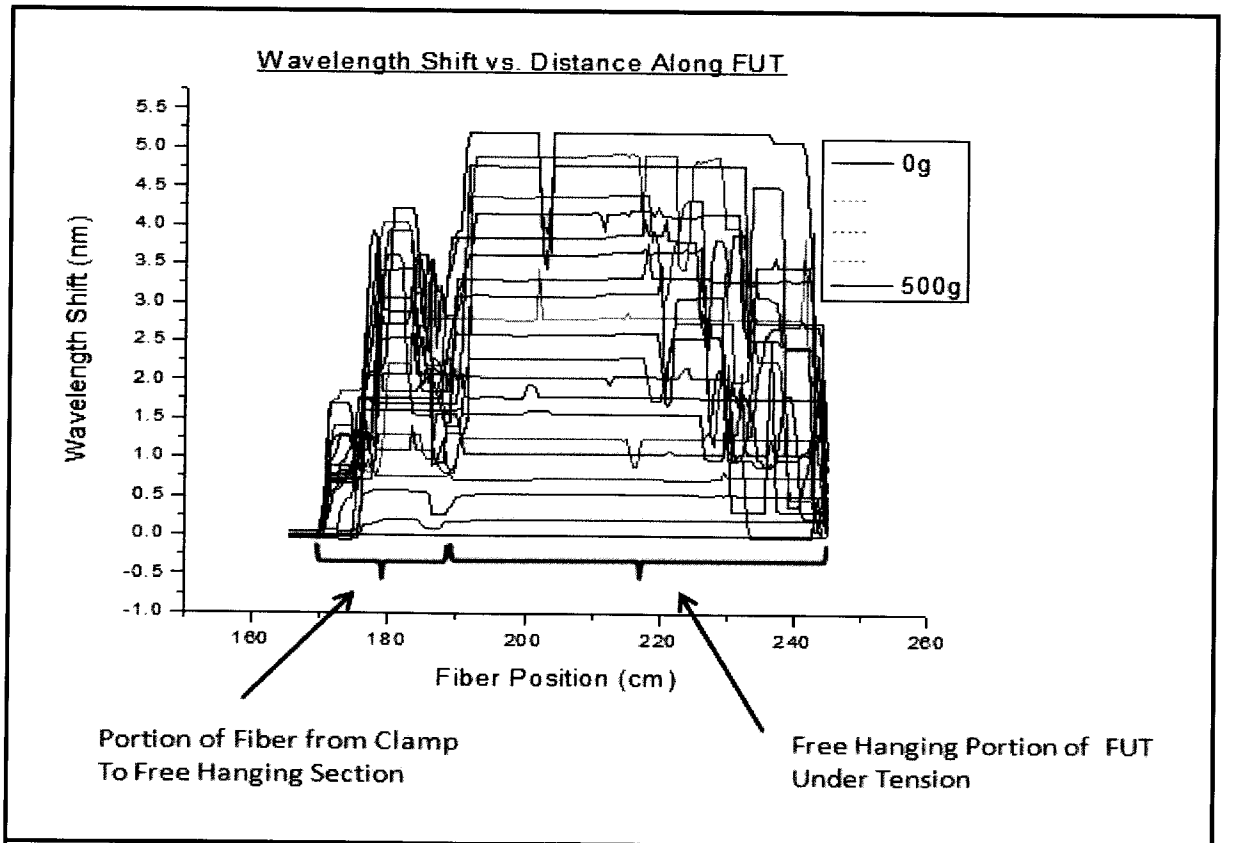

Fig.4.14 – Wavelength shift vs. distance along the FUT

Taking the results from Fig.4.14, the Wavelength vs. Applied Mass relationship can be found in Fig.41.5 below:

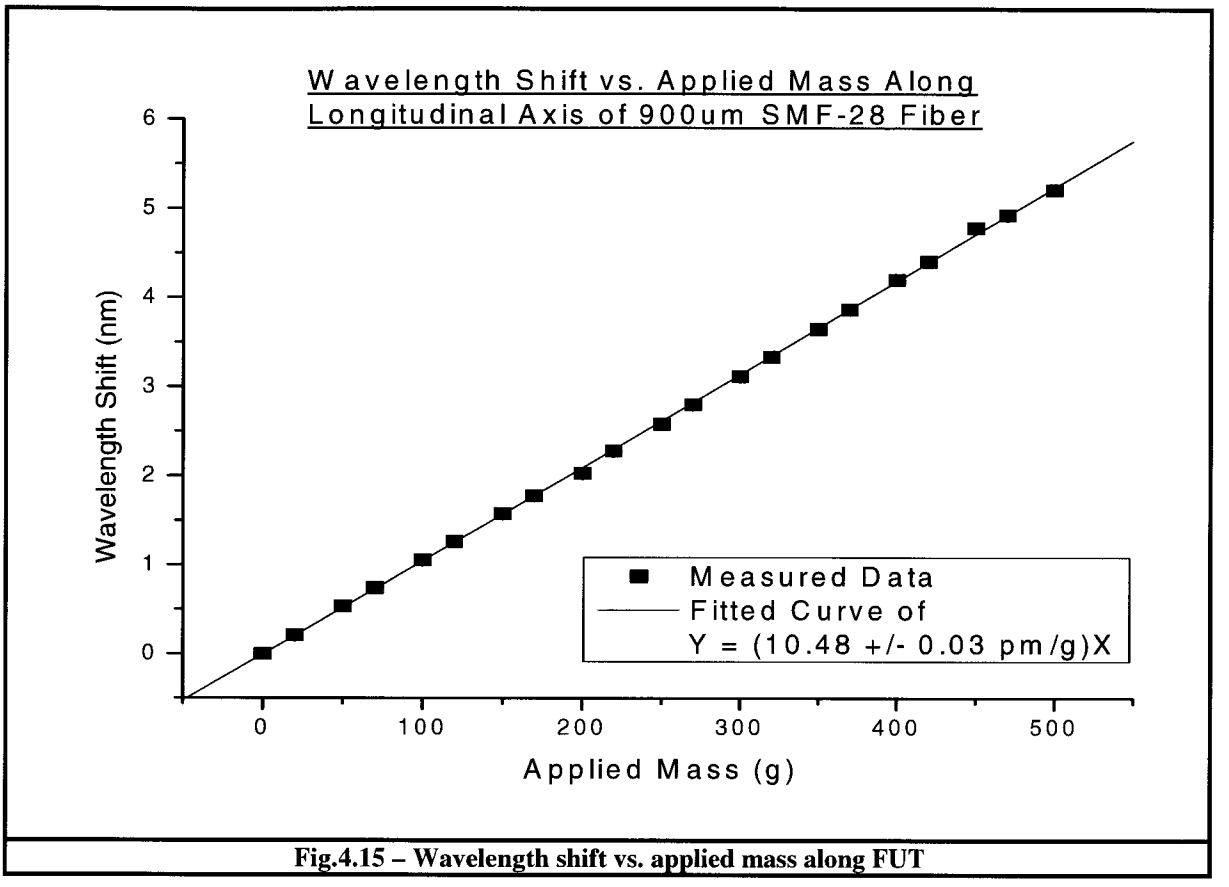

Fig.4.15 – Wavelength shift vs. applied mass along FUT

Thus with the differential quadrature setup and ESS algorithm the wavelength shift for the 900μm SMF-28 fiber was found to be 10.48 ± 0.03 pm/g or 1069.39 ± 3.06 pm/N.

4.5 Preliminary Torsional Stress/Twisting Measurements using the PD OFDR Setup and the Classical Analysis Algorithm

The results presented in this section were my preliminary measurements I carried out to show that I could actually detect torsional stress on the fiber with the polarization diverse OFDR setup with the unmodified 'classical' analysis. The layout with the FUT is similar to that in §4.3 with a 50g weight hanging from the fiber. I then measured the wavelength shift

with respect to position as I twisted the hanging portion of the fiber. The results of this are seen below:

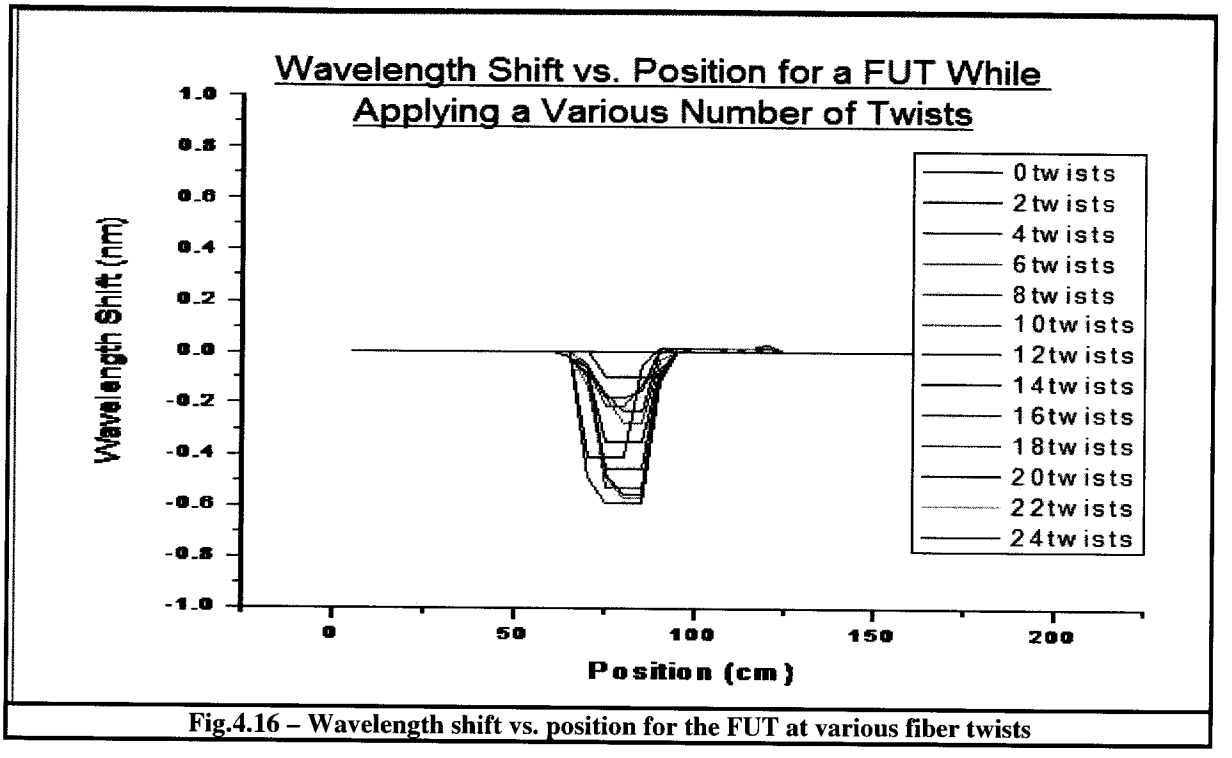

Fig.4.16 – Wavelength shift vs. position for the FUT at various fiber twists

From this graph the wavelength shift with respect to the number of twists can be seen below:

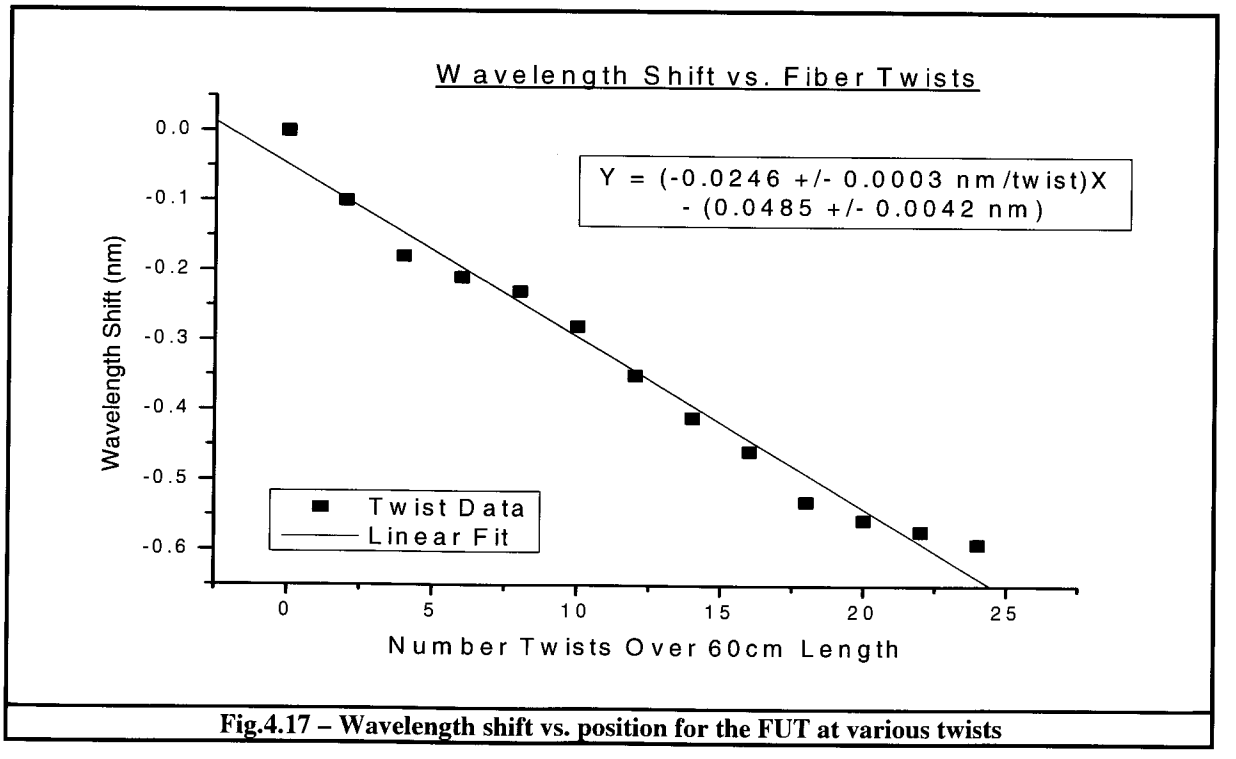

Fig.4.17 – Wavelength shift vs. position for the FUT at various twists

Thus, as is seen above for the 900μm SMF-28 fiber, the wavelength shift experienced by twisting of the fiber is -24.6 ± 0.3 pm/(twist·m). Since the differential quadrature using the same FUT setup in §4.4 performed similar to the polarization diverse setup achieving and relationship of -25.01 ± 0.08 pm/(twist·m) I shall not cover it in detail here. The negative wavelength shift shows that the FUT is physically being compressed as opposed to stretched.

Finally, I should mention other papers that have presented similar results. With regards to doing the temperature sensing, researchers from *Luna Technologies Inc.* wrote several distributed temperature sensing papers [18, 31, 34] using the setup shown in Fig. 2.11. With regards to doing the strain measurement, in 1998 Froggatt wrote an article [29] using a variant of the basic setup but combined the signals from the reference arm and measurement arms of the interferometer in the electrical domain instead of the optical domain. In 2006, Soller *et al.* presented a conference paper [32] where again they used the setup in Fig.2.11 to demonstrate that fiber twisting can be in fact measured using their setup but they didn't go in much detail of their results.

Chapter 5

Fiber Bragg Gratings and In-situ Temperature Monitoring of Fuel Cells

This chapter shall discuss using FBG's as the FUT and how they compare to the SMF-28e fiber as discussed in the previous chapters. I will also discuss my research collaboration with the NRC-IFCI (Institute for Fuel Cell Innovation) in Vancouver, where we did in-situ mapping of the temperature distribution inside a PEM (proton exchange

membrane) fuel cell using both FBG's as well as regular fibers. In the following sections I shall present extra temperature results using both linear as well as chirped FBG's.

5.1 Theory of Fibre Bragg Gratings

Fibre Bragg Gratings (FBG) are in-fiber dielectric mirrors for specific wavelengths. They can be written into SMF-28, multimode or other specialty fibers by using either two-beam interference, photomasking or point-by-point shots from UV laser sources that can cause a periodic change in the index of refraction in the core of the fiber.

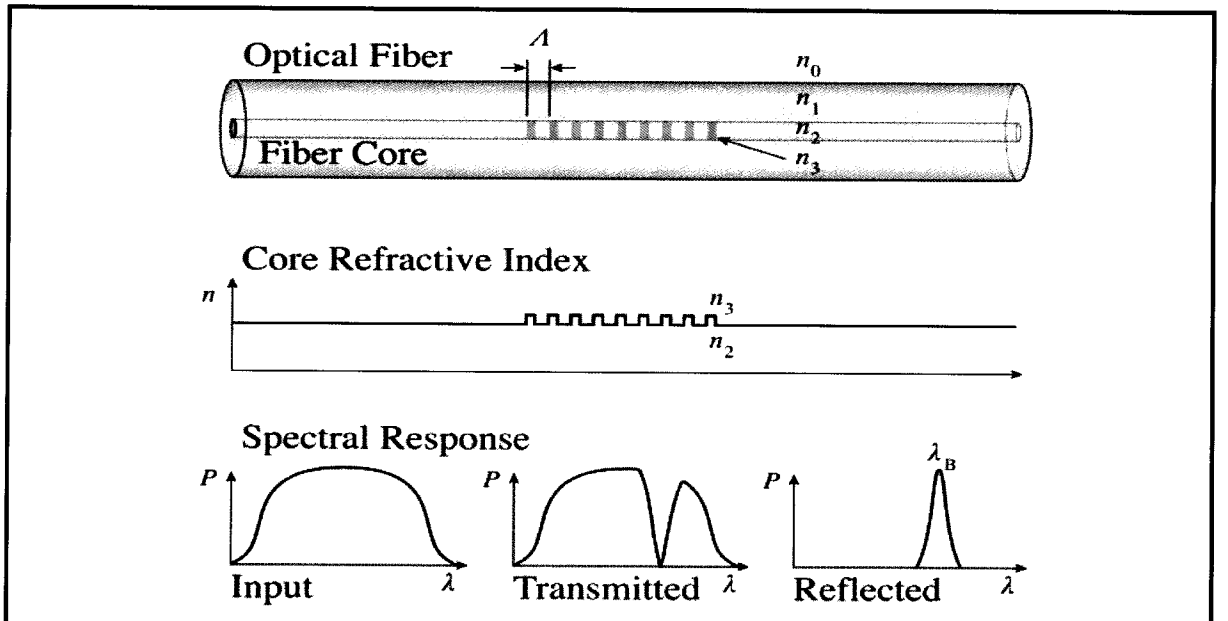

Fig.5.1 – Illustration of a linear FBG, its index of refraction profile in the core, and spectral response

A typical reflection profile for an FBG can be seen in Fig. 5.2 on the following page. In general a grating has a sinusoidal varying refractive index over a defined length. The central reflected wavelength is defined by the relationship, $\lambda_B = 2n\Lambda$, where n is the *effective refractive index* of the grating in the core defined by: $n = (n_3 + n_2)/2$, and Λ is the period of the grating. The bandwidth of the grating $\Delta\lambda$ is given by the relation below[38]:

$$\Delta\lambda = \left[\frac{2\delta n_0 \eta}{\pi}\right]\lambda_B \,, \tag{5.1}$$

where δn_0 is the variation in the refractive index $(n_3 - n_2)$ while η is the fraction of power in the core.

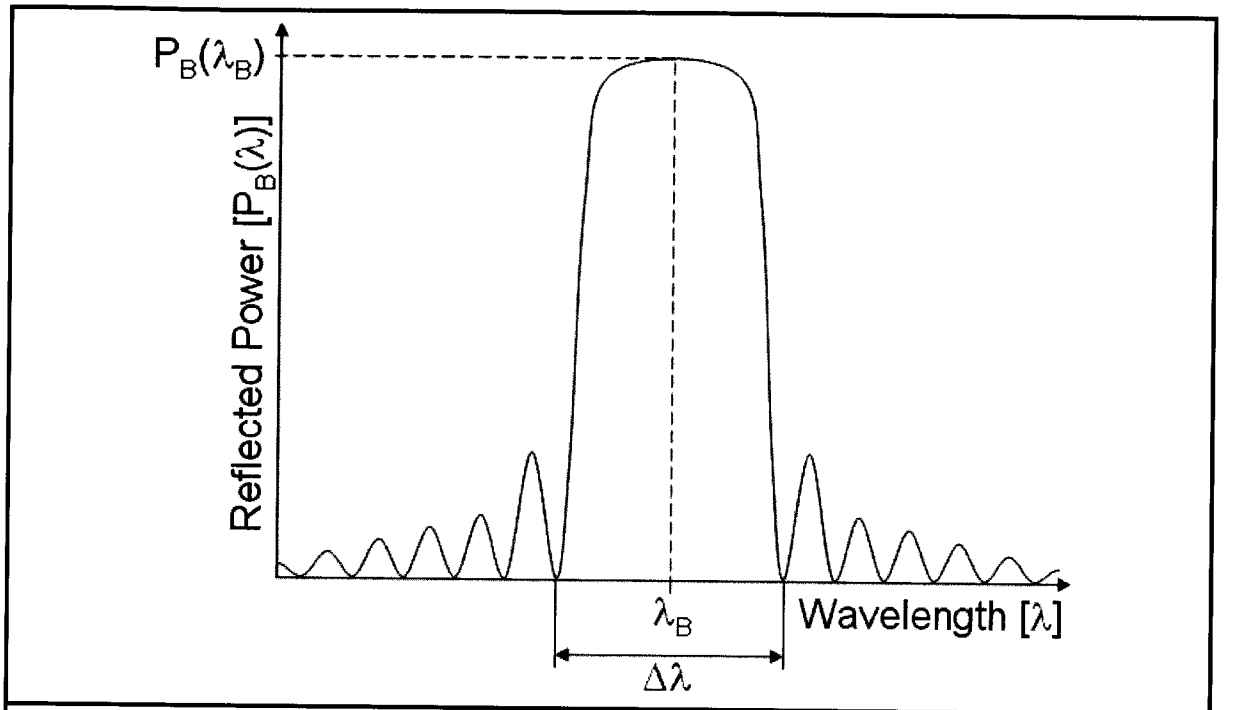

Fig.5.2 – Reflection profile with respect to wavelength for a typical grating

The peak reflected power $P_B(\lambda)$ is given by the following relation[38]:

$$P_B(\lambda) = \frac{\sinh^2\left[\eta(V)\delta n_0\sqrt{1-\Gamma^2}N\Lambda/\lambda\right]}{\cosh^2\left[\eta(V)\delta n_0\sqrt{1-\Gamma^2}N\Lambda/\lambda\right]-\Gamma^2}, \tag{5.2}$$

where,

$$\Gamma(\lambda) = \frac{1}{\eta(V)\delta n_0}\left[\frac{\lambda}{\lambda_B}-1\right]. \tag{5.3}$$

For small Γ this can also be approximately expressed as:

$$P_B(\lambda) \approx \tanh^2\left[\frac{N\eta(V)\delta n_0}{n}\right]. \tag{5.4}$$

The two types of FBG's that I present throughout this chapter are linear gratings and chirped gratings. Diagrams of these can be seen in Fig. 5.3.

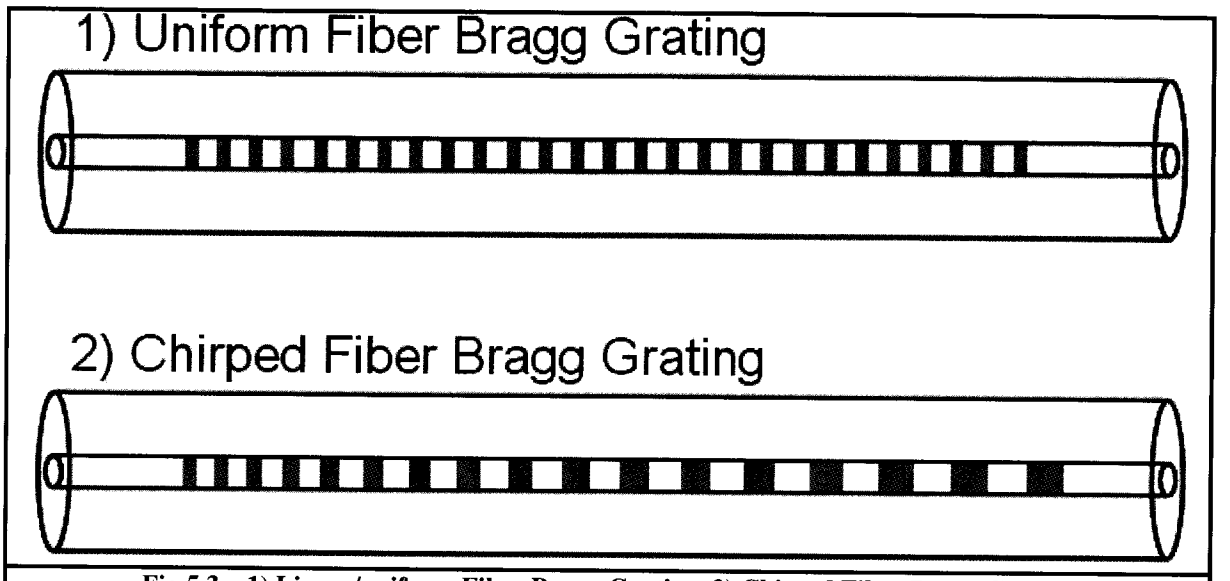

Fig.5.3 – 1) Linear/uniform Fiber Bragg Grating, 2) Chirped Fiber Bragg Grating

The linear FBG has a constant grating period Λ along its length so λ_B also remains constant. On the other hand for the chirped FBG the grating period Λ increases linearly or decreases linearly with respect to distance. This causes the λ_B to also shift linearly throughout the grating. Based on these characteristics the linear grating's main application is to serve as an optical filter, reflecting light of wavelength approximately $\lambda_B \pm \Delta\lambda/2$, while allowing the wavelengths of light outside this range to transmit through. Since λ_B varies linearly with respect to position, one of the primary applications for the chirped grating though is to serve as a dispersion compensation medium which can expand or compress optical pulses[39].

5.2 In-situ Mapping of Temperature Distribution Inside a PEM Fuel Cell

5.2.1 Theory of Hydrogen Fuel Cell Operation

This subsection presents the general chemical processes involved in hydrogen fuel cells. There are two main electrochemical reactions which occur in a fuel cell. One at the anode plate and the other at the cathode plate.

At the anode plate, we have the following reaction:

$$H_2 \leftrightarrow 2H^+ + 2e^- \ , \tag{5.5}$$

while at the cathode plate we have this reaction:

$$2H^+ + \frac{1}{2}O_2 + 2e^- \leftrightarrow H_2O \ . \tag{5.6}$$

These combine to give the result:

$$H_2 + \frac{1}{2}O_2 \leftrightarrow H_2O \ . \tag{5.7}$$

In other words, at the anode hydrogen molecules (H_2) separate to form the positively charged ions (H^+) and electrons. Instead of recombining the electrons get attracted to the reaction happening over at the cathode. In between the 2 flush plates is a proton exchange membrane that allows protons (ionized hydrogen from the anode) to pass through but it will not allow the regular hydrogen or oxygen molecules to pass through. On the cathode side it now has the hydrogen ions and it has the oxygen but it still needs the two electrons to create the water molecule. The electrons from the anode have a difficult time to pass the PEM (Proton Exchange Membrane) and water molecules that have already been created on the cathode side so the path of least resistance is to actually travel through the graphite plate (or other metals can be used), through a wire and over to the other plate – in turn allowing the water molecule to be created – but in the process also creating an electrical current of 2 electrons for every oxygen atom.

The PEM is the main component that is placed in a planar MEA (Membrane Electrode Assembly – aka catalyst layer) that is placed between the two parallel (and mirror imaged) anode and cathode plates that typically have machined channels that are on the face of the plate with serpentine, parallel, series, or series-parallel geometries. As mentioned, for

this project the prototype plates were made of graphite with the flow through channels machined into them via a mill. Hydrogen is injected into the anode plate and oxygen into the cathode plate with the MEA in between the two. The only portion of the MEA surface area that produces power is where the reactive gases touch the electrode assembly on both sides. Where this happens water is created which allows easier transport for the hydrogen ions through the membrane but not for the electrons. Thus there is a net positive and negative potential between the two plates which allows for electron/current collection. This is illustrated in Fig.5.4[41].

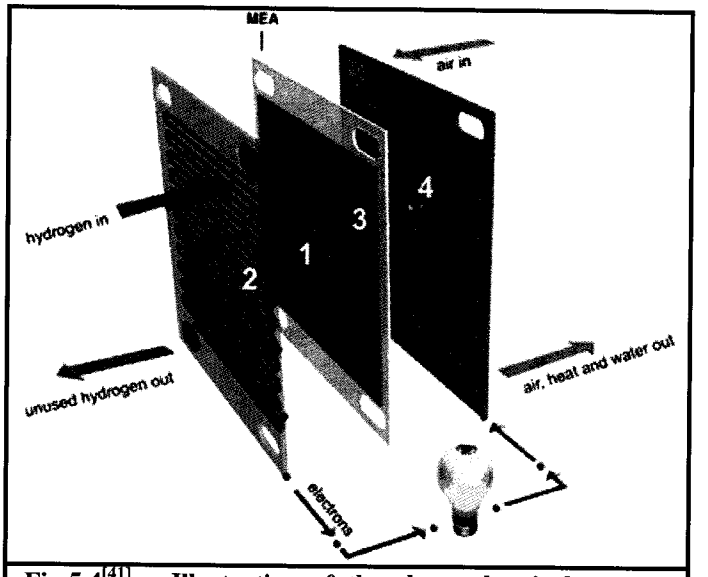

Fig.5.4[41] – Illustration of the electrochemical process with a PEM style hydrogen fuel cell

5.2.2 Details Regarding the Prototype Low Temperature PEM Fuel Cell

The basic layout for the prototype fuel cell that I was to work with is shown in Fig.5.5 below:

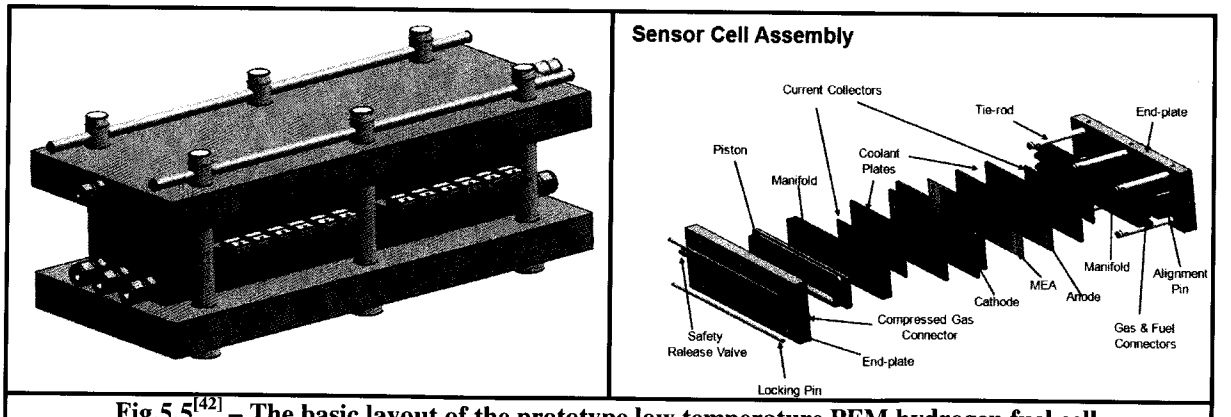

Fig.5.5[42] – The basic layout of the prototype low temperature PEM hydrogen fuel cell.

As was described in the previous section, the MEA/PEM is in the centre of the fuel cell being sandwiched by the anode and cathode plates, then the coolant plates, current collectors, input gas manifolds to distribute the oxygen and hydrogen and finally the piston/endplates to keep all the other components together under pressure.

The problem NRC-IFCI had with the prototype is that the measured efficiency while running the cell was much lower than what their simulations predicted. One possible cause was a non-uniform temperature gradient within the cell while operating which could in turn lower the efficiency. To test this hypothesis the NRC-IFCI wanted to do in-situ temperature monitoring in and around the cathode plate. As well, they wanted to compare the current generation ratios throughout the cathode plate to see if there was any correlation between the temperature of that section as well as the amount of current generated. To do this they redesigned a cathode plate (and mirrored anode plate) that was divided into 18 sections (3 x 6) that were electrically isolated from one another. On the back of the cathode plate they installed thermocouples so that there was one electrical temperature sensor in the center of each section as is seen below[42]:

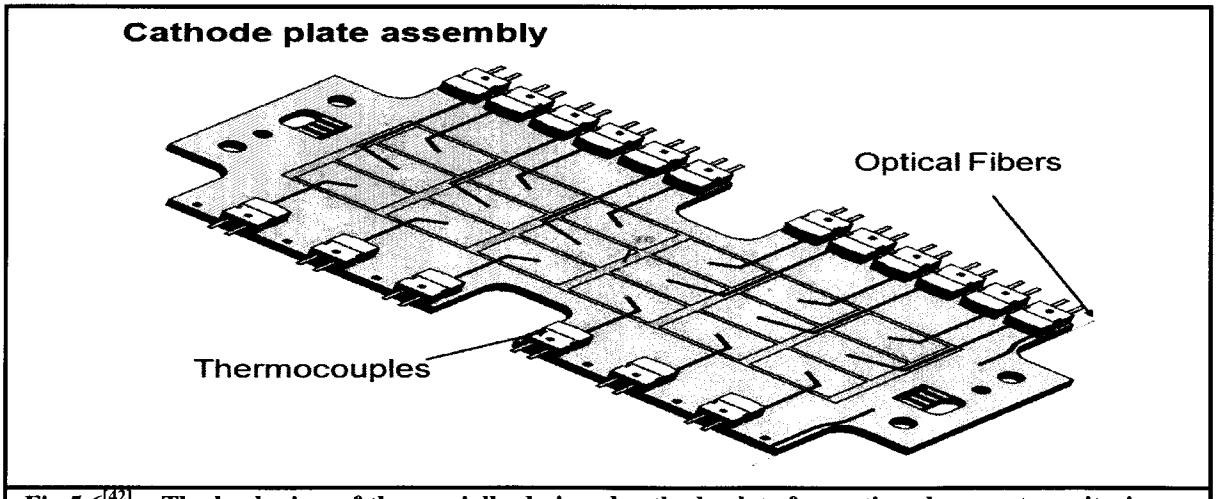

Fig.5.6[42] – The back view of the specially designed cathode plate for sectioned current monitoring as well as in-situ temperature monitoring.

On the other side where the thermocouple sensor was passed through a small hole in each of the 18 sections there was also regular SMF-28 fiber embedded along with 3 identical FBG arrays that contains 6 FBG's in series where each is 4cm in length. The reflection spectrum for one of these FBG arrays is seen in Fig.5.7.

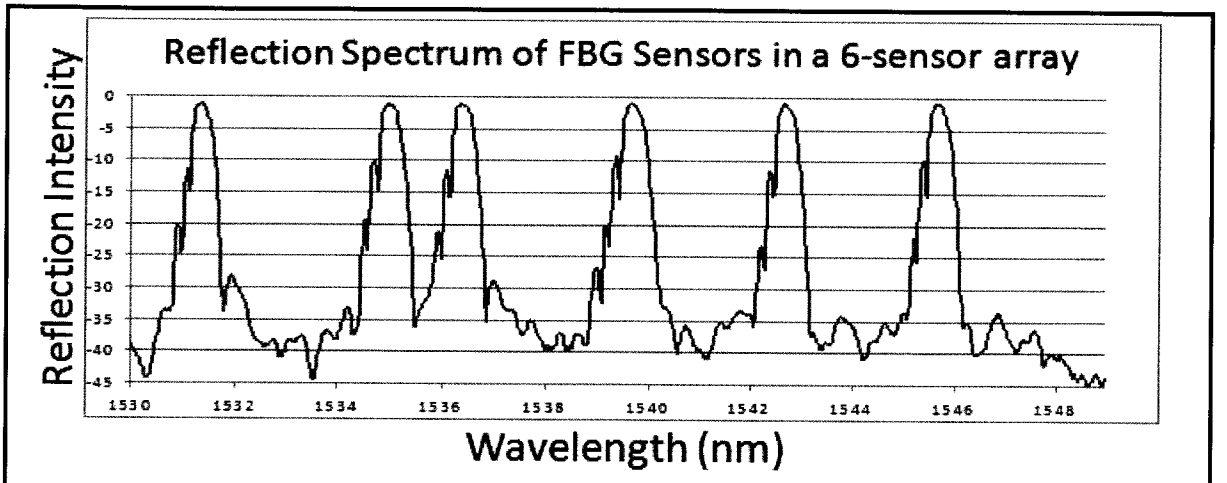

Fig.5.7[42] – Reflection spectrum of the 6 FBG sensor array

Thus there was one 4cm FBG sensor for each 4cm segment of the cathode plate. Along side of it ran a long piece of standard SMF-28 fiber and one thermocouple in the center of each segment. In all, there were 3 different types of sensors being used to monitor the in-situ temperature. If the FBG's and/or SMF-28 performed as well as the thermocouples, then they would remove the thermocouples, since for 18 thermocouples it meant 18 extra sets of wires coming out of the fuel cell; whereas for the FBG's or SMF-28 fiber only one optical fiber would come out of the fuel cell to monitor the whole cathode plate.

5.2.3 Details Regarding the OFDR Setup I Built for the NRC-IFCI Project

When out at their facility in Vancouver I had to rebuild an OFDR setup to interrogate the FBG's and SMF-28 FUT's that were to go in the prototype fuel cell. The version that I

built for them is the polarization diverse OFDR setup that I described in §2.5.2. The laser used in the setup is the Thorlabs TXP-ECL5000D that I detailed in Fig.2.2 and 2.3.

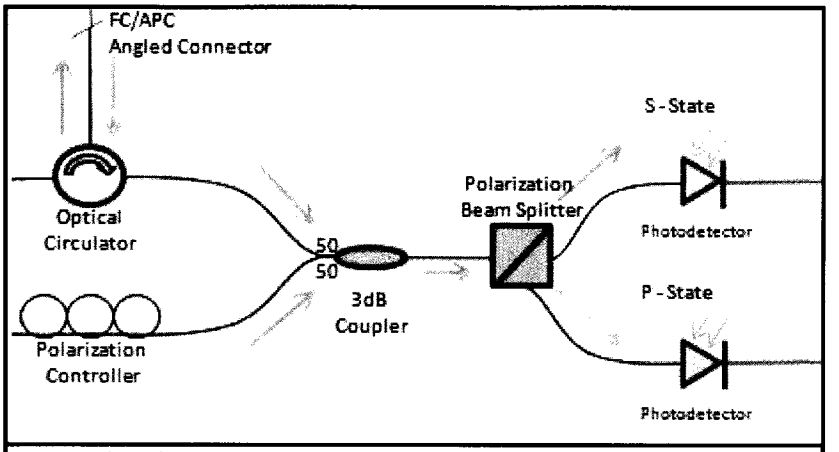

Fig.5.8 – Polarization Diverse OFDR measurement setup.

The initial coupler used to split the signals to the measurement interferometer and the auxiliary interferometer was a ratio of 90/10 instead of 99/1 mentioned in the previous versions described in Ch.2. Like the others the measurement interferometer split its reference arm from the measurement arm by the tunable directional coupler described in §2.4. The photodetectors used for to measure the S & P-states of the measurement interferometer as well as the beating (external clock) signal of the auxiliary interferometer were the Thorlabs FPD510 described in Table 2.2. The voltage amplifiers used for the two measurement signals are the Femto HVA-10M-60-B amplifiers described in §2.2.4 while the amplifier details for the external clock is provided in §2.2.3. As was the case with the other setups the PCI-6115 DAQ-card was used to collect the measurement data.

5.2.4 Preliminary Temperature Results

Unfortunately when my research contract had ended they still didn't have the prototype fuel cell completed for me to try out so none of the results presented here will be those from the actual running fuel cell. What I did though was take one of the 3 identical FBG arrays (the spectral profile of which is seen in Fig.5.7) and mounted each individual 4cm FBG inside of individual 3.5cm heating units with built in thermocouples. The resolution of the electronic

readout for the thermocouples was 0.5°C. The accepted wavelength shift to temperature constant for FBG's phase masked into SMF-28 fibre is 10pm/°C[40]. Using this, and the 75.6pm·cm resolution limitation that I discussed in §3.1 – since the FBG's were 4cm in size it meant that the frequency resolution for that sized segment dropped down to 18.9pm ≈ 1.89°C for the FBG. To get down around the resolution of the thermocouple, it was during this period that I first developed the Fourier Interpolation Algorithm (FIA) discussed in §3.3. Using an interpolation factor of $n = 10$, I was able to drop the frequency resolution for the 4cm grating from 18.9pm down to 1.89pm ≈ 0.19°C which was on par with the thermocouples. Taking a few readings from both the digital thermocouple as well as from the OFDR setup whereby I issued the room temperature at the time of 22.0°C to turn the relative temperature measurements coming from the FBG into absolute temperature measurements. The results of the two are shown in Table 5.1. As you can see the values for both are equivalent to within their resolution limitations, the one down side though is that the thermocouple was able to update about every second where as the readings coming from the OFDR setup were about every 4 seconds.

Table 5.1 – Comparison between a digital thermocouple and 4cm FBG using the PD OFDR setup using the FIA algorithm and interpolation factor of *n=10*.

Measurement #	Thermocouple (°C)	TC resolution	FBG/OFDR	FBG resolution
1	22.0	± 0.25	22.0	± 0.1
2	28.5	± 0.25	28.4	± 0.1
3	37.0	± 0.25	36.8	± 0.1
4	49.0	± 0.25	49.0	± 0.1
5	58.5	± 0.25	58.2	± 0.1
6	70.0	± 0.25	69.8	± 0.1
7	84.5	± 0.25	84.4	± 0.1
8	91.0	± 0.25	90.8	± 0.1

To try to test out the SMF-28 in a semi-real environment the members at the IFCI made a mock-up fuel cell for me where the fiber winds in and out of the cell 3 times over

distance within the cell of 12.6cm. An image of this mock-up cell can be seen in Fig.5.9 while the backscatter profile for the cell can be seen in Fig.5.10 below:

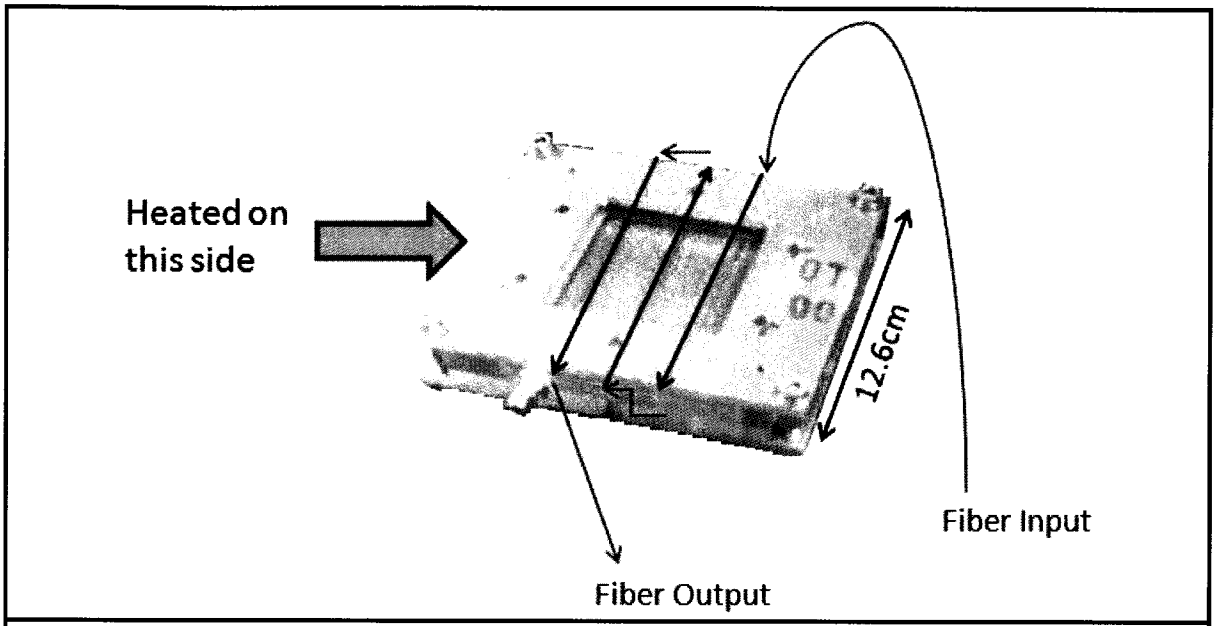

Fig.5.9 – FUT layout for the mock-up fuel cell

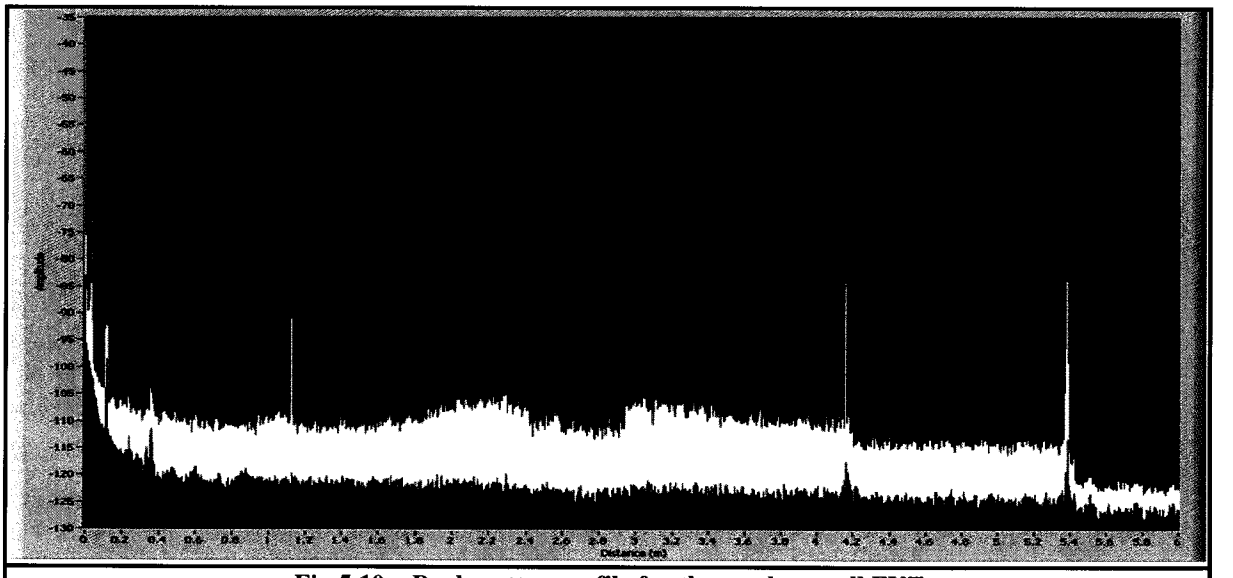

Fig.5.10 – Backscatter profile for the mock-up cell FUT

One side of the cell was then heated using a hotplate. At different times the wavelength shift was measured with respect to position. These results can be seen in Fig.5.11 on the following page. At the fourth temperature measurement I also checked it with a

thermocouple that measured 86.1°C which is what the OFDR setup was also measuring to within error.

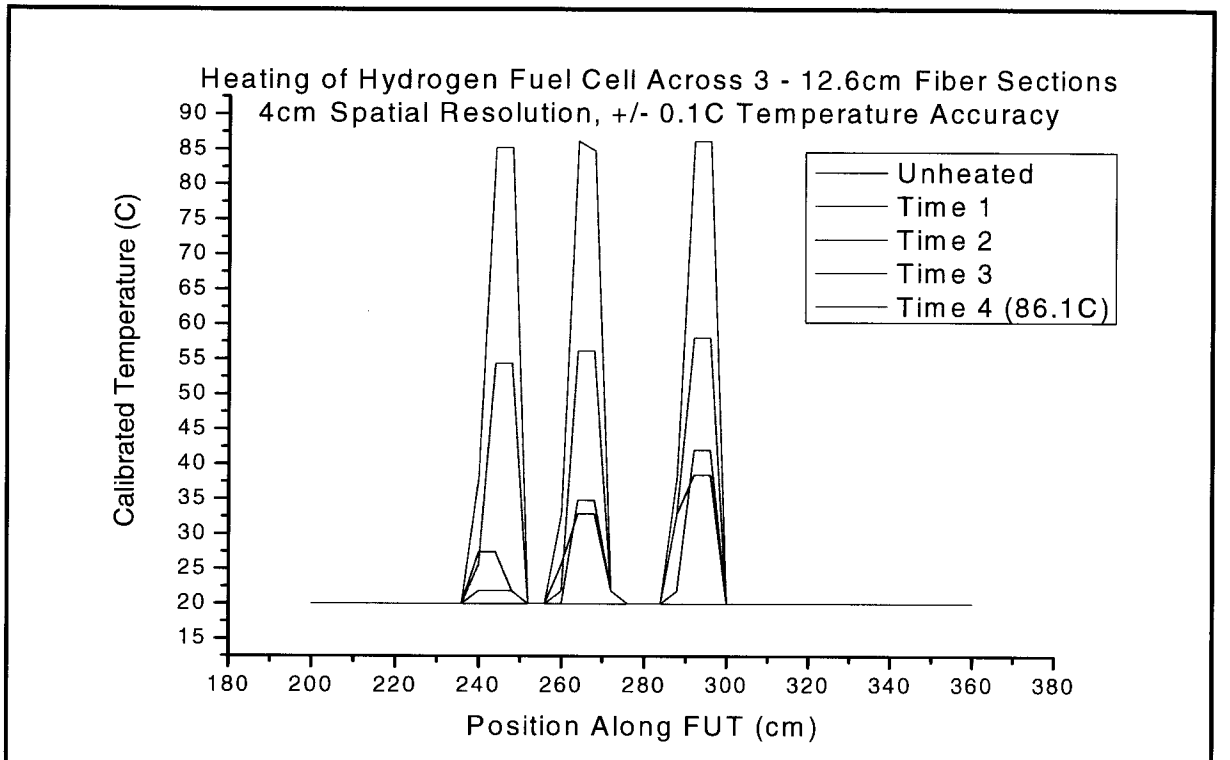

Fig.5.11 – Reflection spectrum of the 6 FBG sensor array

5.3 Sensing Using Identical Linear Gratings in a Parallel Network

As was mentioned in §5.2, the NRC group had gotten 3 identical FBG arrays of 6, 4cm gratings in each fabricated. I explained that if they wanted to splice these 3 arrays together in series and embed within the fuel cell that the first array would work but that very little of the λ_B wavelength light would reach the other two arrays and they would be essentially useless for sensing purposes. One other alternative I gave them was to get a 1x3 coupler and splice one of the FBG arrays to each of the 3 outputs of the coupler with a time delay added on each to create a OTDM (optical time division multiplexing) effect by running the gratings in parallel instead of series. The coupler hadn't arrived before I left but I shall demonstrate the proof of principle. In Fig.5.12 is a diagram of the FUT.

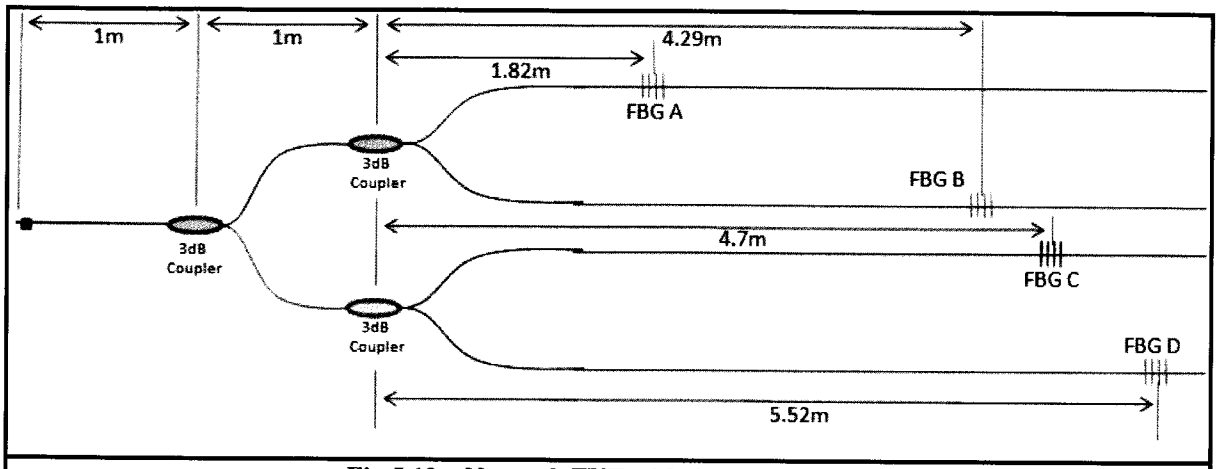

Fig.5.12 – Network FUT with 4 parallel FBG's

The FUT is comprised of a 1x2 50/50 (3dB) coupler whereby their outputs are in turn also each spliced on to 1x2 50/50 couplers. The four output then are spliced on to pieces of SMF-28 fiber that contain linear FBG's, each of which is a different length from the coupler as is seen in Fig.5.12. The central wavelengths λ_B of the gratings A, B, C and D are: 1559.33nm, 1559.16nm, 1560.02nm and 1559.93nm respectively. The amplitude of the raw beating data from a 1556 to 1564nm can be seen below:

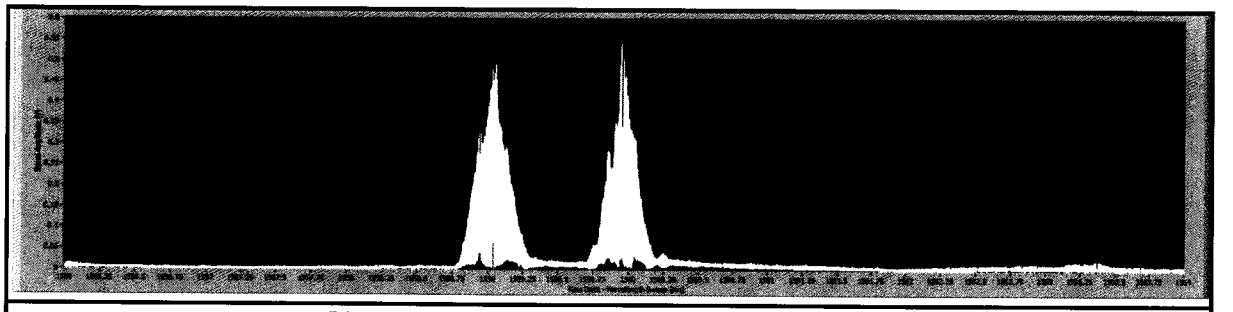

Fig.5.13 – Amplitude of raw data of network FUT

As you can see it only looks like 2 FBG's. This is because FBG's A & B have a closely matching central wavelength so overlap, the same holds true for FBG's C & D. The Fourier transform (spatial backscatter/back reflection profile) of this data can be seen in Fig.5.14. Notice that although one cannot differentiate the FBG's in the

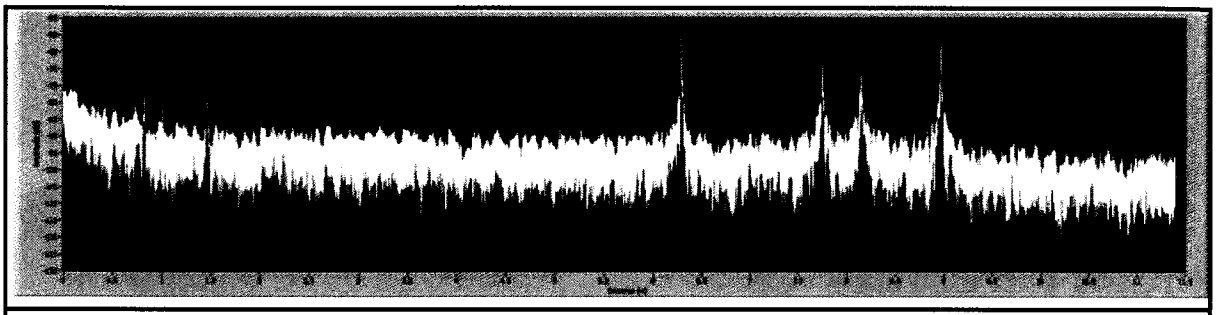

Fig.5.14 – Spatial back reflection profile of the network FUT.

frequency domain, they are easily distinguished in the spatial domain. By extracting the subset of spatial data around each FBG individually one can actually retrieve both the reflectivity

and group delay for each FBG as well as any wavelength shifts they might exhibit with receiving any stimuli such as temperature changes. When the subset is inverse Fourier transformed, using two channel data acquisition systems such as the polarization diverse setup or the quadrature interferometer setup then the complex data sets in the frequency domain can be treated as $i_A(\omega)$ and $i_B(\omega)$. The reflectivity then can be expressed by the following equation[19]:

$$r(\omega) = \sqrt{\left|i_A(\omega)\right|^2 + \left|i_B(\omega)\right|^2} \quad , \tag{5.8}$$

while the group delay is expressed as:

$$\tau_g = \frac{\angle\left\{i_A(\omega) i_A{}^*(\omega+\Delta\omega) + i_B(\omega) i_B{}^*(\omega+\Delta\omega)\right\}}{\Delta\omega} \quad , \tag{5.9}$$

where $\angle\{u\}$ denotes the phase of the complex data set u. Figures 5.15(a)-(d) show the reflectivities and group delays for the four FBG's. The gratings A and C were then heated, the shifting of their reflectivity profiles with respect to wavelength at different temperatures are shown in Fig.5.16(a) and Fig.5.16(b). Finally, the wavelength shift with respect to temperature curves for these two gratings are shown in Fig.5.17(a) and Fig.5.17(b).

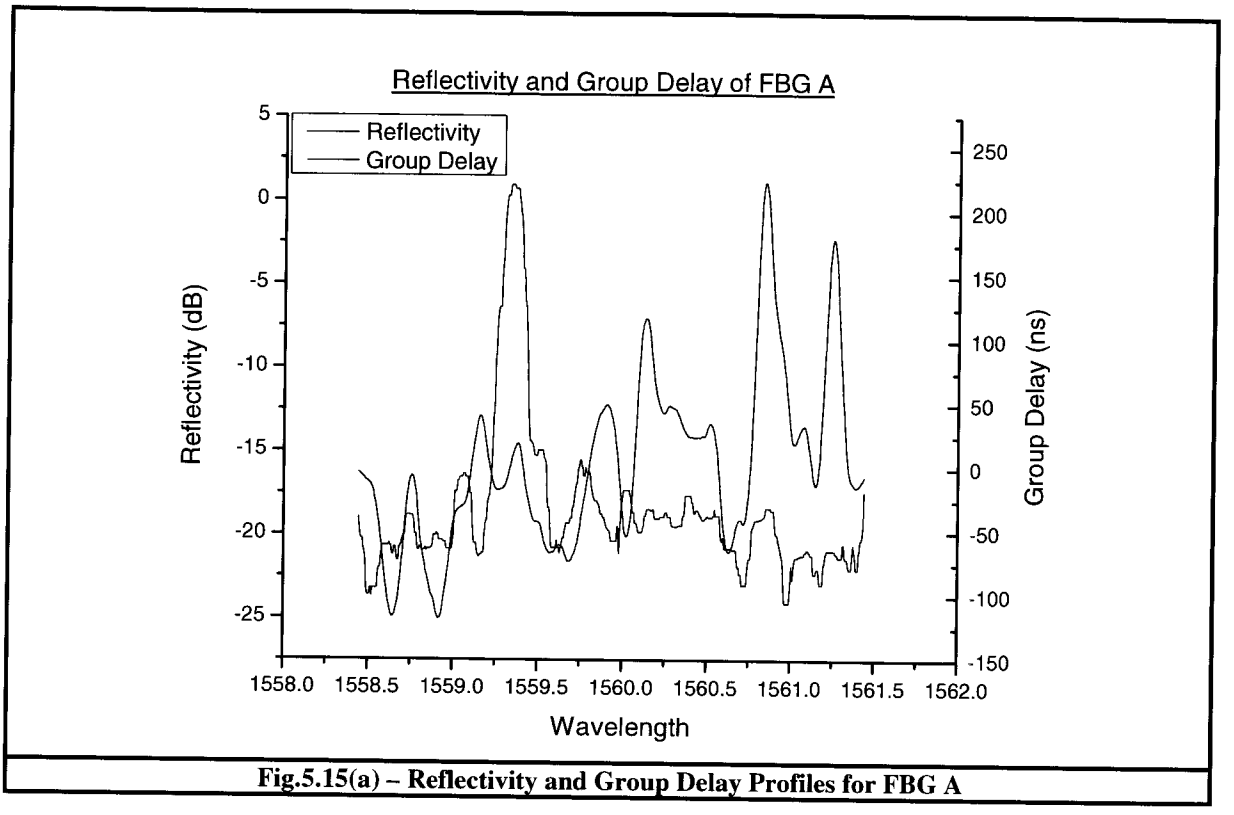

Fig.5.15(a) – Reflectivity and Group Delay Profiles for FBG A

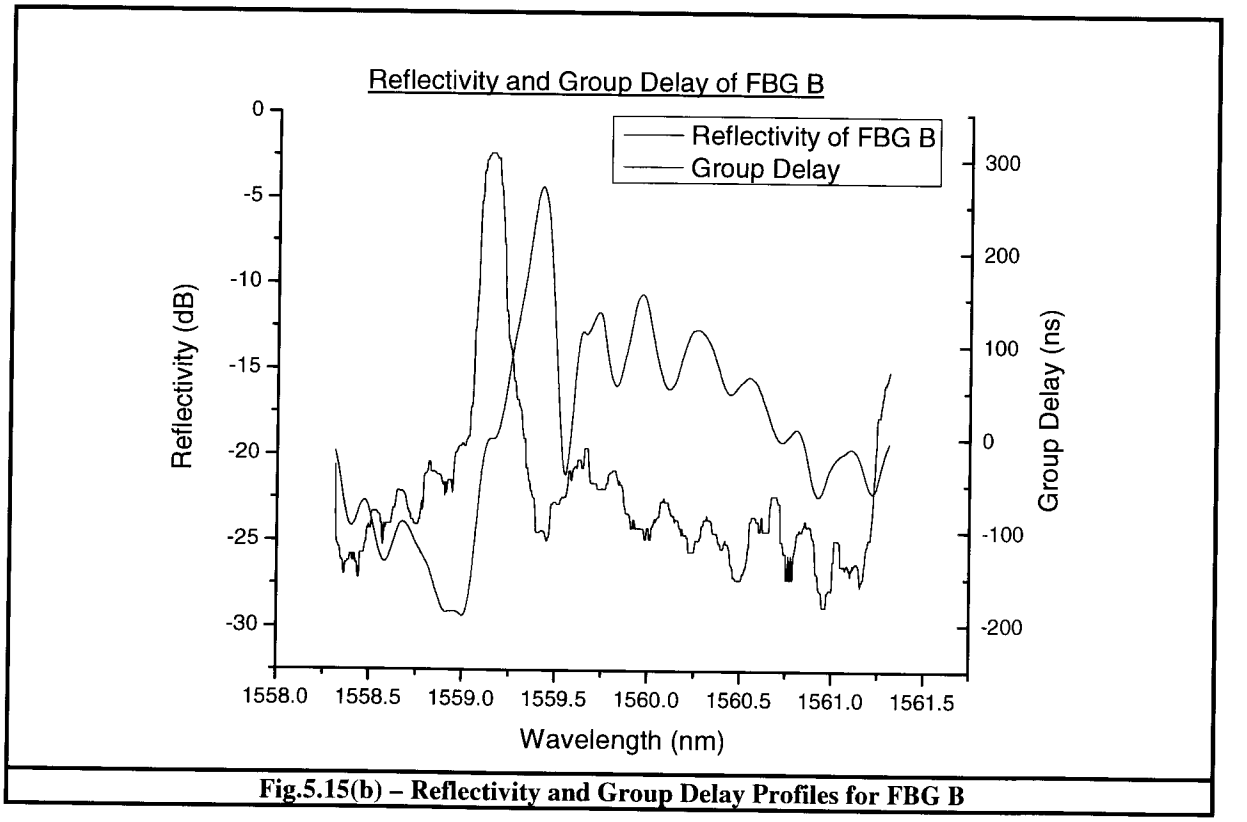

Fig.5.15(b) – Reflectivity and Group Delay Profiles for FBG B

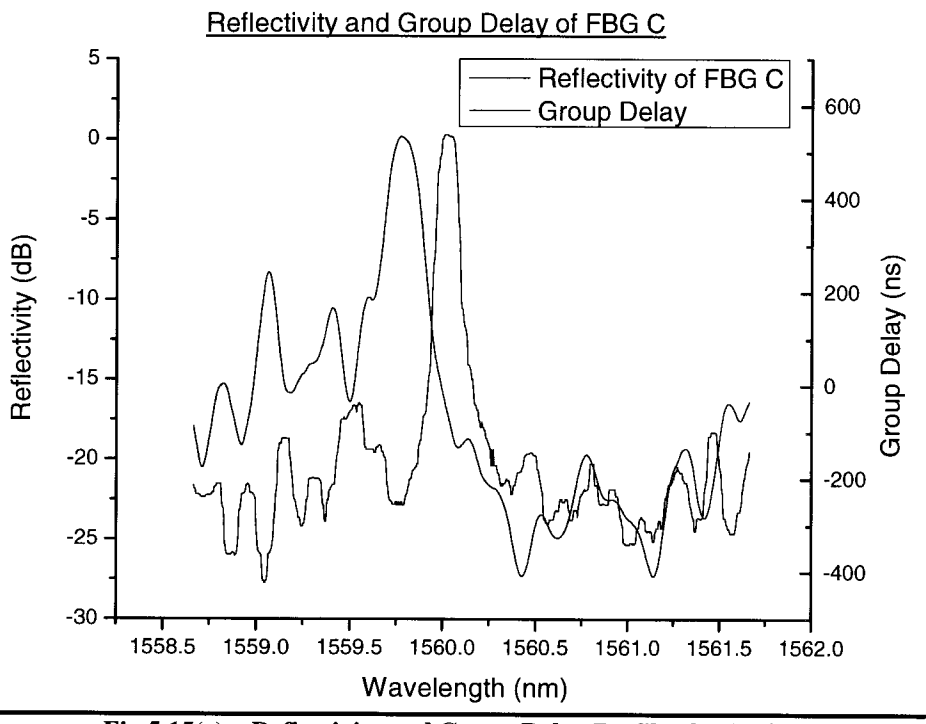

Fig.5.15(c) – Reflectivity and Group Delay Profiles for FBG C

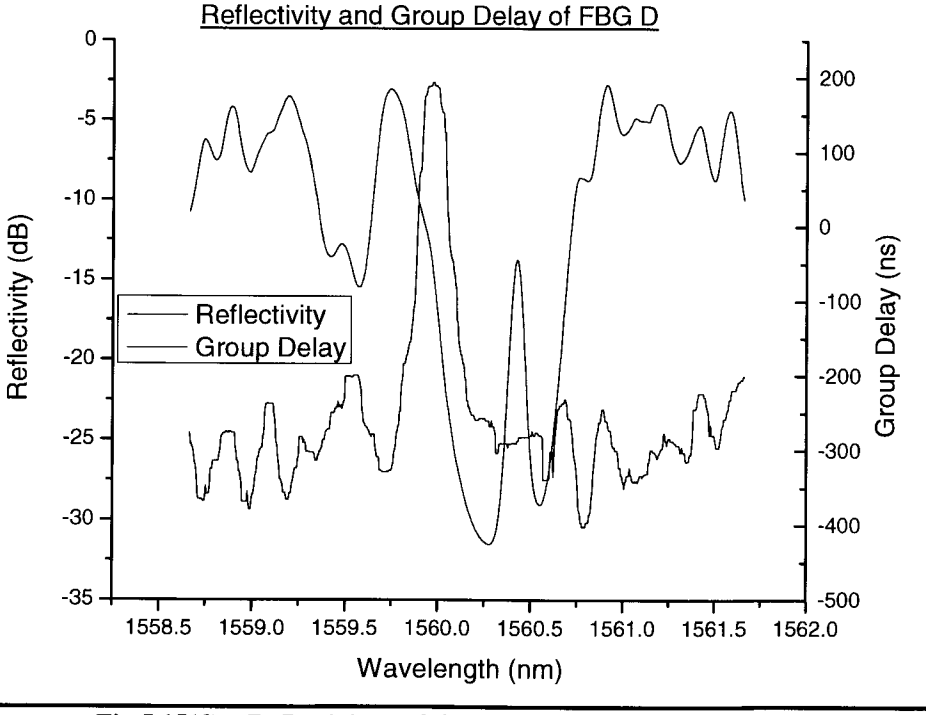

Fig.5.15(d) – Reflectivity and Group Delay Profiles for FBG D

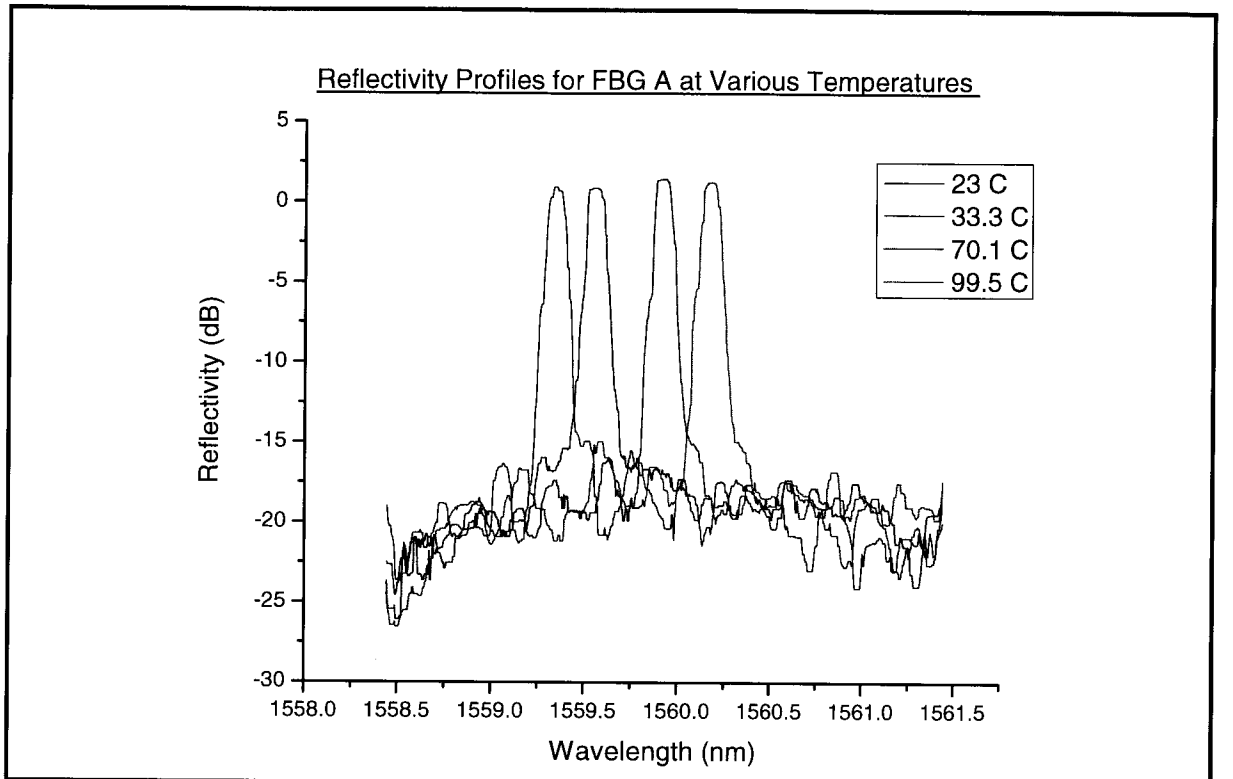

Fig.5.16(a) – Reflectivity Profiles for FBG A at Various Temperatures

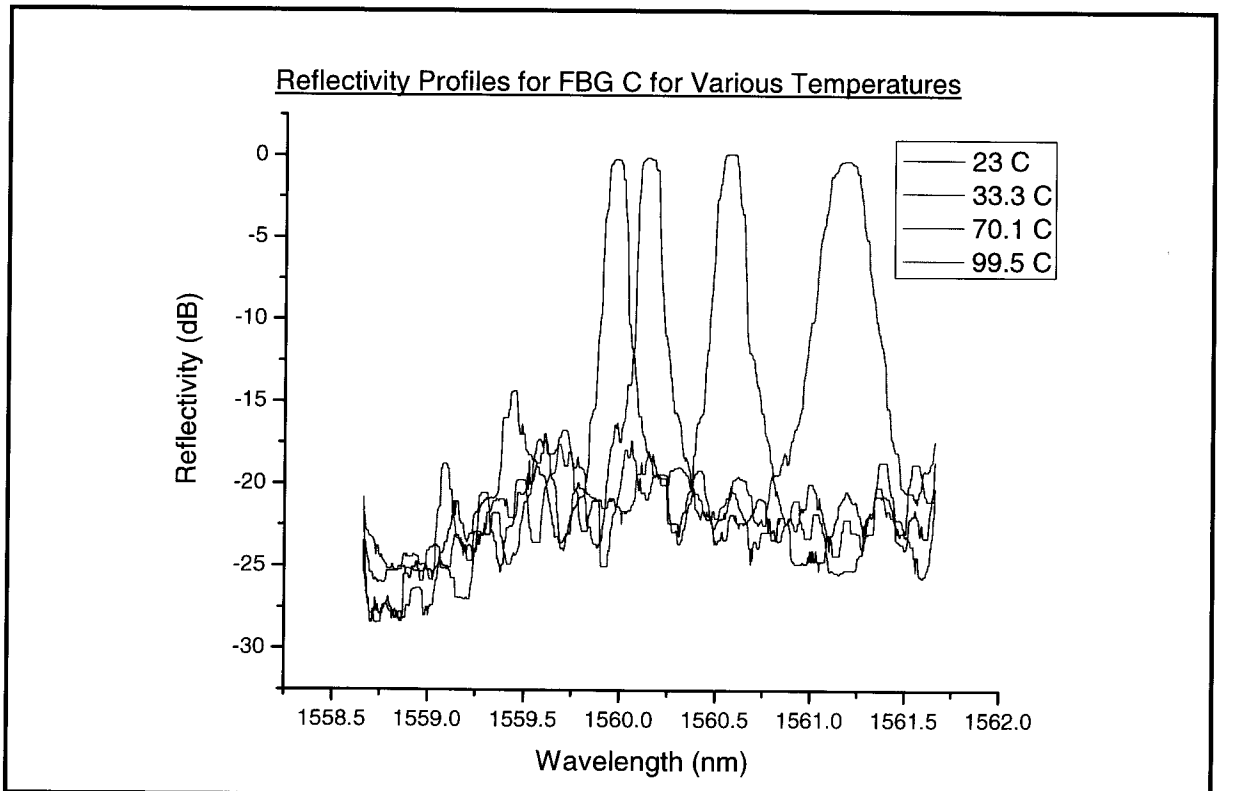

Fig.5.16(b) – Reflectivity Profiles for FBG C at Various Temperatures

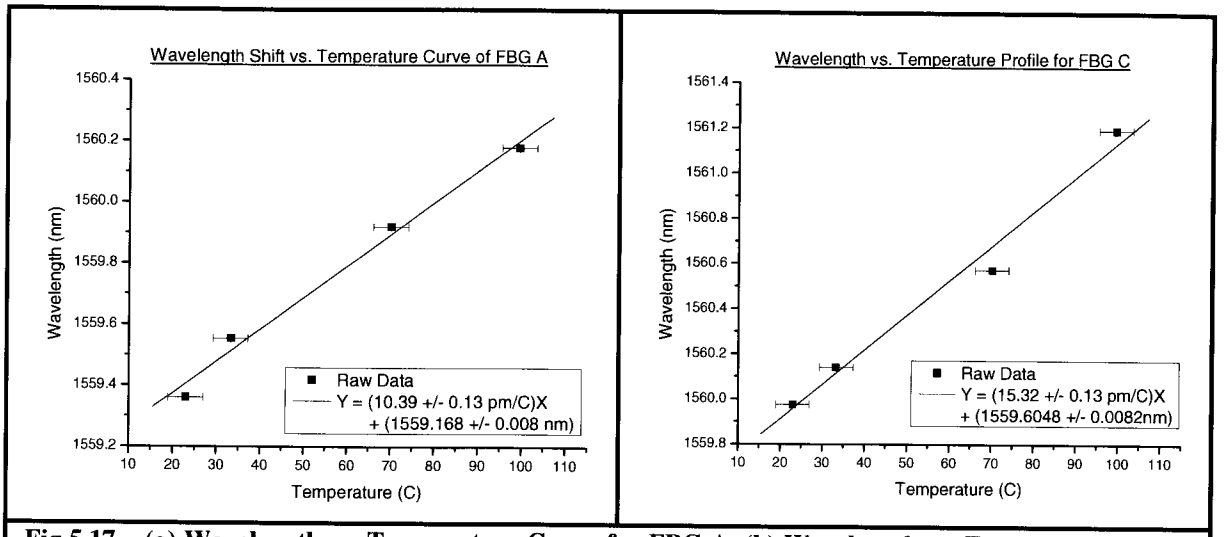

Fig.5.17 – (a) Wavelength vs. Temperature Curve for FBG A, (b) Wavelength vs. Temperature Curve for FBG C

Notice that FBG A has a wavelength shift of 10.39 ± 0.13 pm/°C, while FBG C has a shift of 15.32 ± 0.13 pm/°C. The value for A matches up quite closely to that which has been published elsewhere [40], but the value for FBG C can be possibly partially explained by the way the grating was annealed. Grating A was annealed for 24hrs at 100°C, while grating C was annealed for 8hr at 100°C, then 16hrs at 135°C, and finally 24hrs at 150°C. This different annealing process can have an effect on the expansion coefficient of the glass and in turn how the index of refraction changes with respect to temperature.

A small portion of Ref. [19] written by Soller *et al.* briefly discussed interrogating FBG's using a polarization diverse setup as is shown in Fig.2.11. As well, in a recent conference paper [30] Froggatt, Soller *et al.* also discussed how they used the same Fig.2.11 setup to do stress/strain, and temperature measurements using standard SMF-28 on a parallel network. In their paper they used only one 1x2 coupler with two outputs instead of the 4 outputs that I had demonstrated. As mentioned, this can work as a possible solution for the NRC-IFCI fuel cell in-situ measurements if they are wanting to stay with the 3 identical FBG arrays.

5.4 Distributed Temperature Sensing Using Chirped Gratings

In §5.3 I discussed using linear gratings as temperature sensors when using in conjunction with an OFDR setup. The one problem, although they do measure the temperature quite accurately and do not require any averaging, the linear gratings still behave as point sensors albeit optical sensors that can be strung together both in series if they have different central wavelengths or in parallel if they have the same central wavelength. But since they are still point sensors they are discrete in nature and it means that stimuli events can still be missed if they happen in between two of the gratings. As an alternative I will present a method of using chirped gratings where any portion of the grating is taken to measure the temperature; if long enough then this could also be another distributed solution to doing the in-situ monitoring within the fuel cell.

The chirped grating FUT can be seen in Fig.5.18 below:

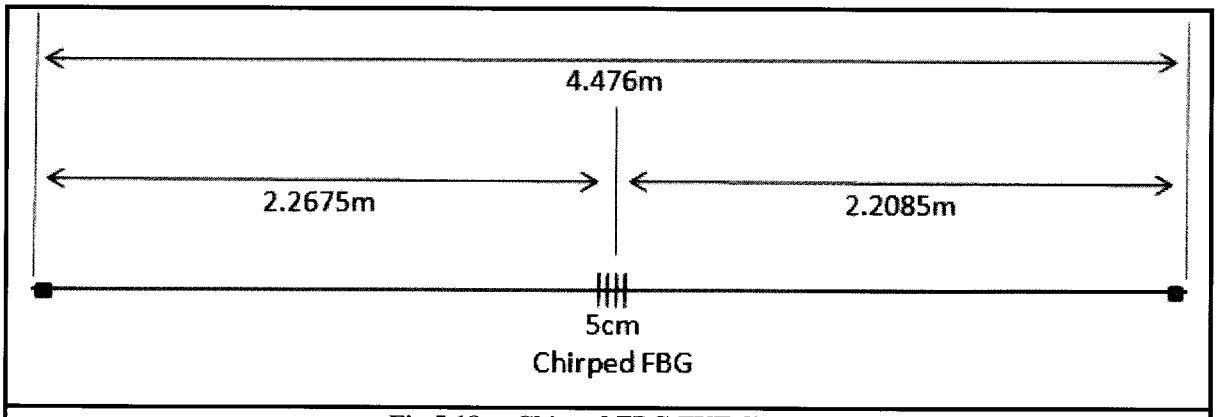

Fig.5.18 – Chirped FBG FUT diagram

If tuning the laser across a 20nm range (1550 – 1570nm) the amplitude of the raw data can be seen in Fig.5.19(a) while the FUT's associated backscatter profile can be seen in Fig.5.19(b). It should be noted that the results seen are from the positive dispersion side of the grating.

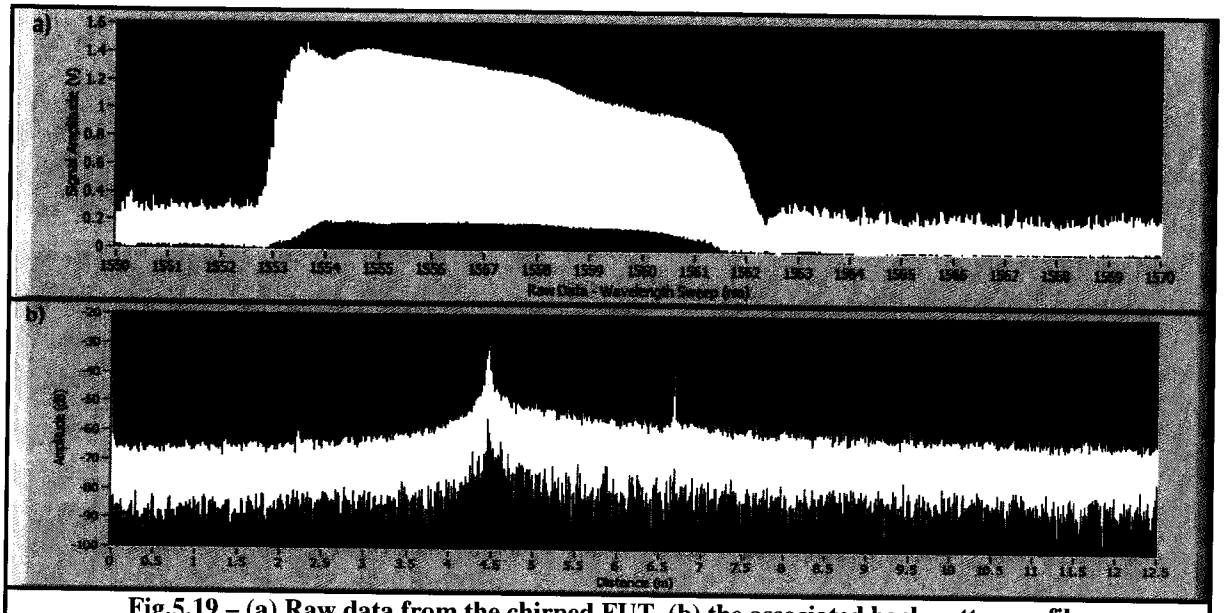

Fig.5.19 – (a) Raw data from the chirped FUT, (b) the associated backscatter profile.

The chirped gratings are 2.5cm in length and are thermally controlled as seen in Fig.5.20. They were used for past research to create tunable gratings for dispersion compensation – more information can be found in reference [39].

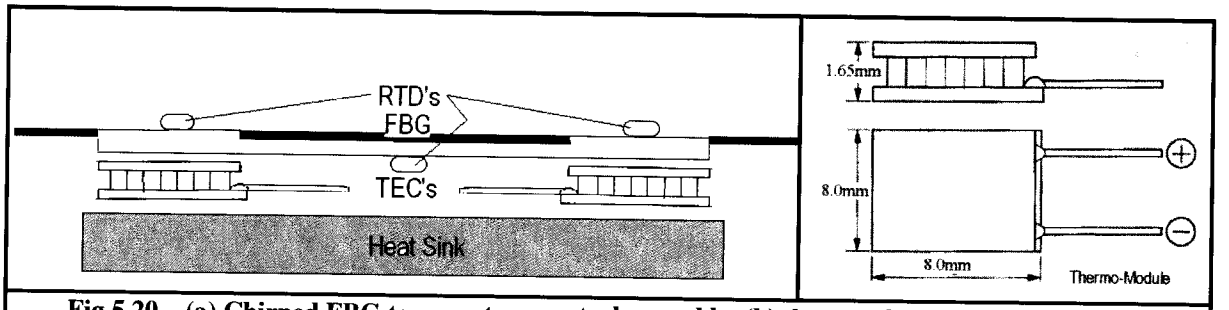

Fig.5.20 – (a) Chirped FBG temperature control assembly, (b) thermo-electric module diagram

Table 5.2 – Measured RTD Temperature Values

Measurement #	RTD 1 (°C)	RTD 2 (°C)	RTD 3 (°C)
1	27	26.9	27
2	29.2	31.6	33.3
3	31.2	35.2	39.5
4	31.8	38.2	44.5
5	32.8	42.0	51.5
6	35.2	46.2	57.3
7	36.9	50.5	63.7
8	38.2	53.5	68.5
9	39.5	55.5	73.9

In Table 5.2 one can see the temperature values that were measured by the RTD's at different voltage settings of the TEC on the right-hand side of the setup shown in Fig.5.20. The wavelength shift in the chirped grating is shown in Fig.5.17 below:

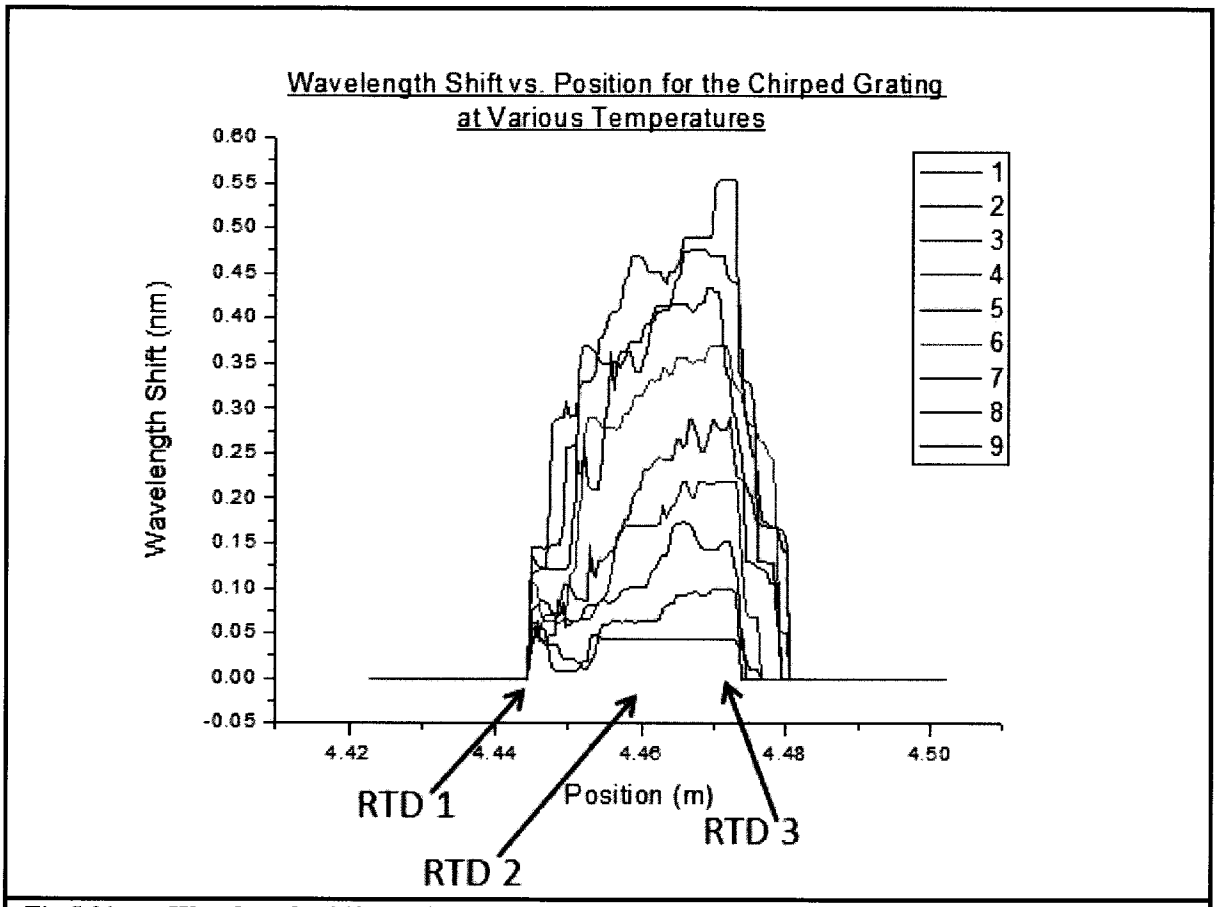

Fig.5.21 – Wavelength shift profile with respect to position of the chirped grating over several temperature ranges shown in Table 5.2.

This data was obtained using the quadrature interferometer setup and the ESS algorithm whereby 25pts/cm was obtained (400μm spatial resolution) and an interpolation factor of 10 was used giving 7.56pm spectral resolution. As before, no averaging was done over several sweeps. The wavelength shift curve with respect to the RTD 3 temperatures in Table 5.2 is seen in Fig.5.22.

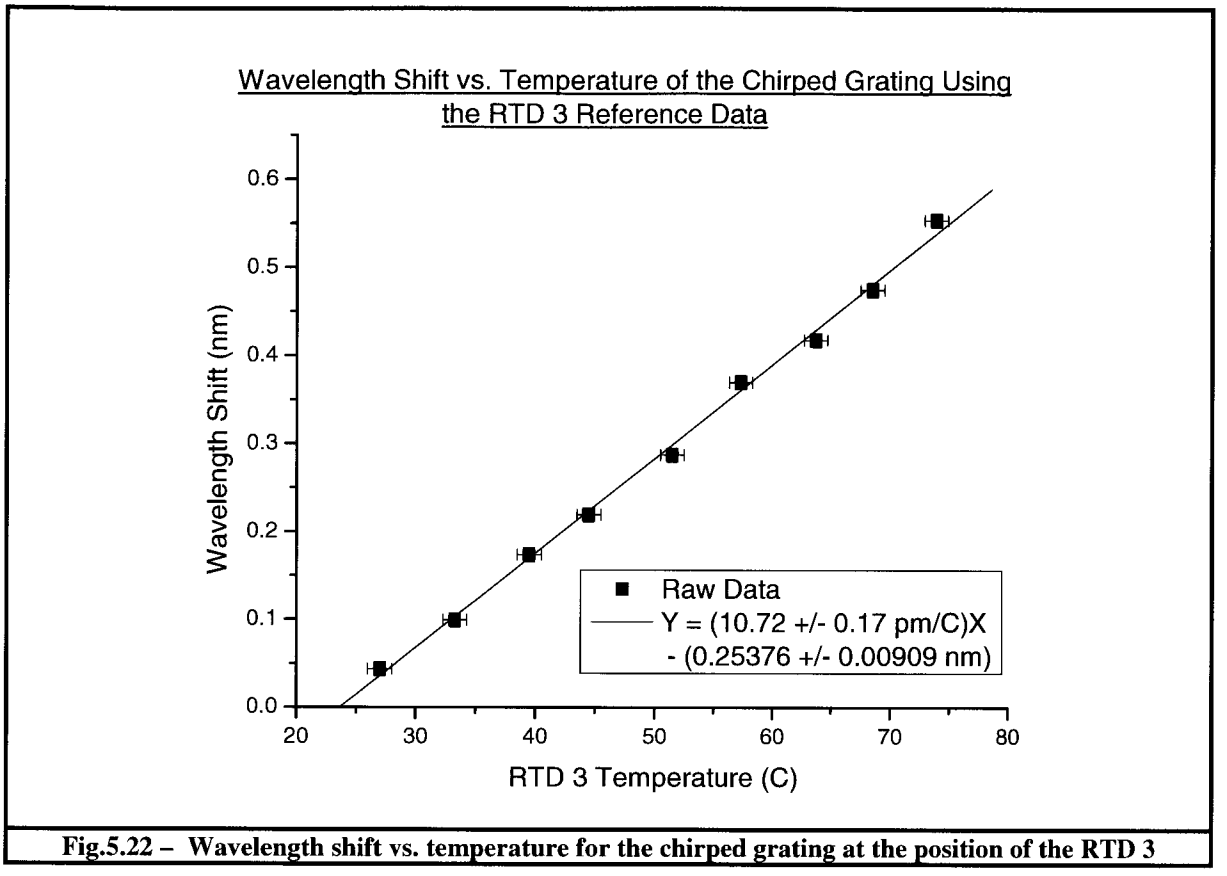

Fig.5.22 – Wavelength shift vs. temperature for the chirped grating at the position of the RTD 3

The slope for the wavelength shift vs. RTD 1 temperatures at its associated location is also the same as that shown in Fig.5.18 to within the given error. Thus, as is seen the chirped gratings could also be used as a *distributed sensor* by measuring the wavelength shift anywhere along them instead of as a *point sensor* like their linear grating counterparts. As far as is known, at the time of writing this thesis there have been no publishings of using chirped gratings in conjunction with OFDR setups for use as a distributed temperature sensor.

5.5 Performance Comparison of Fiber Bragg Gratings to Plain SMF-28 Fibers

When using linear FBG's as point sensors with OFDR setups they have one main advantage over regular SMF's - that is the SNR of the cross-correlations used to measure the wavelength shift at that section of fiber. A typical cross-correlation for a 1cm section of SMF can be seen in Fig.5.23(a) below. The difference between the amplitude of the primary peak and the secondary peak (noise) rarely gets better than 3dB. On the other hand, Fig.5.23(b) shows a typical cross-correlation of a 1cm section of a linear FBG. As is seen, the SNR between the primary and secondary peak for it is up around 15-18 dB. This improved SNR means that little to no averaging needs to be carried out to measure the wavelength shift of the section which is proportional to the stimuli being applied. The drawback to linear FBG's is as mentioned they serve as point sensors so events can be missed if they take place in between discrete sensors.

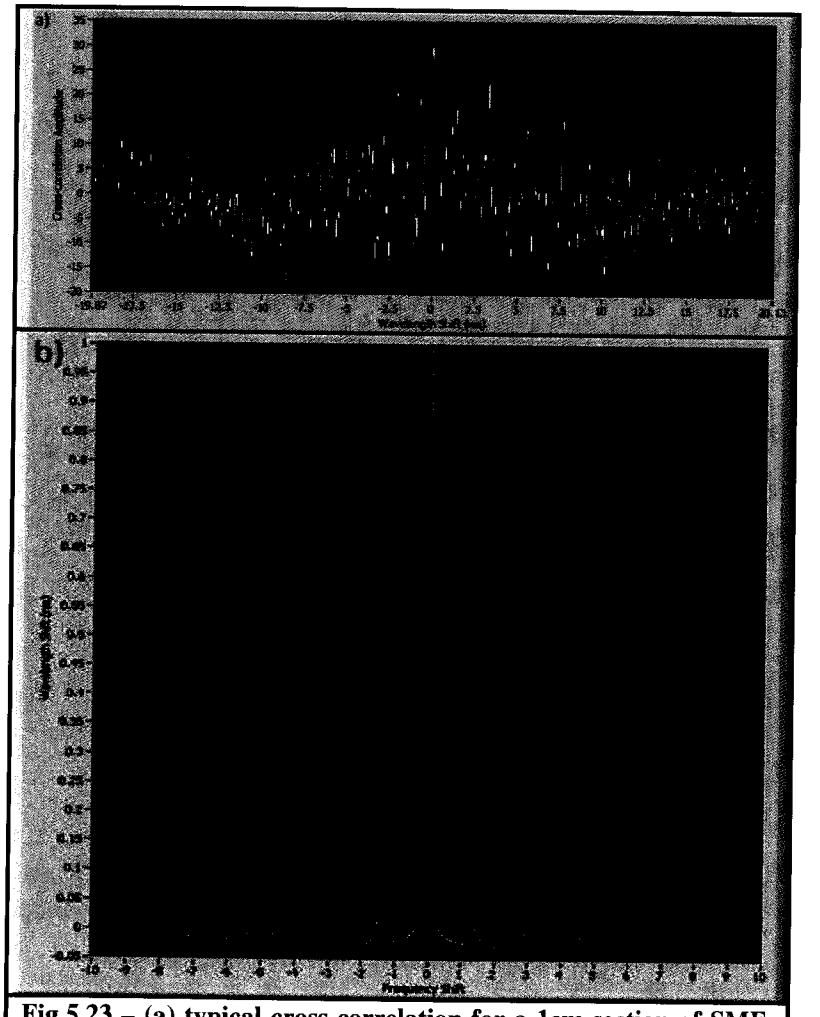

Fig.5.23 – (a) typical cross-correlation for a 1cm section of SMF, (b) typical cross-correlation for a 1cm FBG section

Depending on the type of stimuli being measured, as discussed in the previous section, a

chirped grating could be a good compromise between the two for many applications. The SNR of its cross-correlation is not as good as the linear FBG's but it is a few dB better than the SMF. Accordingly there is less of a chance of picking up jitter in the wavelength shift compared to the regular SMF (assuming no averages are carried out), yet at the same time it can still function as a distributed FUT, which linear gratings even if in series often cannot.

Chapter 6

System Optimization and Errors

All of the results presented so far were primarily based on 1cm sections of the FUT where no averages over multiple sweeps were carried out. Other than increasing the segment size Δx of the FUT to increase the resolution of the cross-correlation and in turn the wavelength shift of the spectral response for that segment, the alternative versions of the OFDR setup that were discussed in Ch.2, and the different data processing algorithms that were discussed in Ch.3 the following chapter will go into optimization of other system variables for improving the overall accuracy in both the spectral and spatial domains.

6.1 Averaging Over Multiple Sweeps

In reference [17] the statistical nature of OFDR is discussed. Since the optical sweep is finite and the Fourier transform of the data set is re-created in a statistical nature, the resulting function can seem often ragged. If one averages the raw data over m sweeps then the standard deviation improvement will be proportional to $0.5\sqrt{m}$. Now this is relying on the fact that each sweep has perfect triggering such that the absolute phase information is preserved. When this is not the case the standard deviation improvement is much lower. On the other hand, if one Fourier transforms the raw beating data first to get the beating

frequency (backscattering) profile and then does the averaging because each profile has been statistically created in this domain, the absolute phase information is not needed (only the relative phase information). It is because of this that one can get away without having perfect triggering for every sweep yet still get considerable improvement in the SNR. From experimental trials, this holds true up to averaging in the Fourier domain over 15 sweeps. After that, one gets diminished returns because coherence noise begins to dominate. This relationship is demonstrated in the following two sections.

6.2 Variation in Optical Linewidth

The Agilent laser that I used in this research had the built - in capability of varying the linewidth of its output from 100kHz to 50MHz; the New Focus laser I also used had a linewidth of 75kHz. Keeping the optical power the same in both lasers, I compared the SNR over a different number of sweep average while varying the linewidth sources – these results can be seen in Fig.6.1 below. When comparing the 75kHz to the 1.098MHz linewidth there is over a 48dB improvement in SNR in the spatial domain. As well, as is seen one does not get much more of an improvement in SNR past the 15 averages mark. Based on these results, with respect to OFDR the narrower the linewidth of the source the better the SNR. I did not illustrate for linewidths

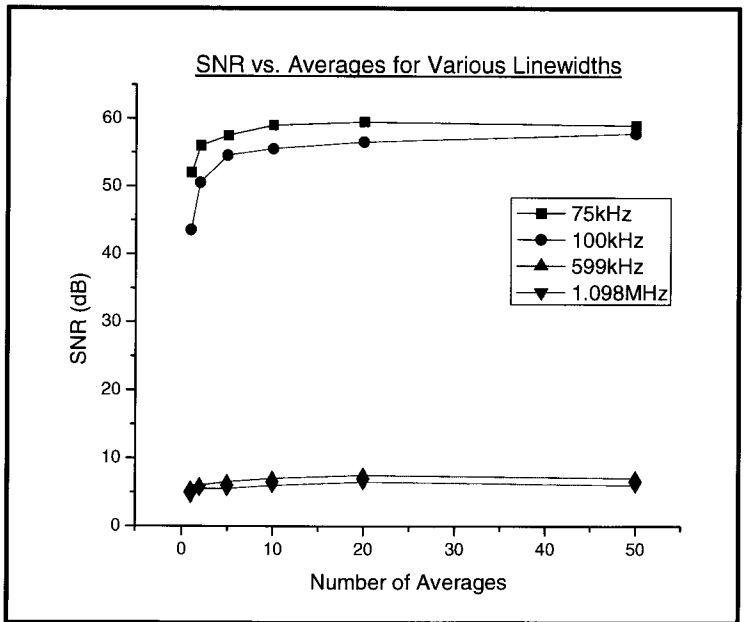

Fig.6.1 – SNR vs. Averages for several different optical linewidths

greater than 1.098MHz because beyond this point the noise was too large in the auxiliary interferometer to serve as a proper external clocking signal for the data acquisition.

6.3 Increasing Optical Tuning Range

At the beginning of Ch.3 I discussed how when one increases the sweeping range they also increase the spatial resolution of the FUT - this is described by Eq.3.1. Measurements were carried out to see how much of an improvement in SNR was made in the spatial domain by increasing the tuning range. This is seen in Fig.6.2 below. For very short tuning ranges such as 0.01nm the SNR actually decreases when the number of averages increases but for 0.1nm or greater the SNR increases with respect to the number of averages. As was mentioned earlier though, one gets diminished returns with respect to averages past the 15 – 20 sweep range. When comparing the 5nm to the 0.01nm tuning range at the 20 average position gets a 26dB improvement in the spatial domain. If one increases the tuning range to 20nm they get a 30dB improvement compared to the 0.01nm curve, but if the range increases beyond this point they again experience diminished returns. As was touched upon in §3.7.3 when discussing the EOSR algorithm and illustrated in Table 3.3 one actually gets a slight (1 to 2dB) degradation of the SNR in the spectral domain when going much past the 10 – 20nm

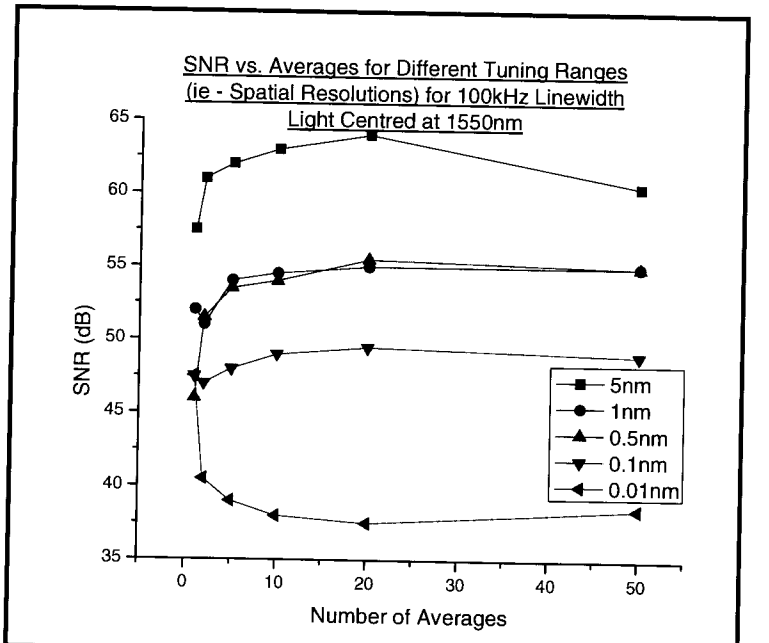

Fig.6.2 – SNR vs. Averages for several different tuning ranges

range. The only main incentive to go beyond the 20nm sweeping range for sensing purposes is to increase the dynamic wavelength shifting range if needing to sense high stresses which will in turn manifest in large wavelength shifts. Either that or if you have metal specialty coatings on the fiber and are wanting to measure very high temperatures (800+°C) as was discussed by Sang *et al.* in reference [34].

6.4 Differentiation of Temperature Stimulus From Stress/Strain

In this work I have discussed doing temperature measurements, longitudinal stress (stretching) measurements and torsional stress (twisting) measurements using regular SMF-28 fiber and both linear and chirped gratings written into SMF. Unfortunately none of these types of FUT are able to differentiate whether the wavelength shifts are coming from temperature changes or some type of stress. When I varied one stimuli I kept the others constant but this is not often the case when it comes to real world sensing applications. Using these types of FUT then, when there are multiple types of stimuli can in turn give distorted results.

One means of resolving this problem is to use highly birefringent fibers such as polarization maintaining (PM) fibers, photonic crystal fibers, or others as the FUT. Birefringence, Δn, is given by:

$$\Delta n = n_{slow} - n_{fast} \ , \tag{6.1}$$

where n_{slow} and n_{fast} represent the slow and fast indices of refraction. Froggatt mentions in one of his patents[35] a method where he uses his polarization diverse setup in Fig.2.11 along with a FUT of PM fiber. He takes the first and second spectral responses where he initially does purely a temperature measurement, then repeats it again where he does purely strain measurements with the PM fiber. He then as was outlined in the basic algorithm of Ch.3 carries out the cross-correlation on first the temperature spectral responses, then the strain

spectral responses. Then the process is repeated but using the *autocorrelation* instead. From this process two constants come out of the cross-correlation process for temperature χ_{TC} and strain $\chi_{\varepsilon C}$, while two more come out of the autocorrelation which are χ_{TA} and $\chi_{\varepsilon A}$ for temperature and strain respectively. These constants can then be put into a 2x2 matrix such that when later carrying out the autocorrelations ($\Delta\upsilon_{auto}$) and cross-correlations ($\Delta\upsilon_{cross}$) on a fiber segment at a later time, the temperature Δt and strain $\Delta\varepsilon$ for that segment can be found by solving the following:

$$\begin{bmatrix}\Delta t \\ \Delta\varepsilon\end{bmatrix} = \begin{bmatrix}\chi_{TA} & \chi_{TC} \\ \chi_{\varepsilon A} & \chi_{\varepsilon C}\end{bmatrix}\begin{bmatrix}\Delta\upsilon_{auto} \\ \Delta\upsilon_{cross}\end{bmatrix}. \tag{6.2}$$

6.5 How PBS Response Affects SNR

In §2.6 (Table 2.5) I mentioned how the polarization diverse setup performed the poorest out the 5 configurations. This section shall discuss this further. Seen in Fig.6.3 is a 100nm sweep using the polarization diverse setup:

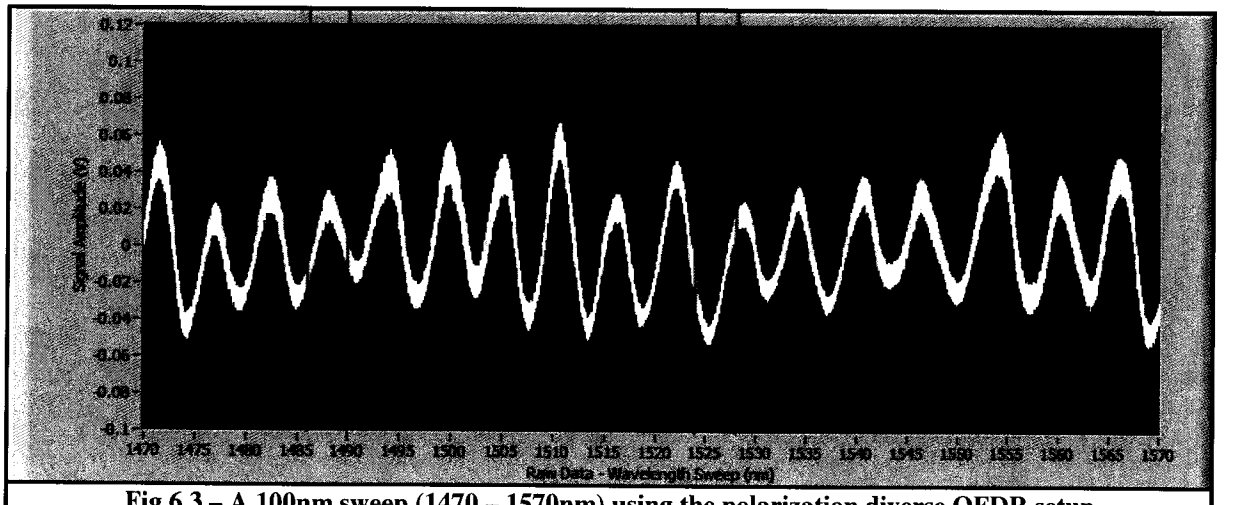

Fig.6.3 – A 100nm sweep (1470 – 1570nm) using the polarization diverse OFDR setup

Ideally as the light oscillates back and forth between the x and y-axis with respect to wavelength, the amplitude of the vector sum of the two channels will remain constant across

every cycle. If the light were linearly polarized or circularly polarized this would be the case. Unfortunately the majority of the light is either elliptically polarized or has a random polarization state. When looking at Fig.6.3 the sections with lower amplitudes have a lower overall elliptically polarized light contribution – so are less distorted. On the other hand, the sections of the sweep with high amplitudes have a larger overall elliptical contribution leading to a larger distortion. To see how much the elliptically polarized light affects the overall SNR I grabbed two subsets from the above data set the first 4nm section is from 1486-1490nm which has a low overall amplitude. The other 4nm section is 1524-1528nm which is a higher amplitude/distortion. A zoom in of these subsets and their FFT's can be seen in Fig.6.4 and Fig.6.5 below.

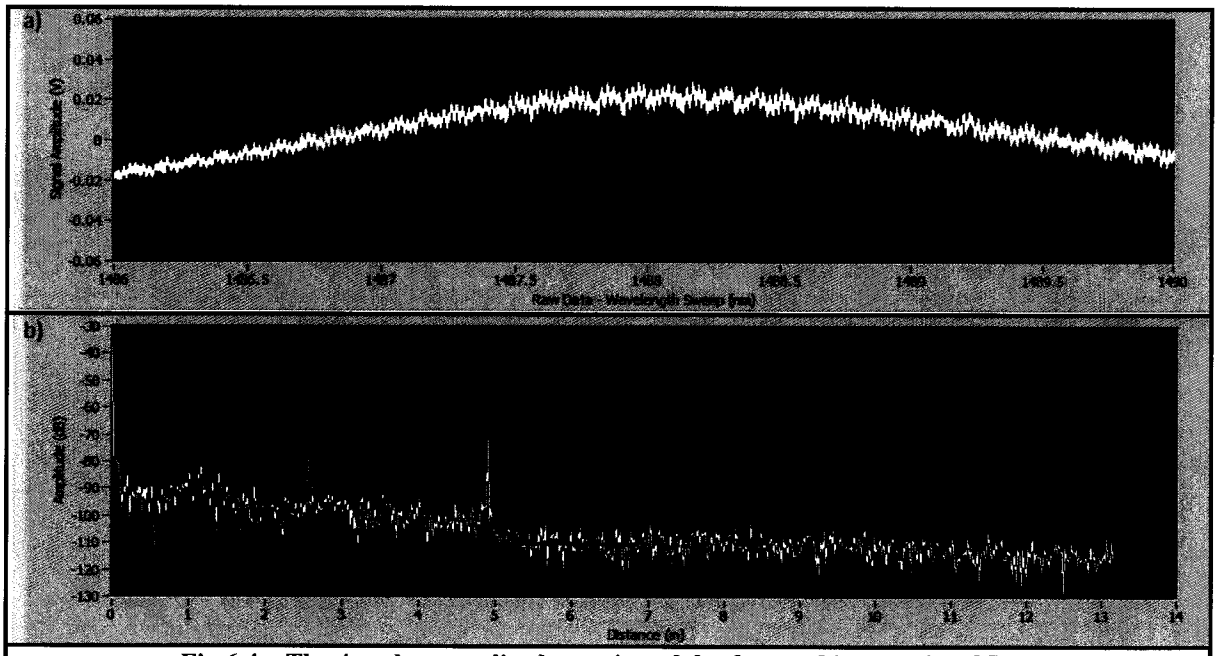

Fig.6.4 – The 4nm low amplitude portion of the data and its associated FFT

Two things one should take note of are SNR of the Fresnel reflection at the 4.9m mark which is 39dB as well as the amplitude of the DC component which is about -37dB. On the other hand when looking at the same positions from the 4nm subset with a high

amplitude as is seen in Fig.6.5 we see that the SNR of the same Fresnel reflection is 32dB while the amplitude of the DC component is -27dB. Accordingly the Fresnel reflection is 7dB higher with the low amplitude section of data than with the high amplitude section. In the same regard, the DC component of the low amplitude subset is 10dB lower than that of

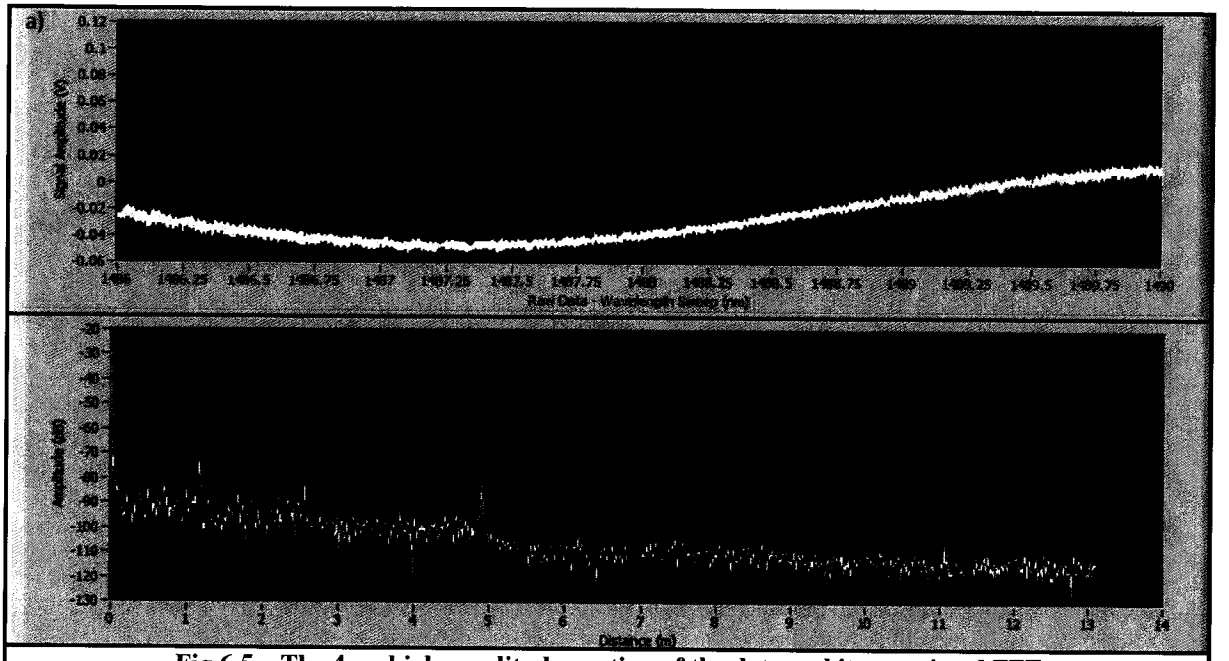

Fig.6.5 – The 4nm high amplitude portion of the data and its associated FFT

the high amplitude data. This is because the response of the polarization beam splitter for elliptically polarized light treats the distortions of the non-uniform projections as a low frequency component. Thus the DC component rises for wavelength regions with large amounts of elliptically polarized light while simultaneously experiencing a decrease in SNR across the rest of the backscatter profile. Accordingly for those wanting to use the PD setup for sensing applications, they may want to choose their sweeping range wisely – keeping to the areas of lower overall amplitudes so that they do not experience of an overall drop of up to 7dB. This is the main reason why the PD setup performed the poorest out of the 5 setups as is seen in Table 2.3

Chapter 7

Conclusion

7.1 Thesis Outcomes

Over the course of this thesis the classical OFDR theory, setup and analysis were discussed. Having outlined their limitations I attempted to improve upon them. In Ch.2 I discussed 5 unique variants of the OFDR setup: *the Basic Setup, Polarization Diverse Setup, Differential Setup, Quadrature Interferometer Setup and Differential Quadrature Setup.* Out of these, the *Differential Quadrature Setup* performed the best in the spatial domain having a relative SNR of 27.5dB higher than the basic setup which performed the worst.

In Ch.3 I discussed how for when trying to detect the wavelength shift in 1cm segments Δx there was an inherent resolution limit of 75.6pm using the classical analysis no matter what the optical tuning range used. To improve upon this I discussed 4 novel data analysis algorithms: the Fourier Interpolation Algorithm (FIA), Extended Optical Sweep Range (EOSR) Algorithm, Boxcar Filter (BF) Algorithm, and Extended Segment Size (ESS) Algorithm. Out of these 4, the ESS algorithm performed the best when compared to the classical algorithm by: a) preserving the dynamic range such that it was the same as the classical algorithm, an overall relative SNR improvement of 1.31dB, and c) a factor of 40 improvement in the spectral resolution, from 75.6pm for a 1cm segment down to 1.89pm. If doing temperature measurements with SMF it would approximately mean going from 8°C resolution when using the classical algorithm down to 0.2°C resolution when using the ESS algorithm.

Ch.4 discussed carrying out temperature, longitudinal stress (stretching), and torsional stress (measurements) using the OFDR setups. For the temperature measurements when the

polarization diverse setup was used in conjunction with the classical algorithm a wavelength shift vs. temperature relationship was found to be: 9.04 ± 0.65 pm/°C for 900μm SMF-28 fiber. When I used the differential quadrature setup with the ESS algorithm with a standard SMF-28 fiber I found: a) that in fact I could obtain true 1cm segment resolution, as well as b) when using standard SMF-28e the wavelength shift vs. temperature curve was found to be 9.20 ±0.05 pm/°C. When using the DQI setup and ESS algorithm again I also found that when using 900μm SMF that when doing stretching measurements there was a wavelength vs. force relationship of 10.48 ± 0.03 pm/g or 1069.39 ± 3.06 pm/N. When using the same type of fiber to do torsional stress measurements the polarization diverse setup with the classical algorithm found a relation of -24.6 ± 0.3 pm/(twist·m) while the DQI/ESS setup found a relationship of -25.01 ± 0.08 pm/(twist·m).

In Ch.5 I discussed my collaborative work with NRC-IFCI in developing an in-situ temperature monitoring setup for their low temperature PEM hydrogen fuel cells. This was at the time when I had just developed the FIA so when used in conjunction with the polarization diverse setup that I had built for them, for 4cm FBG segments I was able to calibrate the system such that it provided them with 0.2°C resolution which was on par with the thermocouples they were also using. So from an accuracy standpoint the optical system performed just as well as the thermocouple system but the refresh time in between temperature measurements was 2 to 4 times slower than the thermocouple readout. I then went on to illustrate on when using a parallel network of identical FBG's one can still differentiate each of them by going into the spatial domain. Through a process of filtering/windowing and inverse Fourier transforming one can in turn retrieve the reflectivity, group delay and wavelength shift for each of the individual gratings. The wavelength shift

vs. temperature relationships were found to be 10.39 ± 0.13 pm/°C and 15.32 ± 0.13 pm/°C for FBG A and FBG C respectively. The usage of a chirped grating FUT was also illustrated to work as a distributed sensor for temperature measurements when used in conjunction with the QI setup. The wavelength shift vs. temperatures relationship for it was found to be 10.72 ± 0.17 pm/°C.

Finally, in Chapter 6 I discussed the system optimization and errors. Presented were the results that one can only really get SNR improvement via averaging up to 15-20 averages before getting diminished returns. Also shown is how one can get a 48dB improvement in the spatial domain when using a 75kHz linewidth source compared to a 1.098MHz source. The SNR also improved by increasing the tuning range of the source. A 5nm range compared to an 0.01nm range experiences a 26dB improvement, a 30dB improvement if one goes up to a 20nm tuning range but after this point one begins to again experience diminished returns.

7.1 Future Work

Although all the major objectives I sought out to achieve were successful there is still some room for improvement in several areas. From an algorithm standpoint it would be interesting to compare the overall performance of replacing the Fourier analysis with wavelet analysis. The two methods have been discussed widely for biomedical signal processing[43] where results found that wavelet analysis tended to be faster than its FFT counterpart as well as at times slightly less distorted. Since as is shown from this work the algorithms are quite data processing intensive, anything that could speed the process up the better. As well, in the case of when using SMF as the FUT, especially for small segments $\Delta x \leq 1cm$ a better peak search algorithm could still be developed for in those cases when the primary peak of interest

is not the highest peak in the cross-correlation. This would in turn reduce the amount of overall jitter in the sensing measurements, and/or reduce or eliminate the need for averaging over extra sweeps. Another way of shortening the processing time is to possibly transfer some of the processes that are currently done via software over to an FPGA hardware unit whereby processes such as averaging and FFT'ing are carried out significantly faster.

Another improvement would be more at the laser end of the setup. It doesn't matter if it was the Agilent, New Focus, or Thorlabs lasers used in this research – in order to carry out a full sweep and return to the starting position the time duration is ≥ 1 second. This means that the OFDR setup is only capable of measuring slowly changing variables with respect to time. Based on such, if one could find or develop a sweeping laser source that would have about 100 sweeps/second or greater (while maintaining the coherence length) then they would be able to do more dynamic type measurements as well and/or do a lot of averaging to further improve the sensing results.

References

[1] R. Tennyson, "Installation, Use and Repair of Fibre Optic Sensors" ISIS Canada Corp., Winnipeg, Manitoba (2001)

[2] L. Zou et al., "Distributed Brillouin scattering sensor for discrimination of wall thinning defects in steel pipe under internal pressure", Applied Optics, 43, 1583-1588 (2004)

[3] Corning Single Mode Fiber, PI1036, April 2002

[4] T. Hosaka et al., "Low-loss single polarization fibers with asymmetrical strain birefringence", Electronics Letters, Vol.17, Issue 15, Pg. 530 (1981)

[5] Robert W. Boyd, "*Nonlinear Optics - 2nd Edition*", Academic Press, London, 2003

[6] L. Fabelinskii, "*Molecular Scattering of Light*", Plenum Press, New York, 1968

[7] Gaëlle Lucas-Leclin, "An Optical Time Domain Reflectometry Set-up for Laboratory Work", Conference on Education and Training in Optics & Photonics, Marseille, October 2005

[8] F. Ravet et al., "Detection of buckling in steel pipeline and column by the distributed Brillouin sensor", Optic Fiber Technology, Vol. 12, 305-311, 2006.

[9] B. Masters, "Early Development of Optical Low-Coherence Reflectometry and Some Recent Biomedical Applications", J. Biomedical Optics, Vol. 4, 236, 1999.

[10] M. Froggatt et al, "Millimeter Resolution Optical Reflectometer Over Up to Two Kilometers of Fiber Length", Fiber-Optics and Photonics Technology Conference IEEE, 52-53, October 2007

[11] W. Eickhoff and R. Ulrich, "Optical frequency domain reflectometry in single-mode fiber", Appl. Phys. Lett., 39(9), Nov. 1981, Pg.693

[12] U. Glombitza and E. Brinkmeyer, "Coherent Frequency-Domain Reflectometry for Characterization of Single-Mode Integrated-Optical Waveguides", Journal of Lightwave Technology, Vol. 11, No.8, Aug. 1993, Pg.1377

[13] J.P. von der Weid et al., "On the Characterization of Optical Fiber Network Components with Optical Frequency Domain Reflectometry", Journal of Lightwave Technology, Vol. 15, No. 7, July 1997, Pg. 1131.

[14] Jesse Zheng, "Analysis of Optical Frequency-Modulated Continuous-Wave Interference", Applied Optics, Vol. 43, No. 21, 20 July 2004, Pg. 4189

[15] Jesse Zheng, Continued Analysis of Optical Frequency-Modulated Continuous-Wave Interference", Applied Optics, Vol. 44, No. 21, 10 February 2005, Pg. 765

[16] A.J. Hymans and J. Lait, "Analysis of a frequency-modulated continuous-wave ranging system", Proc. IEEE 107, Pg. 356-372, 1960

[17] Jozef Jasenek, "Optical Frequency-Domain Reflectometry (OFDR)", http://www.eaeeie.org/theiere_bratislava/5-1.html, FEI STU Bratislava, Slovakia

[18] Dawn K. Gifford, Brian J. Soller et al., "Distributed Fiber-Optic Temperature Sensing using Rayleigh Backscatter", IEEE 31st European Conference on Optical Communication, 2005. ECOC 2005, Sept. 2005, Vol.3, Pg. 511-512

[19] Brian J. Soller, Dawn K. Gifford et al., "High resolution optical frequency domain reflectometry for characterization of components and assemblies", Optics Express, Vol.13, No.2, Jan. 2005, Pg. 666-674

[20] B.J. Soller, M. Wolfe, M.E. Froggatt, "Polarization resolved measurement of Rayleigh backscatter in fiber-optic components", OFC Technical Digest 2005, paper NWD3

[21] A. Huber, M. Wojtkowski et al., "Amplified, frequency swept lasers for frequency domain reflectometry and OCT imaging: design and scaling principles", Optics Express, Vol.13, No.9, May 2005, Pg. 3513-3528

[22] Andrew M. Rollins, Joseph A. Izatt, "Optimal interferometer designs for optical coherence tomography", Optics Letters, Vol.24, Issue 21, Pg.1484-1486

[23] Thorlabs PDB100 Series Balanced Amplified Photodetectors Operation Manual

[24] Paul E. Greene, Jr., "Fiber Optic Networks", Pg.70-79, 123-129, Prentice Hall, Englewood Cliffs, New Jersey, 1993

[25] C. Flueraru, H. Kumazaki et al., "Quadrature Mach-Zehnder interferometer with application in optical coherence tomography", Journal of Optics A: Pure and Applied Optics, Vol.9, L5-L8, 2007

[26] Youxin Mao, Costel Flueraru et al., "Full Range Swept-Source Optical Coherence Tomography Using 3x3 Mach-Zehnder Interferometer with Unbalanced Differential Detection", 2008 IEEE International Symposium on Biomedical Imaging: From Nano to Macro, Paper: SA-PM1-O2.2

[27] Analog Devices, Low Cost Low Power Instrumentation Amplifier AD620 Specifications sheet

[28] Pawel R. Kaczmarek, Jakub Werbinsky, Krzysztof M. Abramski, "Optical Frequency Domain Reflectometer for Diagnostics of Short Distance Networks", IEEE ICTON 2004, We.P.8, Pg.193-195

[29] Mark Froggatt and Jason Moore, "High-spatial-resolution distributed strain measurement in optical fiber with Rayleigh scatter", Applied Optics, Vol. 37, No. 10, April 1998, Pg. 1735-1740

[30] Mark Froggatt, Brian Soller et al., "Correlation and Keying of Rayleigh Scatter for Loss and Temperature Sensing in Parallel Optical Networks", IEEE PDP17

[31] B.J. Soller, M. E. Froggatt et al., "Measurement of Localized Heating in Fiber Optic Components with Millimeter Spatial Resolution", National Fiber Optic Engineers Conference, March 2006, Pg. 3-5

[32] Brian J. Soller, Steven T. Kreger et al., "Optical Frequency Domain Reflectometry For Single And Multi-Mode Avionics Fiber-Optics Applications", Avionics Fiber-Optics and Photonics, 2006. IEEE Conference, Sept. 2006, Pg.38-39

[33] H. Murayama, H. Igawa et al., "Distributed Strain Measurement with High Spatial Resolution Using Fiber Bragg Gratings and Optical Frequency Domain Reflectometry", OSA/OFS 2006, paper Th340

[34] Alex K. Sang, Mark E. Froggatt et al., "One Centimeter Spatial Resolution Temperature Measurements in a Nuclear Reactor Using Rayleigh Scatter in Optical Fiber", IEEE Sensors Journal, Vol. 8, No. 7, July 2008, Pg. 1375-1380

[35] Froggatt, Mark, "Distributed Strain and Temperature Discrimination in Polarization Maintaining Fiber", 7 June 2007, Patent #: WO 2007/149230 A2

[36] Froggatt et al., "Apparatus And Method For Measuring Strain In Optical Fibers Using Rayleigh Scatter", 8 April 2003, Patent #: US 6,545,760 B1

[37] Froggatt et al., "Identifying Optical Fiber Segments And Determining Characteristics Of An Optical Device Under Test Based On Fiber Segment Scatter Pattern Data", 21 October 2008, Patent #: US 7,440,087 B2

[38] Turan Erdogan, "Fiber Grating Spectra", Journal of Lightwave Technology, Vol. 15, No. 8, August 1997

[39] Ryan Bolen, "Temperature Controlled Fiber Bragg Gratings For Active Dispersion Compensation", University of Ottawa Physics Dept. Research Paper, April 2006

[40] A. Othonos et al., "Fiber Bragg Gratings", Artech House, Boston, 1999

[41] Image is from the HydrogenHighway website:
http://www.hydrogenhighway.ca/code/navigate.asp?Id=220

[42] Diagrams used with permission from NRC-IFCI

[43] Sandro A. P. Haddad and Wouter A. Serdijn, "Ultra Low-Power Biomedical Signal Processing", Springer Netherlands, 2009

Publications

Posters/Proceedings

[1] R. Bolen and X. Bao, "Swept Wavelength Interferometry For Acoustic Wave Detection", 2007 GEOIDE Conference, Project: SII-84

[2] R. Bolen and X. Bao, "Measurement of Dynamic Water Properties Measurement Using OFDR", 2008 GEOIDE Conference, Project: SII-84

[3] X.Bao and R. Bolen, "Optical Frequency Domain Reflectometry for Temperature and Strain Measurements", 2009 GEOIDE Conference, Project: SII-84

[4] R. Bolen and X. Bao, "Development of Distributed Temperature Sensor for In-situ Mapping of Temperature Distribution Inside of a PEM Fuel Cell", 2009 CIPI Conference, CIPI-Poster-25-6, Ref: 214-DHb6-55